Fertility assessment in porphyry copper exploration – an industry perspective

Christian Ihlenfeld
Anglo American plc, London, United Kingdom

Abstract. Fertility assessment plays an increasingly important role in porphyry Cu exploration programs to support effective area selection and target identification from the province- to the prospect-scale. Lithogeochemical proxies of porphyry Cu fertility have been used relatively widely by industry and have been shown to be reasonably effective in differentiating barren from potentially mineralized systems. With the ambition to develop new fertility proxies that allow us to discriminate more effectively between well-endowed and poorly endowed systems, research and industry have focused in recent years on the chemistry of various accessory minerals, including zircon and apatite. However, our ability to harness the potential wealth of fertility-related information recorded by these minerals is still limited and developing. Industry and academic research need to collaborate to address this important and challenging task.

1 The importance of fertility assessment in exploration

Understanding the fertility (i.e., potential endowment) of mineral systems is of fundamental strategic relevance to mineral exploration. Within the general framework of mineral system analysis (e.g., McCuaig and Hronsky 2014), an assessment of system fertility supports effective area selection and target identification during an exploration program from the province- to the prospect-scale. If fertility assessment is effectively implemented, less money and time will be required to identify and prioritize the most prospective targets within a district, facilitating quicker and better decisions on drill target selection, and thereby increasing the chances of a successful discovery within existing exploration budgets.

Effective implementation of fertility assessment in the exploration process requires two critical aspects:

(a) An understanding of the fundamental controls governing mineral system fertility, and of the extent to which these controls have varied in space and time.

(b) Effective, measurable and mappable proxies that are predictive of system fertility at the respective scale.

The subject of this talk is the latter aspect and focuses on the utility of the currently available geochemical proxies of porphyry Cu fertility. The talk will present and review the results of in-house case studies and published work to highlight the strengths and limitations of these proxies for exploration targeting. Based on this review, outstanding questions and key areas for future research and development will be identified.

2 Available proxies of porphyry copper fertility – strengths and limitations

2.1 Lithogeochemical proxies

Lithogeochemical proxies of porphyry Cu fertility, such as those developed by Loucks (2014), have been used relatively widely by industry and have been shown to be reasonably effective in differentiating barren from potentially mineralized systems. One of the key advantages of these proxies is that the proxy information can be generated routinely, fast and at relatively low cost through commercial laboratories. The lithogeochemical proxies can be used from the regional down to the district scale to identify arc segments, individual igneous complexes within them, and stages in the evolution of long-lived magmatic centers that match the chemical features of copper-ore-forming arc magmas. Detailed lithogeochemical work by the author in the Los Bronces (Chile) and Quellaveco (Peru) districts, for instance, identified and mapped out in both districts the geochemical evolution and development of porphyry Cu fertility of the host batholith and related porphyry intrusions in space and time (over a 15 Myr period), culminating in both cases in the formation of major world-class porphyry Cu deposits.

However, a known limitation of the lithogeochemical proxies of porphyry Cu fertility is that they generally do not provide a clear indication of the quality/endowment of the system and may generate a relatively high rate of false positives. This is illustrated, for instance, by the results of the stochastic modelling by Chiaradia and Caricchi (2017) of the deep magmatic controls on porphyry Cu deposit endowment. While the modelling corroborates the empirically observed association of porphyry Cu deposits with a specific interval of Sr/Y ratios (~100 ± 50) in the magmatic rocks, it also shows that 2/3 of the model simulations within this Sr/Y interval produce systems with <10 Mt Cu (including barren systems). By contrast, only 9%, 4% and 0.2% of simulations within this Sr/Y interval produce giant to super-giant systems containing 30-50 Mt Cu, 70-90 Mt Cu and >90 Mt Cu, respectively.

The likely reason for the inability to effectively discriminate between variably endowed porphyry systems is that the lithogeochemical proxies of porphyry Cu fertility reflect to a large extent only a single (albeit very important) parameter/process (i.e., the development of water-rich magmas during long-term residence and differentiation in lower crustal "hot zones"; Annen et al. 2006), whereas the endowment of porphyry Cu deposits is controlled by a combination of critical factors.

Therefore, lithogeochemical fertility proxies like those developed by Loucks (2014), constrain a necessary, but not sufficient, condition of a system to develop a major porphyry Cu deposit.

2.2 Mineral chemistry proxies

With the ambition to develop additional or more comprehensive proxies of porphyry Cu fertility that allow us to effectively and reliably discriminate between well-endowed, poorly endowed and barren systems, research and industry have focused in recent years on the chemistry of accessory and alteration minerals, including zircon, apatite, titanite, magnetite, rutile and chlorite.

Zircon and apatite have received particular attention as they potentially record intrinsic magma characteristics that are widely considered important in the formation of porphyry Cu deposits, such as oxidation state and elevated water content in the case of zircon, and S and Cl contents in the case of apatite. In addition, zircon and apatite persist during weathering and transport in the surface environment, which potentially allows their use as fertility proxies in mechanically dispersed surface sediments (e.g., drainage sediments, till). Other favorable properties of zircon include that it is largely resistant to hydrothermal alteration, can be precisely dated and provides information on its crystallization temperature and the relative degree of magmatic fractionation. Furthermore, zircon morphology and growth zoning as revealed by cathodoluminescence imaging may potentially provide important information on changing conditions during zircon crystallization that may help to distinguish between fertile and barren suites (e.g., Lu et al. 2016; Corfu et al. 2003). Analysis of specific growth zones may also provide evidence of episodic recharge of mafic magmas (Buret et al. 2016), which is considered by some a potential trigger of porphyry formation and source of excess S and metals (e.g., Zajacz and Halter 2009). Like zircon, igneous apatite is also frequently zoned, with S-/Cl-rich cores and S-/Cl-poor rims observed in some fertile systems that are interpreted to reflect fluid exsolution and degassing (e.g., Bouzari et al. 2017). However, in contrast to zircon, apatite is sensitive to alteration overprint (e.g., Bouzari et al. 2016) and may be present as both igneous and hydrothermal apatite in porphyry systems. The composition of hydrothermal apatite has been shown to reflect the nature of the mineralizing fluid and may potentially record useful fertility information (Loader 2017). Characteristic compositional and luminescence features of altered apatite may be used to recognize the existence and type of hydrothermal alteration in dispersed surface sediments (Bouzari et al. 2016).

However, despite this potential wealth of fertility-related information recorded by zircon and apatite, our ability to harness this information is still limited and developing. For instance, extracting reliable quantitative or even semi-quantitative information on the oxidation state of the magma from the chemistry of zircons has remained elusive so far despite some potentially promising recent progress (Loucks et al., submitted). Furthermore, the effects of co-crystallizing phases on the compositions of zircon and apatite and their potential implications for the assessment of porphyry Cu fertility remain to be fully understood (e.g. Loader et al. 2017).

Anglo American has been conducting several pilot studies in recent years to trial the utility of zircon and apatite mineral chemistry as porphyry fertility indicators. The studies have been conducted in various geological settings, using well-constrained rock and stream sediment samples to get a first-hand understanding of the type and quality of fertility-related information that can be obtained, to develop appropriate workflows and to identify key knowledge gaps and outstanding challenges. Overall, the results of these pilot studies corroborate the potential usefulness of zircon and apatite as porphyry fertility indicators, but also highlight that the ability to effectively and reliably discriminate between well-endowed, poorly-endowed and barren systems remains a challenge, in particular when comparing results between districts. Recognition of fertile signatures in drainage sediments is feasible, but depending on the geological setting and background lithologies effective pre-screening of the zircon and apatite separates prior to LA-ICP-MS and EMP analysis may be required to make the approach time- and cost-effective.

3 Concluding remarks

Fertility assessment plays an increasingly important role in porphyry Cu exploration programs to support effective area selection and target identification from the province-down to the prospect-scale. However, despite this importance the currently available lithogeochemical and mineral chemical proxies of porphyry Cu fertility have limitations and generally only discriminate broadly between barren and fertile systems, but do not allow to effectively and reliably discriminate between well- and poorly endowed systems. This is partly due to our incomplete understanding of the fundamental controls that govern the endowment of porphyry Cu systems, but also due to our limited ability to harness the wealth of fertility-related information recorded by the geochemical compositions of rocks and minerals. To address the shortcomings in both aspects, it is necessary to collect a much larger number of integrated datasets for whole rock and multiple mineral indicators in carefully selected, well-characterized samples from porphyry Cu systems and barren analogues that cover the entire endowment spectrum. Industry and academic research need to collaborate on this challenging task.

Acknowledgements

I would like to thank the session organizers for the invitation to give this presentation and Anglo American for their permission to accept this invitation and to share some of our in-house results and ideas on the topic of porphyry Cu fertility.

References

Annen C, Blundy JD, Sparks RSJ (2006) The genesis of intermediate and silicic magmas in deep crustal hot zones. Journal of Petrology 47(3):505-539.

Bouzari F, Hart CJR, Bissig T, Barker S (2016) Hydrothermal alteration revealed by apatite luminescence and chemistry: A potential indicator mineral for exploring covered porphyry copper deposits. Economic Geology 111:1397–1410.

Bouzari F., Hart CJR, Bissig T, Lesage G (2017): Mineralogical and geochemical characteristics of porphyry-fertile plutons: Guichon Creek, Takomkane and Granite Mountain batholiths, south-central British Columbia (NTS 092I, P, 093A, B). In Geoscience BC Summary of Activities 2016, Geoscience BC, Report 2017-1:189–200.

Buret Y, von Quadt A, Heinrich C, Selby D, Wälle M, Peytcheva I (2016) From a long-lived upper-crustal magma chamber to rapid porphyry copper emplacement: reading the geochemistry of zircon crystals at Bajo de la Alumbrera (NW Argentina). Earth Planet. Sci. Lett. 450:120–131.

Chiaradia M, Caricchi L (2017) Stochastic modelling of deep magmatic controls on porphyry copper deposit endowment. Sci. Rep. 7:44523. doi: 10.1038/srep44523

Corfu F, Hanchar JM, Hoskin PWO, Kinny P (2003) Atlas of zircon textures. Reviews in Mineralogy and Geochemistry 53:469–500.

Loader MA (2017) Mineral indicators of porphyry Cu fertility. PhD Dissertation, Imperial College London.

Loader MA, Wilkinson JJ, Armstrong RN (2017) The effect of titanite crystallisation on Eu and Ce anomalies in zircon and its implications for the assessment of porphyry Cu deposit fertility. Earth and Planetary Science Letters 472:107–119.

Loucks RR (2014) Distinctive composition of copper-ore-forming arc magmas. Australian Journal of Earth Sciences 61:5–16.

Lu Y-J, Loucks RR, Fiorentini M, McCuaig TC, Evans NJ, Yang Z-M, Hou Z-Q, Kirkland CL, Parra-Avila LA, Kobussen A (2016) Zircon Compositions as a Pathfinder for Porphyry Cu ± Mo ± Au Deposits. Soc. Econ. Geol. Spec. Publ. 19:329–347.

McCuaig TC, Hronsky, JMA (2014) The mineral system concept: the key to exploration targeting. Soc. Econ. Geol. Spec. Publ. 18:153–176.

Zajacz Z., Halter W (2009) Copper transport by high temperature, sulfur-rich magmatic vapor: evidence from silicate melt and vapor inclusions in a basaltic andesite from the Villarrica volcano (Chile). Earth Planet. Sci. Lett. 282:115–121.

Zircon-hosted apatite inclusions at La Granja Cu-Mo Porphyry, Peru: Implications for the use of apatite as a probe of magma petrogenesis

Emily Brugge[1,2], Jamie J. Wilkinson[1,2], Yannick Buret[2], Andrew J. Miles[3]
[1]Department of Earth Science and Engineering, Imperial College London, UK
[2]London Centre for Ore Deposits and Exploration, Department of Earth Sciences, Natural History Museum, London, UK
[3]Department of Geology, University of Leicester, Leicester, UK

Abstract. Apatite is widely used as a petrogenetic indicator mineral. However due to the rapid diffusion of some elements, the degree to which apatite retains original magmatic compositions in porphyry environments is unclear. To investigate this we have analysed fine-grained (< 10 µm) apatite inclusions in zircon using modified electron microprobe (EMP) and laser ablation inductively-coupled-plasma mass spectrometry (LA-ICP-MS) methods. The inclusions (Ap_{incl}) are inferred to preserve primary apatite compositions, which can be compared with the composition of apatite from the groundmass of the porphyritic rocks (Ap_{mtrx}). We find that Ap_{incl} contain higher concentrations of Cl, S, Sr and lower concentrations of Mg and Mn than Ap_{mtrx}. We infer that the groundmass apatite has re-equilibrated with a later fluid phase. These observations have important implications for how apatites in porphyry systems are used to infer crystallisation conditions. We conclude that the majority of apatite crystals in such systems will undergo re-equilibration and therefore do not record primary crystallisation conditions. Instead, apatite compositions reflect the character of porphyry ore-forming fluids and therefore may have utility as an indicator of ore-forming potential. Apatite inclusions in zircons, although less abundant and more challenging to analyse are more representative of magmatic crystallisation conditions.

1 Introduction

Apatite has regularly been used to help constrain the petrogenesis of igneous rocks (Webster and Piccoli 2015), and more recently to discriminate between ore-hosting and unmineralised intrusions (Duan and Jiang 2018). The growing popularity of apatite is due to the large number of trace elements that can be analysed using methods such as LA-ICP-MS. The chemical composition of apatite can be used as a record of its crystallisation environment and has the potential to be used as an exploration tool for both in situ and detrital grains. In a porphyry environment, the halogen and S contents of apatite can be associated with hydrothermal and ore-forming components, and elements such as REE, Sr, Y etc. reflect magmatic processes including co-crystallising accessory phases. However, metasomatised apatite is common in hydrothermally-altered portions of porphyry systems and even where grains appear unaltered, high diffusion rates in apatite (e.g. F-OH-Cl: 8.1×10^{-8} m^2/s; Mn: 5.4×10^{-7} m^2/s; Cherniak 2010) mean that primary magmatic features, such as zoning, are not well preserved. Apatite hosted in zircon may provide a more robust record of the original composition as the diffusion rates in zircon are considerably lower (Cherniak 2010).

In this study, apatite inclusions in zircon (Ap_{incl}) from the La Granja Cu-Mo porphyry, Peru were analysed. The compositions were then compared to apatite grains within the groundmass (Ap_{mtrx}). Previous studies have found apatite inclusions in zircon to mirror the composition of the groundmass apatite in the rock (Jennings et al. 2011; Bruand et al. 2016). Therefore, at La Granja any difference in composition between Ap_{incl} and Ap_{mtrx} may be due to re-equilibration of the latter. Based on our findings, we question the extent to which the chemistry of Ap_{mtrx} sampled from intrusive rocks belonging to a porphyry system can be used to interpret the magmatic crystallisation conditions. However, our evidence suggests that apatite inclusions in zircon can provide a faithful record of magma petrogenesis.

2 Geological Setting

La Granja Cu-Mo porphyry deposit (-6.35203, -79.127159; Fig. 1) is located in northern Peru within the Western Cordillera. The Miocene deposit is hosted within Eocene volcanic belt and contains total resources of 4329 MT of ore with an average grade of 0.51% Cu (Rio Tinto annual report 2018).

La Granja comprises two main porphyry complexes, Paja Blanca and Mirador, which lie approximately 1 km apart. Both porphyry complexes are composed of a similar sequence of nested porphyry intrusions and range from ~ 14 – 17.6 Ma (Table 1). Of the lithologies sampled for this study, for each porphyry complex the intermineral dacite porphyry is the oldest, followed by the dacite porphyry and then a late quartz porphyry. The system has been subjected to intense hydrothermal alteration (sericitic and argillic overprinting potassic-propylitic) that is focused in the centre of the deposit (Schwartz 1982).

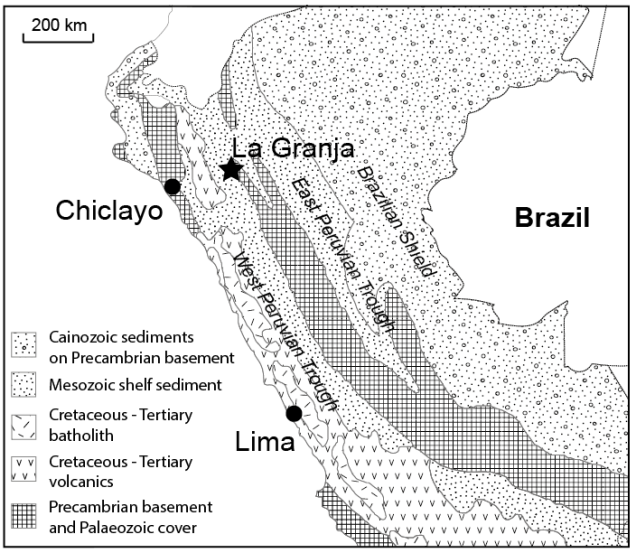

Figure 1. Location of La Granja, which sits at an altitude of 2200 m in the Western Cordillera of the Andes (edited from Meyers 1975).

3 Sample Petrology

3.1 Rock descriptions

Samples of the porphyritic lithologies were collected from drillcore from both Paja Blanca and Mirador. Compositionally the three rock types are very similar. The intermineral dacite porphyry has a crowded texture containing feldspar phenocrysts (50%, < 4 mm), rare quartz eyes (< 5%, 2 mm) with biotite and amphibole within a fine-grained quartz-feldspar-biotite groundmass**.** This unit does not contain any significant Cu mineralisation. The dacite porphyry is interpreted to be one of the main mineralising intrusions. Its mineralogy and texture is very similar to the intermineral dacite porphyry but it contains abundant disseminated Cu-sulphides that are also occasionally present within the quartz eyes. The late quartz porphyry is texturally distinct from the earlier lithologies and contains abundant quartz eyes (≥ 10%, 2-5 mm), feldspar, biotite and amphibole (< 5%) phenocrysts in a glassy matrix (~50%). The alteration of the samples ranges from propylitic to chlorite-sericite. Pseudomorphs of primary mafic minerals are dominated by chlorite and the alteration of feldspar phenocrysts is a prevalent feature.

3.2 Apatite textures

The textural context of Ap_{incl} and Ap_{mtrx} are distinct (Fig. 2). Apatite is one of the most common inclusions in zircon crystals, and are present as small (<10 µm width), prismatic to acicular crystals that cut across the zircon growth zones. Most are located towards the centre of zircon hosts.

Table 1. Lithologies used in this study, U-Pb zircon rim ages and number of spot analyses obtained.

Lithology	Age (n) [MSWD]	Ap_{incl} (EMPA/LA-ICP-MS)	Ap_{mtrx} (EMPA/LA-ICPMS)
Paja Blanca			
Late quartz porphyry	15.09 ± 0.28 (25) [1.3]	(1/2)	(46/25)
Dacite porphyry	15.96 ±0.27 (38) [1.5]	(8/5)	(31/10)
Intermineral dacite porphyry	16.81 ± 0.22 (30) [1.4]	(0/2)	(24/7)
Mirador			
Late quartz porphyry	14.24 ± 0.26 (24) [1.4]	(3/0)	(29/4)
Dacite porphyry	15.06 ± 0.26 (41) [1.9]	(2/4)	(33/14)
Intermineral dacite porphyry	17.58 ± 0.27 (35) [1.4]	(7/1)	(0/0)

Ap_{mtrx} crystals comprise < 5% of the rock. They are generally euhedral to subhedral in shape and occur as micro-phenocrysts in assemblages predominantly made up of quartz, feldspar and minor biotite. In BSE images the Ap_{mtrx} grains appear relatively unaltered with an even surface brightness; some grains do contain small inclusions of monazite.

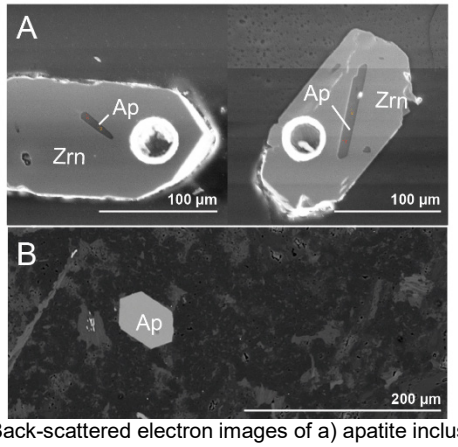

Figure 2. Back-scattered electron images of a) apatite inclusions in zircon and b) apatite within the groundmass of a dacite porphyry sample.

4 Analytical methods

Mounted zircon separates (for Ap_{incl}; Fig. 2a) and thin sections (for Ap_{mtrx}; Fig. 2b) were made from each sample. Apatite was imaged using scanning electron microscopy (SEM) and then analysed by electron microprobe (EMP) and laser ablation inductively-coupled-plasma mass spectrometry (LA-ICP-MS). U-Pb zircon ages obtained for each unit together with the number of analytical spot data acquired using each of the methods are presented in Table 1. Ap_{incl} data from inherited (xenocrystic) zircons were not used in this study.

Due to the small size of the Ap_{incl}, specially modified EMP and LA-ICP-MS methods were adopted. The accuracy and precision of the results were monitored by repeat analysis of Durango, a natural apatite standard (Young et al. 1969). EMP analyses were carried out in the Imaging and Analysis Centre and LA-ICP-MS analyses in

the LODE Laboratory at the Natural History Museum, London.

4.1 EMPA method

Major elements were analysed using a Cameca-SX100 electron microprobe with a 20 kV accelerating voltage and 20 nA bean current. A spot size of 1 µm was used. This set up is non-ideal for F analysis in apatites and resulted in artificially raised values in some cases, likely produced as the result of the orientation of a F-rich apatite (Stormer et al. 1993; Fig. 3) but was necessary because of the very small size of the Ap_{incl} crystals.

4.2 LA-ICP-MS method

LA-ICP-MS analyses were collected using a New Wave ESI 193 µm excimer laser coupled to an Agilent 7700 quadrupole ICP-MS. The analyses were collected using a spot size of 5 µm, and a fluence of 3.5 Jcm^{-2} and a pulse frequency of 10 Hz were used. NIST610 was used as the external standard and Ca was used for internal standardisation.

5 Results

5.1 Major elements: Ap_{incl} vs. Ap_{mtrx}

The Cl and F concentrations in apatite are inversely correlated as is expected for elements substituting into the same structural site. All apatites are fluorapatite and have an average mole fraction chlorapatite of 0.05. Fluorine contents range from 1.56 wt. % to above the stoichiometric limit. Overall, Ap_{inc} display higher average Cl and S concentrations (0.85 wt. %, 1.00 wt. % respectively) than Ap_{mtrx} (0.26 wt. %, 0.15 wt. %; Fig. 3).

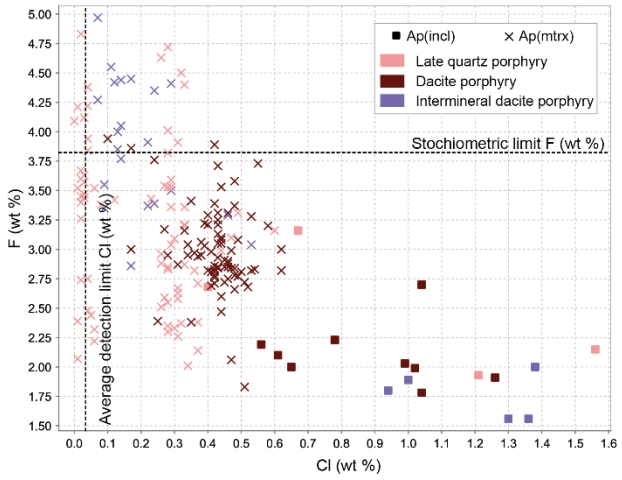

Figure 3. Plot of F against Cl for different apatite types (data acquired by EMPA). Crosses indicate Ap_{mtrx} and squares indicate Ap_{incl}. Lithologies are denoted by colour: intermineral dacite porphyry (purple), dacite porphyry (red), late quartz porphyry (pink). The stoichiometric limit for F substitution in apatite is shown.

5.2 Trace elements: Ap_{incl} vs. Ap_{mtrx}

REE patterns of Ap_{incl} and Ap_{mtrx} are broadly similar (Fig. 4) with LREE enrichment and negative Eu anomalies. However, Ap_{incl} are characterised by more homogenous patterns and are more LREE-enriched and HREE-depleted than Ap_{mtrx}.

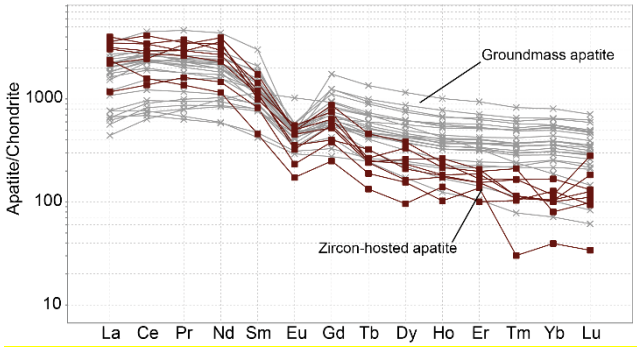

Figure 4. Chondrite-normalised REE patterns for apatites from the dacite porphyry. The Ap_{incl} (red) are slightly depleted in HREE and enriched in LREE relative to Ap_{mtrx} (grey).

The percentage change in elements between the two textural varieties of apatite is illustrated in figure 5.Apatites from the late quartz porphyry tend to display smaller compositional variability in comparison with the other samples.

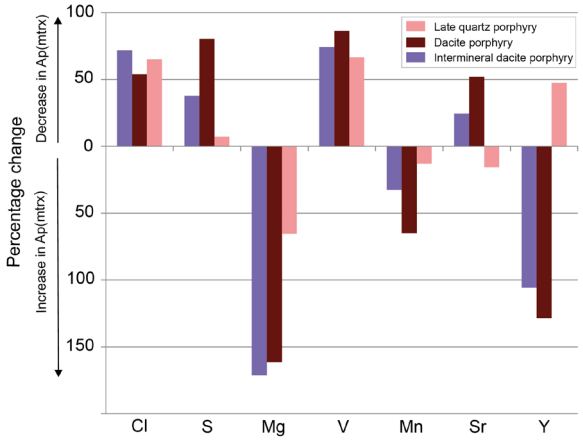

Figure 5. Percentage change in element concentration between Ap_{incl} and $Ap_{mtrx.}$ Lithologies are denoted by colour: intermineral dacite porphyry (purple), dacite porphyry (red), late quartz porphyry (pink).

6 Discussion

Previous studies have observed similar compositions for Ap_{incl} and Ap_{mtrx} in unaltered plutonic rocks (Jennings et al. 2011; Bruand et al. 2016). In this study, the elements that show the greatest variation are those known to have high diffusivity rates in apatite (Cherniak 2010) and are mobile in metasomatised apatite (e.g. Cl, LREE etc. Fig. 3; Fig. 4; Webster and Piccoli 2015). Therefore we propose that Ap_{mtrx} have requilibrated to a fluid phase.

Based on apatite concentrations from the dacite porphyry, Ap_{incl} are assumed to represent an original magmatic endmember composition (Fig.6). Apatites

analysed within veins (Ap_{vein}) are also plotted and are assumed to represent a purely hydrothermal endmember. The compositions of the Ap_{mtrx} correspond to the vein apatites and the graph shows a trend in the apatite composition reflecting the magmatic and magmatic-hydrothermal portions of the porphyry system.

In addition, Ap_{mtrx} and Ap_{incl} analsyes from the late quartz porphyry display the smallest differences in composition, with a lot of overlap in the data (Fig. 5). If Ap_{mtrx} chemistry is a result of re-equilibration, this observation can be explained by the late emplacement of the quartz porphyry and its exposure to limited volumes of hydrothermal fluids as indicated by the lack of associated alteration and copper mineralisation.

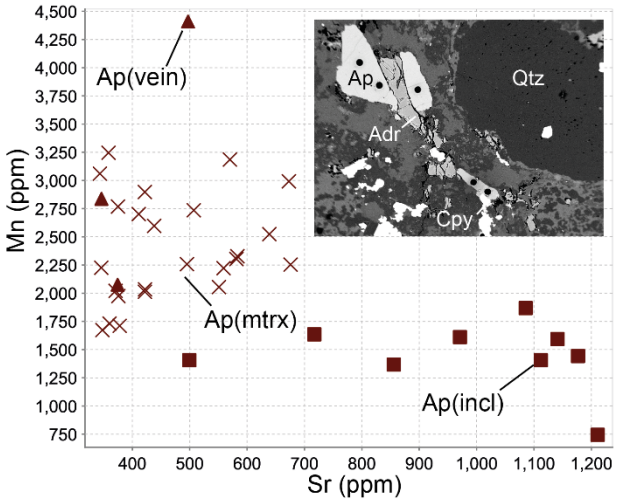

Figure 6. Plot of Mn (ppm) against Sr (ppm) from LA-ICP-MS analyses of Ap_{incl} (squares) and Ap_{mtrx} (crosses) from the dacite porphyry. Vein apatite composition, for grains found within the same sample (BSE image inset), are plotted as triangles.

7 Conclusions

At La Granja, apatite in porphyritic rocks found as inclusions in zircon have different compositions to apatite in the groundmass. It is proposed that the difference is a result of the groundmass apatite (Ap_{mtrx}) having re-equilibrated with a fluid. The results of this work have implications for the application of apatite as an indicator mineral; the composition of apparently fresh apatite in porphyry systems may represent later fluid events that may be associated with mineralisation.

The composition of apatite hosted in zircon (Ap_{incl}) is thought to preserve the original magmatic composition more faithfully than Ap_{mtrx} due to the protective properties of the zircon host. Future work will build on this idea, Apincl from porphyry rocks at La Granja will be compared to Apincl from older, barren Eocene igneous rocks from the area in order to compare characteristics between porphyry forming, and non-porphyry forming melts.

Acknowledgements

This PhD project is funded by a NERC Industrial Case studentship award (NE/N007883/1) to JJW, with additional funding from Rio Tinto. We thank Paul Agnew at Rio Tinto for his support of this research project and the Rio Tinto team at La Granja, Peru for their help in the collection of the samples used in this study.

References

Bruand E, Storey C, Fowler M (2016) An apatite for progress: inclusions in zircon and titanite constrain petrogenesis and provenance. Geology 2:91-94

Cherniak DJ (2010) Diffusion in accessory minerals: zircon, titanite, apatite, monazite and xenotime. Reviews in Mineralogy and Geochemistry 77:827-869

Dua DF, Jiang SY (2018) Using apatite to discriminate synchronous ore-associated and barren granitoid rocks: a case study from the Edong metallogenic district, South China. Lithos 369-380

Jennings ES, Marschall HR, Hawkesworth CJ, Storey CD (2011) Chracterization of magma from inclusions in zircon: Apatite and biotite work well feldspar less so. Geology 39:863-866

Meyers JS (1975) Vertical crustal movements of the Andes in Peru. Nature 254:672-674

Rio Tinto Annual Report (2018) 276

Schwartz MO (1982) The porphyry copper deposit at La Granja, Peru. Economic Geology 77:482-488

Stormer JC, Milton JR, Pierson L, Tacker RC (1993) Variation of F and Cl X-ray intensity due to anisotropic diffusion in apatite during electron microprobe analysis. American Mineralogist 78:5-6

Webster JD, Piccoli PM (2015) Magmatic apatite: a powerful, yet deceptive, mineral. Elements 11:177-182

Young E, Myers A, Munson E (1969) Mineralogy and geochemistry of fluorapatite from Cerro de Mecado, Durango, Mexico. Geological Survey Research 4:84-89

Using PGE geochemistry to assess magma fertility in the Polo Sur and Penacho Blanco porphyry copper deposits, Centinela District, Northern Chile

Carlos I. Carrasco-Godoy and Ian H. Campbell
The Australian National University

Abstract. The Centinela District is host to several mineralized porphyries, including both Cu-only and Cu-Au deposits. This study focusses on the known Polo Sur and Penacho Blanco porphyry Cu±Mo deposits as cases of study to assess their Cu-Au fertility.

PGE are sensitive indicators of sulphide saturation in silicate melts due to their strong partitioning into sulphide melts. They also have relatively low mobility in hydrothermal fluids, minimizing any effects of addition during hydrothermal alteration. If a parent magma reaches sulphide saturation early in its history, an immiscible sulfide melt will extract chalcophile metals trapping them at depth, potentially preventing them from entering the volatile ore-forming phase. In contrast, if sulphide saturation occurs close to the time of volatile saturation, or does not occur, then metals will be available to enter the fluid phase to form a deposit.

Thirty igneous rock samples from both deposits were analysed for major and trace elements. A subset of these samples were analysed to determine their PGE concentrations. Preliminary results suggest that sulphide saturation may occurr before the MgO content of magmas at Penacho Blanco fell below 3.5 wt.% but the timing of sulfide saturation, if it occurred at all, at Polo Sur is unclear.

1 Introduction

Copper is one of the most widely used metals in our society and it is essential in electronics, vehicles, telecommunications, electrical power generation and distribution systems, industrial and domestic piping, chemicals, currency and general infrastructure (Mudd and Jowitt 2018). The main source of this metal is porphyry copper deposits which provide nearly three-quarters of the world´s copper and a fifth of its gold (Sillitoe 2010; Mudd and Jowitt 2018). It is estimated that the demand for metals doubles every 20-30 years, but, in contrast, the average discovery rate of economic deposits is falling each year (Schodde 2017). For this reason, it is important to reach a better understanding of the processes that form these deposits, which can help us sustain the copper supply in future decades.

Porphyry ore deposits are related to igneous rocks, usually of dioritic to granitic composition, that form in magmatic belts above subduction zones (Richards 2003; Seedorff et al. 2005; Sillitoe 2010; Audétat and Simon 2012; Wilkinson 2013). The magmas produced in this setting are usually of basaltic composition, hydrated and oxidized, and ascend until they reach the base of the crust where they stagnate due to the contrast of density (Richards 2003). Here, they evolve to more felsic compositions that are able to ascend to upper crustal levels where a decrease in temperature and pressure can lead to the exsolution of a volatile phase (Wilkinson 2013, and references therein). These fluids can transport metals and have the potential to develop ore systems, known as porphyry copper deposits. However, not all porphyry systems contain economic concentrations of metals, and 'barren' systems share many features with fertile ones. Although there is an understanding of the general processes that can lead to a mineralized system, the factors that control the fertility of porphyry systems remain unclear (Wilkinson 2013, and references therein).

The aim of this project is to test the hypothesis that the timing of sulfide saturation, relative to volatile saturation, is an important factor controlling the type (Cu or Cu-Au) and fertility of porphyry systems from the Centinela District, Northern Chile. If a parent magma reaches sulfide saturation before volatile saturation, an immiscible sulfide melt will form, which will extract chalcophile metals, such as Cu and Au, and may trap them at depth so that they are unable to enter the volatile ore-forming phase (Fig. 1A), potentially resulting in a barren system. In contrast, if volatile saturation occurs before sulfide saturation, if the fraction of immiscible sulfide to form is small, if the time difference between these events is short, or if does not happen, most of the metals will remain in the melt and be available to enter the fluid phase and form an economic Cu or Cu-Au deposit (Fig. 1B). To address this aim, two porphyries from the Centinela District were studied, Penacho Blanco and Polo Sur.

Recent advances in platinum group element (PGE) analysis, developed at the Research School of Earth Sciences (RSES) at the Australian National University (ANU), are allowing analysis of PGE at ultra-low concentrations (Park et al. 2012a). Therefore, it is now possible to study rocks with low abundance of these elements, such as felsic suites, including the rock types associated with porphyry copper deposits. The PGE have been demonstrated to be sensitive indicators of sulfide saturation due to their high partition coefficients into sulfide melts (Mungall and Brenan, 2014). Furthermore, they are substantially less mobile in hydrothermal fluids than Cu and Au (Park et al., 2016) so are less likely to be impacted by post-magmatic hydrothermal addition .

Recent studies used PGE geochemistry to establish the timing of sulfide saturation in the El Abra porphyry Cu deposit in Northern Chile (Cocker et al. 2015) and in the

Cu-Au deposits of the Northparkes region, New South Wales, Australia (Hao et al. 2017). The latter work also included barren suites from the same region allowing the PGE geochemistry of barren rocks to be contrasted with the mineralized bodies. The results suggest that sulfide saturation occurred at earlier stages of magmatic differentiation for the non-mineralized suites than in the Cu-Au porphyries, where sulfide saturation occurred slightly before volatile saturation. Moreover, the results from the El Abra porphyry copper system showed that sulfide saturation occurred earlier than at Northparkes, which is consistent with the former being a Cu-only (gold removed early by limited sulfide saturation) and the latter being a Cu-Au deposit.

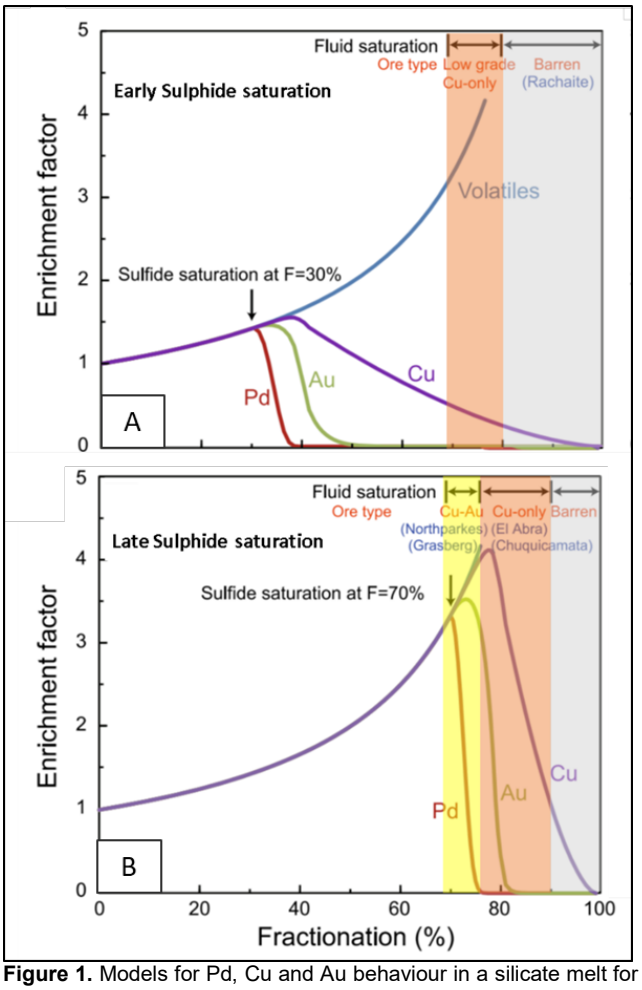

Figure 1. Models for Pd, Cu and Au behaviour in a silicate melt for early (A) and late (B) timing of sulfide saturation. Modified from Park et al. (2018).

2 Geological Background

The Centinela District, located in northern Chile, is part of the middle Eocene to early Oligocene metallogenetic belt which contains a number of renowned deposits like Chuquicamata and La Escondida (Sillitoe and Perelló 2005). The Centinela District forms a NE-trending block of approximately 40 km length and 25 km width, limited by the Coastal Cordillera to the west and the Domeyko Cordillera to the east. It is associated with the northern tip of the Sierra de Varas Fault, part of the Domeyko Fault System which is related to most of the mineralization in this belt (Perelló et al. 2010; Mpodozis and Cornejo 2012).

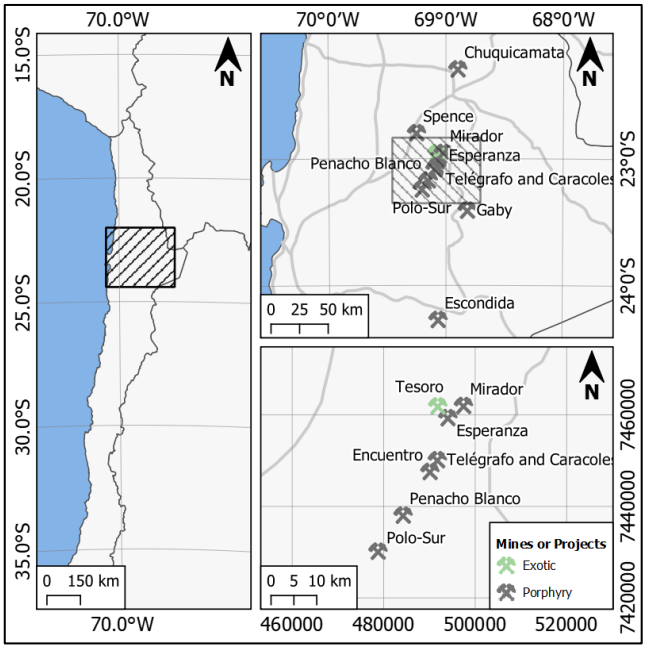

Figure 2. Map showing the location of the Centinela District and the principal mines and projects.

The district is host to at least seven identified mineralized porphyries, including both Cu-only and Cu-Au deposits, and has accounted for nearly 24.8 Mt of refined copper by 2017 (Antofagasta Minerals plc, 2017). Encuentro (41 Ma) and Esperanza (42 Ma) are currently being mined, together with exotic copper deposits at Tesoro and Mirador (Fig. 2). These features make the district a perfect natural laboratory to test whether the timing of sulfide saturation relative to volatile saturation affects the nature of the mineralization (i.e. Cu or Cu+Au).

The Penacho Blanco (formerly Centinela) and Polo Sur deposits account for the 25% of the resources known in the district, with 1.25 Mt contained Cu in the former and 5.14 Mt in the latter (Perelló et al. 2010; Antofagasta Minerals plc 2017). These are the oldest deposits in the district with dates between 45-44 and 42-41 Ma, respectively, and are classified as Cu-Mo porphyries (Perelló et al. 2010; Mpodozis and Cornejo 2012).

Penacho Blanco comprises subvertical cylindrical bodies of granodioritic composition hosted in volcanic rocks and a pre-mineralization diorite. Its alteration pattern is concentric with a central potassic zone overprinted by sericitic alteration. The main hypogene mineralization is dominated by chalcopyrite with an important and well-developed blanket of secondary sulfides that include chalcocite and covellite. The oxidation zone is not well developed and marginal (Perelló et al. 2010).

The Polo Sur porphyries are irregular to cylindrical bodies of dacitic composition emplaced in Paleocene to early Eocene volcanic rocks. Its alteration zonation is concentric with a potassic core overprinted by sericitic

alteration that grades to propylitic alteration laterally and it is capped by an advanced argillic lithocap. The sulfide mineralization is mainly chalcopyrite with minor bornite and, in contrast to Penacho Blanco, the oxidation zone is well developed (Perelló et al. 2010).

3 Samples and Methods

A representative group of samples from the deposits were selected according to two main criteria: i) unmineralized samples with a low intensity of alteration were preferred; ii) to encompass the full compositional range of the igneous rocks. Fifteen samples from Penacho Blanco and thirteen from Polo Sur ranging from diorites to dacite porphyries were studied. Three samples of rhyodacite porphyry from the TYC (Telégrafo and Caracoles, Fig. 2) area, which correspond to the youngest porphyries (39 Ma) in the district, were included to extend the temporal range.

Samples were cleaned of visible veinlets and ground in an in-house hardened case soft iron mill until grit-free. Major elements were determined at Intertek Genanalysis in Perth, Australia, by Li-borate fusion and analysis by XRF. Trace elements were analyzed by LA-ICP-MS in fused glass beads using a Lambda Physic Complex 110 excimer laser coupled with an ANU-designed HelEx ablation cell and an Agilent 7700x ICP-MS.

Twenty-three samples were selected based on composition to span the range from the most mafic member (highest MgO content) to the most felsic (lowest MgO). These were analyzed for PGE using the isotopic dilution, Ni-sulfide fire assay method described by Park et al. (2012). Concentrations of monoisotopic Rh and Au were calculated by the method described by Meisel et al. (2003) and Park et al. (2012b), using the ratio between ^{103}Rh and ^{106}Pd and ^{197}Au and ^{194}Pt, respectively, assuming that the loss of each element was similar during the analytical procedure. Eighteen duplicate samples were analyzed to evaluate the possible impact of PGE heterogeneity in the samples.

4 Results and discussions

The results from major and trace elements indicate that the magmas from Polo Sur and Penacho Blanco are typical calc-alkaline series with a subduction zone signature of Nb depletion and Pb enrichment.

The rare earth element patterns, normalized to chondrite are spoon-shaped, with an enrichment of LREE and depleted in MREE. The europium anomaly varies from slightly positive to slightly negative. The rocks from both deposits present a sub-adakite to adakite-like signature with high values of Sr/Y and La/Yb, especially in the more felsic samples. This signature has been proposed to result from a high water content of the magma (>2%) that suppresses plagioclase crystallization in early differentiation stages and promotes fractional crystallization dominated by hornblende (Richards and Kerrich 2007, and references therein).

Preliminary results show that the MgO content varies between 0.6 to 3.5 wt. % with one high value at 5.5 wt.% and that Pt and Pd vary from 0.01 to 1.85 and 0.04 to 3.27 ppb, respectively. The results from duplicates yield values that lie close to the corresponding original values (Fig. 3).

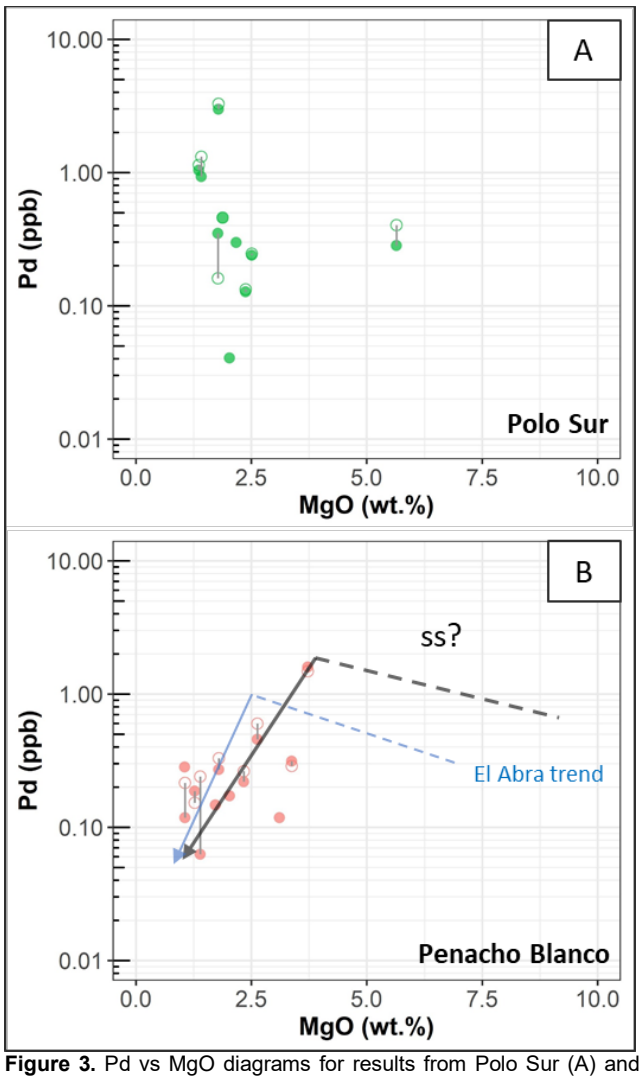

Figure 3. Pd vs MgO diagrams for results from Polo Sur (A) and Penacho Blanco (B). Duplicate analyses are linked by a grey line and shown by an open circle.

Pd is the most appropriate element to identify the onset of sulfide saturation because it accumulates in the melt up to sulfide saturation and then drops abruptly following saturation (Park et al. 2013). There is no obvious trend in the Polo Sur data. Thus, it is not possible to identify a sulfide saturation signature in this deposit (Fig. 3A). There is a weak trend of decreasing Pd with decreasing MgO for the Penacho Blanco samples, however, it may be possible to assume that sulfide saturation happened before 3.5 wt.% MgO (Fig. 3B). The trend and values are similar to those observed in the Cu-only El Abra porphyry deposit (Fig. 3B; Cocker et al. 2015).

Although the samples span dioritic to rhyodacitic compositions, it was not possible to establish evidence for a clear onset of sulfide saturation for these deposits. However, the geochemistry still reflects the nature of the processes involved in the formation of porphyry copper

deposits. According to the chalcophile element fertility diagram (Fig. 4) of Park et al. (2018) they are classified as mainly porphyry Cu-Only deposits . A group of Polo Sur samples fall in the Cu-Au area which may be related to small amounts of gold (0.06 g/t) reported in sulfides (Antofagasta Minerals plc 2017)

Finally, the study of the PGE geochemistry of felsic rocks gives us a proxy to better understand how sulfides behave in magmatic systems related to porphyry copper deposits which frequently are overprinted by hydrothermal alteration.

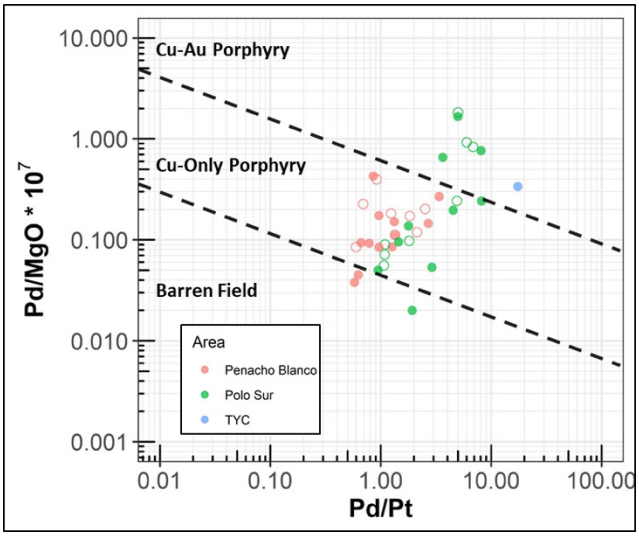

Figure 4. Chalcophile element discriminator from Park et al. (2018). Most of the samples fall into the Cu-Only field. Open circles indicate duplicate analyses.

Acknowledgements

This work was funded by the ARC Discovery Project DP17010340 to Ian Campbell and Andrew Berry. CCG acknowledges Antofagasta Minerals for their support collecting samples, specially Pepe Perello, Constantino Mpodozis, Pedro Apablaza and Leonardo Torres. Special thanks to Paula Cornejo and Jaime Osorio for their support and discussions at the beginning of this project. This program was funded by CONICYT PFCHA/MAGISTER BECAS CHILE/2017 – 73180502.

References

Antofagasta Minerals PLC (2017) Annual Report and Financial Statements 2017 - Antofagasta Minerals PLC. http://www.antofagasta.co.uk/investors/reports-presentations/

Audétat A, Simon AC (2012) Chapter 21 Magmatic Controls on Porphyry Copper Genesis. SEG Spec Publ 16:553–572

Cocker HA, Valente DL, Park JW, Campbell IH (2015) Using platinum group elements to identify sulfide saturation in a porphyry Cu system: The El Abra porphyry Cu deposit, Northern Chile. J Petrol 56:2491–2514. doi: 10.1093/petrology/egv076

Hao H, Campbell IH, Park JW, Cooke DR (2017) Platinum-group element geochemistry used to determine Cu and Au fertility in the Northparkes igneous suites, New South Wales, Australia. Geochim Cosmochim Acta 216:372–392. doi: 10.1016/j.gca.2017.05.009

Meisel T, Fellner N, Moser J (2003) A simple procedure for the determination of platinum group elements and rhenium (Ru, Rh, Pd, Re, Os, Ir and Pt) using ID-ICP-MS with an inexpensive on-line matrix separation in geological and environmental materials. J Anal Atom Spectrom 18:720. doi: 10.1039/b301754k

Mpodozis C, Cornejo P (2012) Cenozoic Tectonics and Porphyry Copper Systems of the Chilean Andes. SEG Spec Publ 16: 329–360

Mudd GM, Jowitt SM (2018) Growing Global Copper Resources, Reserves and Production: Discovery Is Not the Only Control on Supply. Econ Geol 13:1235–1267. doi: 10.5382/econgeo.2018.4590

Mungall JE, Brenan JM (2014) Partitioning of platinum-group elements and Au between sulfide liquid and basalt and the origins of mantle-crust fractionation of the chalcophile elements. Geochim Cosmochim Acta 125:265–289. doi: 10.1016/j.gca.2013.10.002

Park J-W, Campbell IH, Arculus RJ (2013) Platinum-alloy and sulfur saturation in an arc-related basalt to rhyolite suite: Evidence from the Pual Ridge lavas, the Eastern Manus Basin. Geochim Cosmochim Acta 101:76–95. doi: 10.1016/j.gca.2012.10.001

Park J-W, Campbell IH, Eggins SM (2012a) Enrichment of Rh, Ru, Ir and Os in Cr spinels from oxidized magmas: Evidence from the Ambae volcano, Vanuatu. Geochim Cosmochim Acta 78:28–50. doi: 10/bz7n4b

Park JW, Campbell IH, Kim J (2016) Abundances of platinum group elements in native sulfur condensates from the Niuatahi-Motutahi submarine volcano, Tonga rear arc: Implications for PGE mineralization in porphyry deposits. Geochim Cosmochim Acta 174:236–246. doi: 10.1016/j.gca.2015.11.026

Park J-W, Campbell IH, Malaviarachchi SPK, et al (2018) Chalcophile element fertility and the formation of porphyry Cu ± Au deposits. Miner Deposita. doi: 10.1007/s00126-018-0834-0

Park JW, Hu Z, Gao S, et al (2012b) Platinum group element abundances in the upper continental crust revisited - New constraints from analyses of Chinese loess. Geochim Cosmochim Acta 93:63–76. doi: 10.1016/j.gca.2012.06.026

Perelló J, Muhr R, Mora R, et al (2010) Chapter 13 Wealth Creation through Exploration in a Mature Terrain : The Case History of the Centinela District , Northern Chile Porphyry Copper Belt. Econ Geol Spec Publ 15:229–252

Richards JP (2003) Tectono-Magmatic Precursors for Porphyry Cu-(Mo-Au) Deposit Formation. Econ Geol 98:1515–1533

Richards JP, Kerrich R (2007) Special Paper: Adakite-Like Rocks: Their Diverse Origins and Questionable Role in Metallogenesis. Econ Geol 102:537–576. doi: 10.2113/gsecongeo.102.4.537

Schodde R (2017) Long term trends in global exploration – are we finding enough metal?. https://www.minexconsulting.com/publications/oct2017b.html

Seedorff E, Dilles JH, Proffett JM, et al (2005) Porphyry Deposits: Characteristics and Origin of Hypogene Features. Econ Geol 100th Anniversary Volume:251–298

Sillitoe RH (2010) Porphyry Copper Systems. Econ Geol 105:3–41. doi: 10.2113/gsecongeo.105.1.3

Wilkinson JJ (2013) Triggers for the formation of porphyry ore deposits in magmatic arcs. Nat Geosci 6:917–925. doi: 10.1038/ngeo1940

Titanite petrology and chemistry from the Strontian Igneous Complex, Scotland

Tom Matthews[1,2]*, Jamie Wilkinson [1,2] and Matthew Loader[1,2]
[1]*Department of Earth Sciences and Engineering, Imperial College London, UK*
[2]*LODE, Department of Earth Sciences, Natural History Museum, UK*

Abstract. Whole rock Sr/Y and mineral indicators are commonly employed to assess porphyry Cu fertility. Despite the favourable characteristics of titanite, its utility as an indicator of porphyry Cu fertility has not been evaluated. Magmas of the Strontian Igneous Complex exhibit a fertile Sr/Y signature but are not associated with a known porphyry. Titanite petrology and trace element chemistry from the Strontian Igneous Complex suggests that titanite may track petrogenetic processes that influence porphyry Cu fertility. Furthermore, titanite crystallisation may affect the utility of other mineral indicators in assessing porphyry Cu fertility.

1 Introduction

The ability of accessory minerals to sequester large quantities of trace elements from a melt is crucial to understanding melt evolution. Accessory minerals can be used for geochronology and can also indicate intensive parameters such as temperature and fO_2. In a world where ore deposits are becoming increasingly scarce, utilisation of accessory phases to better understand the genesis of magmatic-related ore deposits is of particular relevance. Magmas associated with porphyry Cu deposits (PCD's) are typically hydrous, oxidised and exhibit anomalously high Sr/Y. However, the factors that control porphyry fertility are not well constrained.

Titanite ($CaTiSiO_5$) can incorporate a variety of trace elements (e.g. REE, HFSE and LILE), demonstrating excellent preservation of primary magmatic textures that can be identified using backscattered electrons (BSE). Titanite has been employed as a geochronometer (Frost et al. 2000), as a thermometer (Hayden et al 2008) and has been suggested to track magma mixing (Piccoli et al. 2000). Despite this, the utility of titanite as a fertility indicator has not yet been explored.

The Strontian Igneous Complex (SIC) displays a 'fertile' Sr/Y signature with no known associated PCD. Hence, the SIC either signifies an eroded PCD, or a fertile magma that failed to form a PCD. The SIC also represents a rare opportunity to study the genesis of a fertile igneous rock that has experienced relatively minor alteration. Textural and trace element data of titanite grains from the SIC are presented hereafter.

2 Strontian Igneous Complex

The Strontian Igneous Complex (SIC) is a ~25km long calc-alkaline pluton that was emplaced into Moine metasediments of the Northern Highlands Terrane, during the late Caledonian orogeny (Atherton & Ghani 2002; Bruand et al. 2014; Fig. 1). The SIC is one of several plutons of the Argyll and Northern Highlands suite, that exhibit anomalous Sr and Ba whole rock concentrations, which have previously been attributed to assimilation of carbonate rich sediments (Fowler et al. 2008).

The SIC exhibits normal zonation comprising zones of: (outer to inner) quartz diorite, quartz monzonite and biotite granite. The SIC is crosscut by diorite dykes, that are in turn crosscut by felsite dykes (Birt 2019). Mafic enclaves are common within the SIC, on the cm to >100 metre scale. U-Pb dating of zircon and titanite from the quartz monzonite yield ages of 425 ± 3Ma and 423 ± 3Ma respectively (Rogers & Dunning 1991).

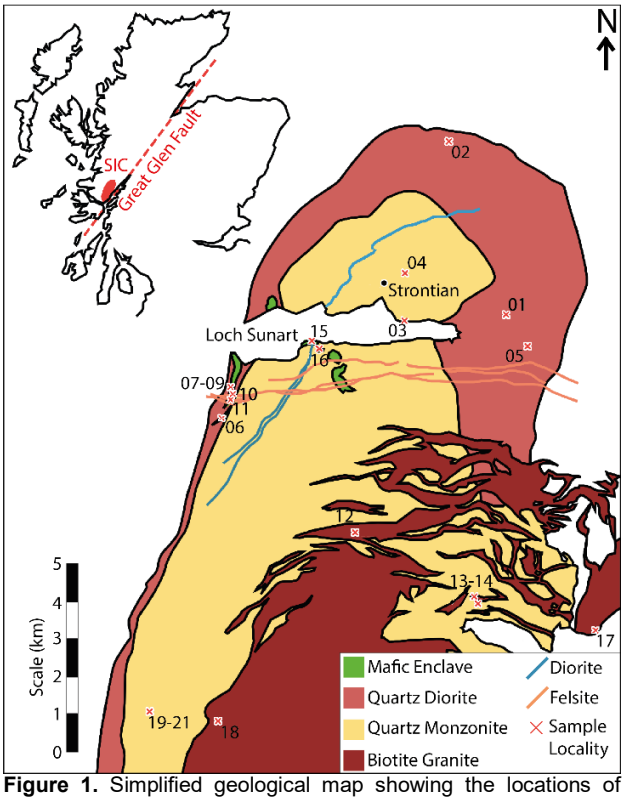

Figure 1. Simplified geological map showing the locations of samples used for this study (Adapted from Birt 2019).

3 Methods

Samples were collected from the main intrusive units of the SIC, and their locations are shown by Fig. 1. These

were subsequently prepared into thin sections, prior to analysis at the Natural History Museum, London. 10 thin sections were selected for analysis (01, 03, 07, 09, 10, 13, 15, 16, 19, 21) based on the size and abundance of titanite.

Titanites were imaged and analysed using a Zeiss EVO SEM, with a beam current of 3 nA and an accelerating voltage of 20kV. Backscatter electron (BSE) imaging was employed to reveal titanite zonation and major element data was collected by energy dispersive spectroscopy (EDS). EDS was also employed to identify mineral inclusions in titanite grains. Trace element analysis was conducted using an ESI New Wave Research 193nm excimer laser coupled to an Agilent 7700cs quadrupole ICP-MS. Ca, as determined by quantitative SEM analysis, was employed as the internal standard and NIST-610, GSD-1G and BCR-2G glasses were used as primary, secondary and tertiary external standards respectively. The laser was operated with a 10 Hz frequency, a fluence of 3.5 J cm^{-2} and a spot size of 30 μm.

4 Results

4.1 General characteristics

Titanite is present in all lithologies except the felsite, which has therefore been excluded from this study. However, within the biotite granite titanite grains are only present in sample 13, which is close to the contact with the quartz monzonite. Titanite exhibits modal abundances of 1-4%, with crystals ranging from 0.1-1.5mm in length. BSE images reveal that zoning in titanite is ubiquitous, and individual grains display one or several of the following types: sector, normal, oscillatory and patchy (Fig. 2).

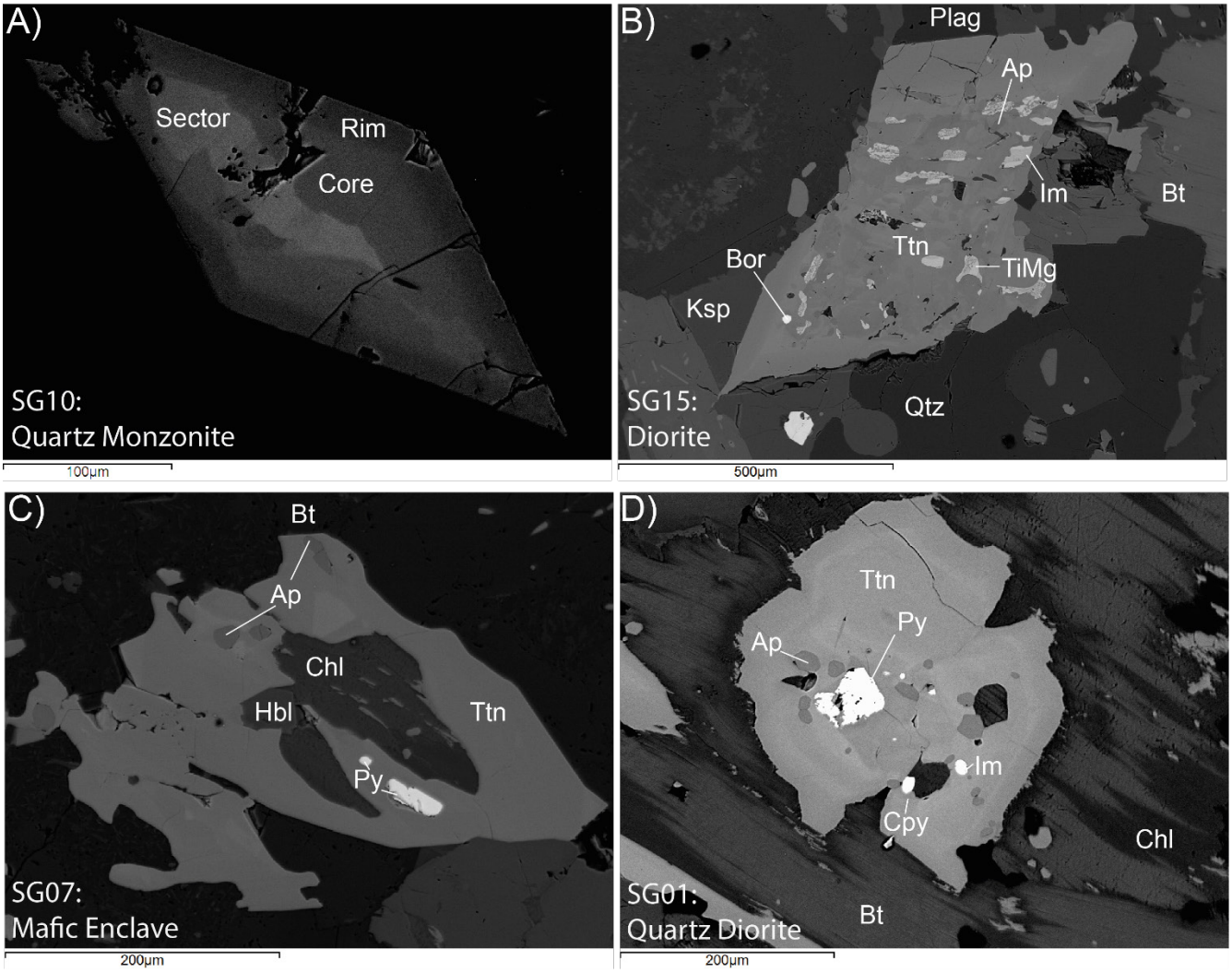

Figure 2. SEM-BSE images of titanites from the SIC. (a) Euhedral titanite showing normal and sector zoning. (b) Subhedral titanite showing patchy zoning and partial dissolution. The core contains bornite, apatite and Fe-Ti oxide inclusions. Apatites are included in both core and rim. (c) Interstitial sector zoned titanite containing pyrite, apatite, chlorite and hornblende inclusions. (d) Interstitial reverse zoned titanite containing pyrite, chalcopyrite, ilmenite and apatite inclusions.

4.2 Lithological variation

A range of crystal habits and phase relationships are observed within the same rock, and between lithologies. In the quartz monzonite and biotite granite titanite is commonly euhedral, occurring as inclusions within mafic minerals e.g. hornblende and biotite (Fig. 2a). In the quartz diorite, diorite and mafic enclaves, titanite is typically anhedral and included in feldspars (Fig. 2b-d). Apatite inclusions are present in most grains, whilst zircon inclusions are less common. Devitrified melt inclusions are also common, comprising quartz + feldspar.

Sulphides (pyrite, chalcopyrite and bornite) are included within grains from the quartz diorite, diorite and mafic enclaves, but are absent from the quartz monzonite and biotite granite. Zones that are rich in unmixed Fe-Ti oxide inclusions are present in all lithologies and are often associated with patchy zoning, partial dissolution or sulphide inclusions. These Fe-Ti oxide inclusion zones are found exclusively in grain cores in all lithologies, except the biotite granite, where they are also observed in rims.

4.3 Titanite chemistry

Trace element concentrations of titanite grains from all lithologies, show core to rim variations (Fig. 3). All grains exhibit marked reductions in the concentrations of HREE and LREE, with a broadly consistent ratio of ~1:1. Core to rim variation in Sr/Y is dominated by Y, which is highly variable (250 – 2500 ppm) in comparison to Sr (60 – 90 ppm). Whilst Sr typically shows minimal variation from core to rim, Y is strongly depleted.

5 Discussion

Sulphide and Fe-Ti oxide inclusions are interpreted to be of magmatic origin, due to their presence only in particular zones. The presence of Fe-Ti oxide inclusion zones has previously been suggested to indicate magma mixing events. Piccoli et al. (2000) suggested that the introduction of hotter, more primitive magmas with a lower fO_2 could stabilise ilmenite over titanite and result in the partial resorption of titanite. If Fe-Ti oxide inclusion zones represent magma mixing events, then their omnipresence would suggest that magma mixing was widespread in the SIC. This is supported by the common occurrence of mingling textures between felsic magmas and mafic enclaves observed in the field. The confinement of these Fe-Ti oxide inclusion zones to grain cores (excluding the biotite granite) suggests that magma mixing typically occurred early during titanite crystallisation.

Where sulphide inclusions are found associated with Fe-Ti oxide inclusion zones, then sulphide saturation may be triggered by magma mixing. Nevertheless, the occurrence of sulphide inclusions within titanite indicates that titanite crystallised during magmatic sulphide saturation.

Titanite rims (relative to cores) are strongly depleted in REE and Y, representing systematic depletion in the residual melt. This depletion likely results from the crystallisation of REE-compatible phases such as titanite itself, or hornblende. Hence, any phases that crystallise following titanite saturation may also be strongly depleted in these components. This has important implications where REE and Y concentrations are utilised in mineral fertility indicators (e.g. zircon).

Our data suggests that titanite can be utilised to assess the importance of magma mixing and sulphide saturation in affecting porphyry Cu fertility. Furthermore, the saturation of titanite has the ability to strongly influence mineral indicators of porphyry fertility.

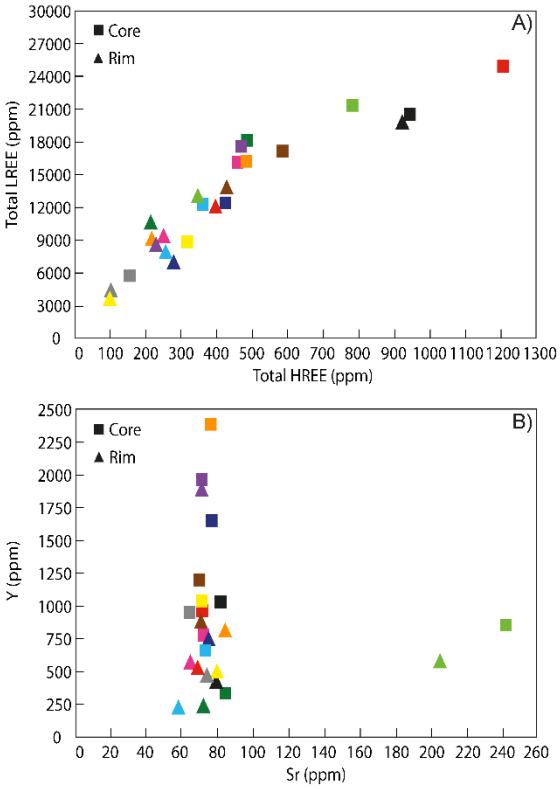

Figure 3. Core to rim trace element chemistry of titanite grains. Each colour represents core to rim variation in an individual titanite grain. (a) Total Heavy REE vs Total Light REE (b) Sr vs Y.

Acknowledgements

This study forms part of the lead author's PhD project, that is in part funded by Rio Tinto Exploration. Miranda Birt is thanked for the provision of samples. Yannick Buret (LA-ICP-MS), Tobias Salge (SEM) and John Spratt (SEM) are thanked for their assistance during the analyses.

References

Atherton, M.P. & Ghani, A.A. 2002. Slab breakoff: a model for Caledonian, Late Granite syn-collisional magmatism in the orthotectonic (metamorphic) zone of Scotland and Donegal, Ireland. Lithos, 62:65-85.

Birt, M.M., 2019. The generation of high Sr/Y in the Strontian Intrusive Complex. Unpublished MSci thesis, Imperial College London.

Bruand, E., Storey, C. & Fowler, M. 2014. Accessory mineral chemistry of high Ba–Sr granites from northern Scotland: constraints on petrogenesis and records of whole-rock signature. Journal of Petrology, 55:1619-1651.

Fowler, M.B., Kocks, H., Darbyshire, D.P.F. & Greenwood, P.B. 2008. Petrogenesis of high Ba–Sr plutons from the northern highlands Terrane of the British Caledonian Province. Lithos, 105:129-148.

Frost, B.R., Chamberlain, K.R. & Schumacher, J.C., 2001. Sphene (titanite): phase relations and role as a geochronometer. Chemical Geology, 172:131-148.

Hayden, L.A., Watson, E.B. & Wark, D.A., 2008. A thermobarometer for sphene (titanite). Contributions to Mineralogy and Petrology, 155:529-540.

Piccoli, P., Candela, P. & Rivers, M. 2000. Interpreting magmatic processes from accessory phases: titanite—a small-scale recorder of large-scale processes. Earth and Environmental Science Transactions of The Royal Society of Edinburgh, 91:257-267.

Rogers, G. & Dunning, G.R., 1991. Geochronology of appinitic and related granitic magmatism in the W Highlands of Scotland: constraints on the timing of transcurrent fault movement. Journal of the Geological Society, 148:17-27.

Wones, D.R. 1989. Significance of the assemblage titanite + magnetite+ quartz in granitic rocks. American Mineralogist, 74:744-749.

Magma fertility related to porphyry copper mineralization potential in Sangilo, Baguio Mineral District, Philippines

Jillian Aira Gabo-Ratio, Karl D. Jabagat
University of the Philippines

Naoto Kugizaki, Kotaro Yonezu
Kyushu University, Japan

Graciano P. Yumul, Jr.
Itogon Suyoc Resources Inc. - Apex Mining Company Inc., Philippines

Abstract. The Sangilo epithermal deposit is located in the Baguio Mineral District (BMD) in northern Luzon, Philippines. Epithermal mineralization in Sangilo is hosted by the Early Miocene dark-colored hornblende quartz diorite (HQD), Middle Miocene quartz diorite and Pliocene porphyritic andesite dikes. Recent exploration activities in the area reveal manifestations of an older porphyry copper mineralization hosted by the hornblende quartz diorite. The mineral chemistry of magmatic plagioclase and amphibole crystals in the Sangilo host rocks were thus investigated in order to relate magmatic conditions with porphyry copper mineralization potential. The physico-chemical calculations from amphibole mineral chemistry shows that the andesite has the highest calculated ranges of pressure, temperature and H_2O% in melt. These andesite dikes appear to be mantle-derived melts which triggered mineralization in the BMD during the Pliocene-Pleistocene. The hornblende quartz diorite on the other hand, which also reflected high water content and oxygen fugacity, might correspond to an earlier episode of mineralization (Early-Middle Miocene) which is responsible for the observed porphyry copper mineralization signature in the area.

1 Introduction

The increasing difficulty in discovering hydrothermal deposits led to the formulation of various exploration tools apart from conventional geophysical and geochemical methods. One of the challenges being addressed in recent works is assessing the fertility of a system by looking at the mineral chemistry of igneous source rocks as formational triggers. Fossil specimens of magmatic systems represented by igneous intrusive complexes offer a window into understanding the evolution of magmatic processes. These various processes are not only spatially and temporally, but also genetically critical to the onset of associated porphyry copper and epithermal gold mineralization (Sillitoe, 2010; Walker et al., 2013). Physico-chemical conditions (e.g. pressure, temperature, oxygen fugacity, H_2O percentage in melt) prevailing in the magmas during crystallization significantly govern the metallogenesis of hydrothermal systems. These conditions were inferred to vary on mineralized and barren magmatic bodies (Mason, 1978; Cao et al., 2018).

This study focuses on the Baguio Mineral District, which is a world-class district in terms of porphyry copper and epithermal mineralization. We evaluate the plutonic host rocks in Sangilo, a known epithermal gold deposit but with manifestations of porphyry copper mineralization recently observed in the underground mine workings. This study therefore looks into the magmatic and physico-chemical conditions and porphyry copper mineralization potential in Sangilo by investigating the mineral chemistry of plagioclase and amphibole crystals of the hornblende quartz diorite, tonalite and andesite host rocks.

2 Geologic Outline

2.1 Regional Tectonic Setting

Luzon island belongs to the Philippine Mobile Belt, which is an amalgamation of magmatic arcs, ophiolitic complexes, metamorphic terranes, sedimentary basins and continental fragments (Yumul et al. 2008). The island is bounded by oppositely dipping subduction zones: the east dipping Manila Trench to the west and the west dipping East Luzon Trough-Philippine Trench to the east (Figure 1). Excess stress generated by the oblique subduction along the Philippine Trench resulted in the formation of the left-lateral strike-slip Philippine Fault Zone (PFZ) transecting the island in a northwest-southeast trend (Aurelio 2000). Major and minor splays of the PFZ played a crucial role in the evolution of hydrothermal systems in north Luzon and the formation of metalliferous deposits (Bellon and Yumul 2000; Yumul et al. 2008).

2.2 Sangilo epithermal deposit

The Sangilo deposit is located in the Baguio Mineral District (BMD), which forms a 25-km-long and 7-km-wide north-trending belt located in the central portion of Luzon island. The BMD is host to world-class porphyry copper, epithermal gold and skarn deposits that are mostly Pliocene in age (Waters et al. 2011). The basement of the district consists of ophiolitic and metamorphic complexes overlain by Late Cretaceous to Quaternary volcanic arcs (Aurelio 2000; Hollings et al. 2011).

The BMD also hosts the Sangilo epithermal deposit in Itogon, Benguet that contain quartz-carbonate veins

linked to the N-W to E-W trending veins of Acupan to its west. Epithermal mineralization in Sangilo is hosted by three rock units: the Early Miocene dark-colored hornblende quartz diorite (HQD) of the Central Cordillera Diorite Complex, Middle Miocene quartz diorites of the Itogon Quartz Diorite and minor Pliocene porphyritic andesite dikes (Figure 1). Mineralized structural fabrics in Sangilo have three major orientations: NE, NNE and due west. These structures are related to the zone of dilation produced by the northerly splays of the Philippine Fault zone. These vein-filled structures cut the igneous host rocks suggesting that the epithermal veins are not genetically linked with them. In addition, recent underground mapping revealed the presence of stockwork veinlets and disseminated chalcopyrite and bornite, which was also reported in the adjacent Acupan as porphyry-type mineralization by Waters et al. (2011). This porphyry-type mineralization is only observed in the hornblende quartz diorite

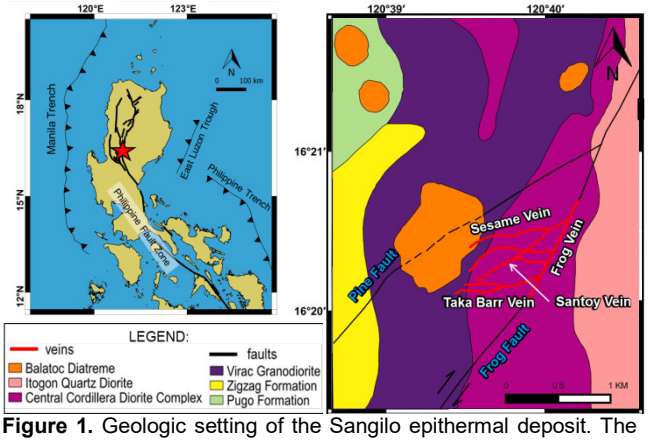

Figure 1. Geologic setting of the Sangilo epithermal deposit. The figure on the left shows Luzon Island and its tectonic features. The red star shows the location of the study area. The right figure shows the geologic map of the Sangilo epithermal deposit, including the major faults and veins that host the epithermal mineralization.

3 Petrography and Mineral Chemistry

The hornblende quartz diorite (HQD), which hosts most of the epithermal veins, is medium to coarse grained, holocrystalline, composed mainly of euhedral to subhedral plagioclase feldspar, hornblende and anhedral quartz together with accessory magnetite, apatite and zircon. Minor chlorite and epidote alteration is also evident. The relatively younger quartz diorite unit contains less hornblende and a higher percentage of quartz compared to the HQD. Plagioclase feldspars in the quartz diorite exhibits distinct zoning compared to the unzoned plagioclase in the hornblende quartz diorite. Porphyritic andesite dikes which post-dates both the aforementioned host units are composed of euhedral to subhedral plagioclase feldspars and subhedral amphiboles as phenocrysts set in a groundmass of plagioclase microlaths. Accessory magnetite minerals are also present in this unit. Minor sericite and calcite alteration is apparent.

Selected polished sections were analyzed by a JEOL-JXA 8230 electron probe microanalyzer at the National Institute of Geological Sciences, University of the Philippines. Amphiboles in the HQD are ferrohornblende in composition whereas amphiboles in the quartz diorite vary from magnesiohornblende to actinolite. Amphiboles from the basaltic andesite were classified as pargasite, which is a higher temperature and pressure variety of amphibole. Plagioclase in both the HQD and tonalite is dominated by zoned andesine with minor labradorite while plagioclase from the basaltic andesite is anorthite in composition.

4 Discussion

Physico-chemical calculations from amphibole mineral chemistry calculated from Ridolfi et al. (2010) shows that compared with the quartz diorite, the HQD has relatively higher calculated ranges of pressure (HQD: 100-142 MPa; quartz diorite: 88-96 Mpa; σest: 11-14 Mpa) (Figure 2A), temperature (HQD: 771-865°C; tonalite: 760-812°C; σest: 22°C) and H_2O% in melt (HQD: 5.1-6.4 wt.%; quartz diorite: 4.2-5.4 wt.%; σest: 0.4 wt%) (Figure 2B). The andesite, which is the youngest unit, has the highest values of pressure (300-350 MPa), temperature (957-968°C) and has a relatively high H_2O% in melt (4.6-5.2 wt%).

The crystallization depth was also calculated by the method of Ridolfi et al. (2010) using a crustal density value of 2890 kg/m^3. The calculated depths coincide with the calculated pressures and temperatures (Table 1). The hornblende diorite revealed depths of crystallization of 3.8-4.9 km. The quartz diorite reflected shallower crystallization depths ranging from 1.9-3.1 km. Amphiboles in the andesite reflected the deepest depths of crystallization ranging from 10.8-12.5 km. Oxygen fugacity computations showed high fO_2, with the HQD and andesite plotting above the NNO slope and the quartz diorite straddling the NNO+2 slope (σest: 0.4 logfO_2) (Figure 2C).

Varying magmatic sources were identified for the host rocks using the diagram of Jiang and An (1984) utilizing TiO_2 and Al_2O_3 wt% in amphiboles (Figure 2D). The basaltic andesites were sourced from mantle-derived melts that underwent minimum crustal contamination. The hornblende diorite plotted in the mixed crust and mantle derived melt suggesting a hybrid origin. Lastly, the quartz diorites both plotted in the hybrid and crust source suggesting higher degrees of crustal contamination compared to the HQD.

Recent studies like Wilkinson (2013) and Richards (2011) emphasized the role of factors such as high magmatic water content, relatively high oxidation states and high sulfur content in enhancing the fertility of arc magmas in generating hydrothermal ore deposits.

Based on the calculated physico-chemical conditions, the Middle Miocene quartz diorite is considered as barren. The barren nature of the intrusive can be explained by its crust-derived affinity suggesting minimum interaction with mafic melts during its formation which could have supplied ample amount of sulfur and water. This explanation is supported by the relatively lower magmatic water content reflected in the amphibole

chemistry.

The basaltic andesite dikes in Sangilo correspond to mafic-derived melts which interacted with silicic crustal melts during the Plio-Pleistocene resulting in the ubiquitous mineralization in the Baguio Mineral District. Addition of a more primitive melt increased sulfur content in the resulting hybrid magma. Aside from increasing the contained sulfur, formation of amphibole at depth suggests that the basaltic andesite has high initial water content which could also enhance fertile conditions in the resulting magma.

Lastly, the Early Miocene HQD is considered to be responsible for the older porphyry copper signature present in the area. Aside from field evidence, the mix crust-mantle signature of the HQD suggests interaction with primitive melt which is favorable for hydrothermal mineralization. This assumption is supported by high magmatic water content and oxygen fugacity calculated for the host rock.

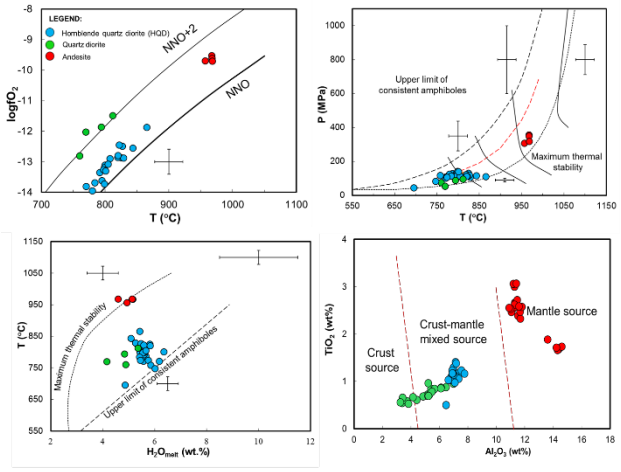

Figure 2. The pressure (A), temperature (B) and oxygen fugacity (C) of amphiboles based on diagrams by Ridolfi et al. (2010). (D) Source composition diagram of Jiang and An (1984)

5 Summary and Conclusions

This study investigated the mineral chemistry of the three intrusive rock units in Sangilo to look at the physico-chemical conditions during magmatism and assess their potential for porphyry copper mineralization. The mineral chemistry data indicates that the basaltic andesites has the highest calculated ranges of pressure, temperature and relatively high initial H_2O wt% in melt. These mantle-derived melts triggered mineralization in the BMD during the Pliocene-Pleistocene. The hornblende quartz diorite which also reflected high water content and oxygen fugacity, might correspond to an earlier episode of mineralization (Early-Middle Miocene) responsible for the observed porphyry copper mineralization signature in the area. These findings provide new insights into the link between physico-chemical conditions and fertility of intrusive bodies in the Baguio Mineral District.

Acknowledgements

The authors acknowledge the Itogon-Suyoc Resources Incorporated (ISRI), the Rushurgent Working Group Laboratory of the National Institute of Geological Sciences, University of the Philippines and the Economic Geology Laboratory of the Department of Earth Resources Engineering, Kyushu University for the logistical support and laboratory analyses. This study is partially funded by the University of the Philippines Office of the Vice President for Academic Affairs Balik-PhD Grant to the first author and by the Japan Society for the Promotion of Science Asia Africa Science Platform to the fourth author.

References

Aurelio MA (2000) Shear partitioning in the Philippines: Constraints from the Philippine fault and global positioning system data. Island Arc 9:584–597.

Bellon H, Yumul GPJr (2000) Mio-Pliocene magmatism in the Baguio mining district (Luzon, Philippines): Age clues to its geodynamic setting. C.R. Acad Sci., Ser. IIa: Sci. Terre Planets 331:295–302.

Cao, M., Evans, N. J., Hollings, P., Cooke, D. R., & Brent, I. A. (2018a). Phenocryst zonation in porphyry-related rocks of the Baguio District, Philippines: Evidence for magmatic and metallogenic processes. Journal of Petrology, 59 (5), 825-848.

Hollings P, Cooke DR, Waters PJ, Cousens B (2011) Igneous geochemistry of mineralized rocks of the Baguio district, Philippines: Implications for tectonic evolution and the genesis of porphyry-style mineralization. Econ Geol 106:1317–1333.

Mason, D. R. (1978). Compositional variations in ferromagnesian minerals from porphyry copper-generating and barren intrusions of the Western Highlands, Papua New Guinea. Economic Geology, 73(5), 878–890.

Ridolfi F, Renzulli A, Puerini M (2010) Stability and chemical equilibrium of amphibole in calc-alkaline magmas: An overview, new thermobarometric formulations and application to subduction-related volcanoes. Contrib Mineral Petrol 160:45–66.

Sillitoe, R. H. (2010). Porphyry copper systems Shannon, J. R. (1979). Igneous petrology, geochemistry and fission track ages of a portion of the Baguio mineral district, northern Luzon, Philippines: Unpublished M.Sc. thesis, Colorado School of Mines, Golden Colorado, 173 pp.

Waters PJ, Cooke DR, Gonzales RI, Phillips D (2011) Porphyry and epithermal deposits and $^{40}Ar/^{39}Ar$ geochronology of the Baguio district, Philippines. Econ Geol 106:1335–1363.

Walker, B. A., Klemetti, E. W., Grunder, A. L., Dilles, J. H., Tepley, F. J., & Giles, D. (2013). Crystal reaming during the assembly, maturation, and waning of an eleven-million-year crustal magma cycle: Thermobarometry of the Aucanquilcha Volcanic Cluster. Contributions to Mineralogy and Petrology, 165(4), 663–682.

Williamson BJ, Herrington RJ, Morris A. (2016) Porphyry copper enrichment linked to excess aluminium in plagioclase. Nat Geosci 9: 237.

Yumul GPJr, Dimalanta CB, Tam TA, Ramos EGL (2008) Baguio Mineral District: An oceanic arc witness to the geological evolution of northern Luzon, Philippines. Island Arc 17:432–442.

Role of breccias in porphyry copper formation

Richard H. Sillitoe
Independent consultant, London, England

Abstract. Three volumetrically important, cross-cutting breccia types can occur in association with porphyry copper ± molybdenum ± gold deposits: magmatic-hydrothermal, phreatomagmatic (diatreme), and phreatic, each reliant on a specific aqueous fluid-induced process and characteristic of a particular position in and evolutionary stage of deposit development. With few exceptions, these various hydrothermal breccias were generated during and after, rather than before, porphyry copper and overlying high-sulfidation epithermal gold ± silver deposit formation. They are located near the apices of and above their causative porphyry intrusions. Consequently, even where breccia bodies contain juvenile igneous material, they could not have controlled ascent of the magmas that gave rise to the main mineralized intrusions. The syn-mineral magmatic-hydrothermal breccias are blind, having failed to approach the paleosurface, so could not have been connected in any way to subaerial volcanism during porphyry copper formation. Indeed, available evidence requires that porphyry copper deposits are normally generated beneath non-brecciated roof rocks, which are generally much older than the deposits themselves. Any direct connection between porphyry copper systems and volcanic paleosurfaces is usually via phreatomagmatic diatremes and generally a late- to post-mineral event; however, in rare cases, porphyry copper stocks intruded early, pre-mineral diatremes.

1 Introduction

Hydrothermal breccias – fragmental rocks whose genesis involved hot aqueous fluids – are common and prominent features of porphyry copper ± molybdenum ± gold deposits worldwide. They typically constitute <10 volume % of the porphyry copper ore but, exceptionally, can approach 50% (e.g., Río Blanco-Los Bronces, Chile; Toro et al. 2012); however, breccias may be entirely absent (e.g., Chuquicamata, Chile; Rivera et al. 2012). Some breccias are economically important because they constitute the highest-grade parts of porphyry copper or overlying epithermal precious-metal deposits and, where suitably located, can be extracted early in mine lives to accelerate capital payback. The characteristics and relative timing of the principal breccia types in porphyry copper systems and the roles that they can and cannot play in deposit formation are the subjects of this brief review.

2 Breccia types

Three end-member breccia types can be volumetrically important in porphyry copper systems (Sillitoe 1985): magmatic-hydrothermal breccias, in close association with porphyry intrusions; phreatomagmatic (diatreme) breccias, rooted in intrusions but spanning the full vertical extents of the porphyry systems, including their lithocaps; and phreatic breccias, largely confined to the lithocap environment (Fig. 1).

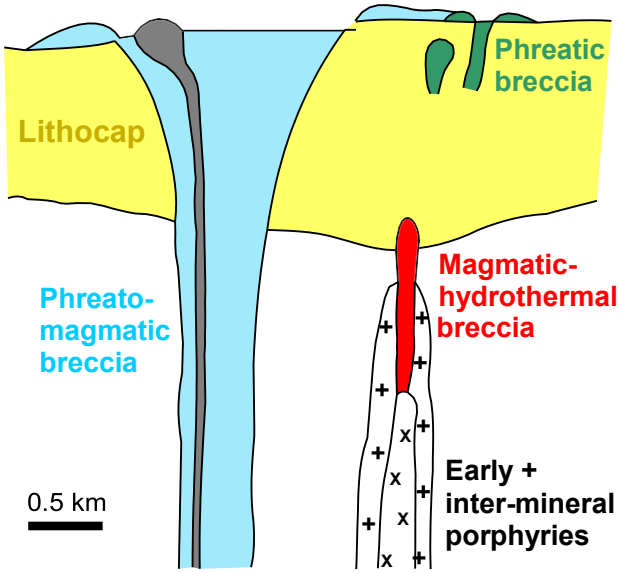

Figure 1. Cartoon to illustrate typical positions and relative timing of magmatic-hydrothermal, phreatomagmatic (diatreme), and phreatic breccias in porphyry copper systems

2.1 Magmatic-hydrothermal breccias

Magmatic-hydrothermal breccias, the products of over-pressured aqueous fluids following their exsolution from magma, are generally emplaced as irregular to pipe-like bodies during porphyry copper formation; they are closely associated with the upper flanks and tops of porphyry intrusions (Fig. 1), in common with which they display potassic alteration at depth and sericitic (± tourmaline) and, uncommonly, advanced argillic alteration at shallower levels (e.g., Río Blanco-Los Bronces; Irarrazaval et al. 2010; Toro et al. 2012). The breccia bodies, typically tens to hundreds of meters across and, locally, >1,000 m in vertical extent, can have gradational or abrupt host-rock contacts, the latter marked in places by vertically extensive zones of sheeting. The breccia bodies are blind, i.e. they typically do not extend far above the associated porphyry intrusions; however, some of the larger breccia volumes at Cananea in Mexico, Río Blanco-Los Bronces, and elsewhere can continue for hundreds of meters above their causative intrusions (Bushnell 1988; Toro et al. 2012).

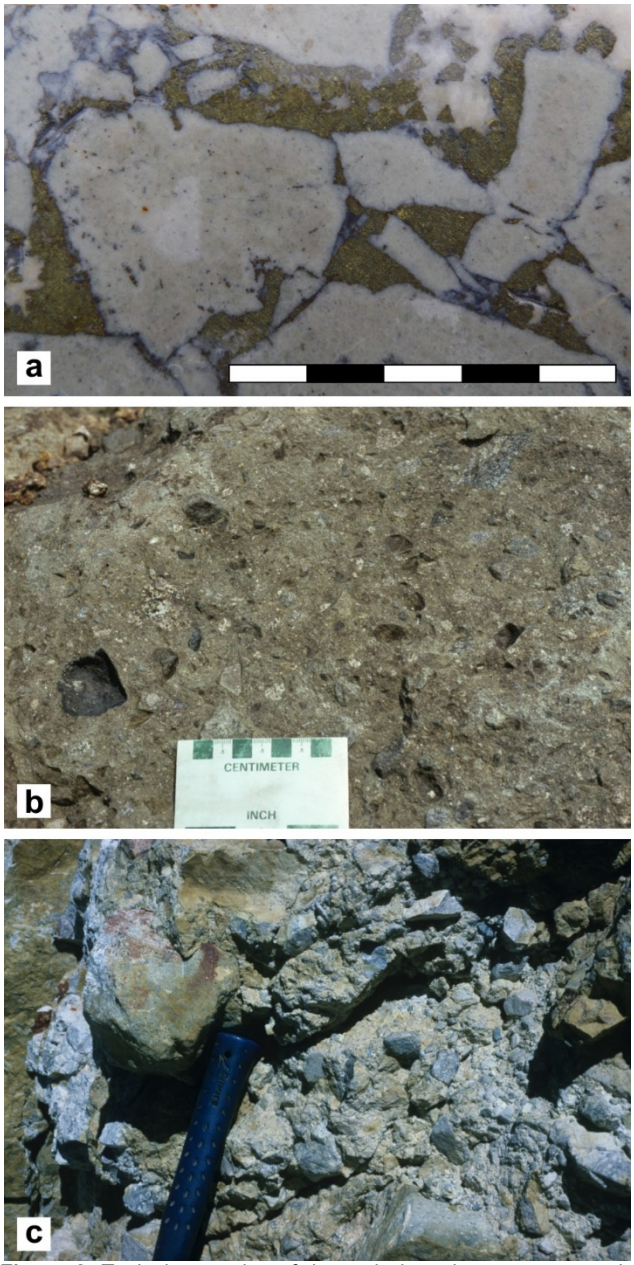

Figure 2. Typical examples of the main breccia types present in porphyry copper systems: **a** magmatic-hydrothermal, with monolithic, sericitic-altered clasts cemented by thin rinds of early tourmaline (gray-black) and later chalcopyrite (yellow); **b** phreatomagmatic, with small heterolithic clasts and casts after clasts (gray-black, lower left) in a tuff plus rock-flour matrix; **c** phreatic, with massively silicified clasts (gray) cemented by chalcedony (stained yellow by supergene jarosite). Centimeter scale bars and upper 15 cm of hammer handle for scale.

The breccia clasts are commonly subangular, monolithic, and match contiguous wall rocks, implying relatively limited vertical transport (Fig. 2a). Spheroidal clasts formed by hypogene exfoliation and alignment of high-aspect-ratio clasts are additional diagnostic features (Sillitoe 1985). Hydrothermal minerals, with or without comminuted rock (rock flour), can cement the clasts and, where copper sulfides are abundant (Fig. 2a), abnormally high grades can result; end-stage open space is typically filled by anhydrite. Magma can passively invade intra-clast space in the deeper parts of magmatic-hydrothermal breccia bodies, giving rise to what are termed igneous breccias (Gustafson and Hunt 1975).

2.2 Phreatomagmatic breccias

Phreatomagmatic breccias, products of explosive energy release during interaction between magma and hot aqueous solutions, commonly including ground water, fill kilometer-scale, upward-flared diatreme vents that can be vertically extensive (2–3 km; Fig. 1). Remnants of the magma bodies responsible for phreatomagmatism are observed to underlie and intrude the diatreme breccias as dikes (e.g., El Teniente, Chile; Howell and Molloy 1960) and shallow plugs, which may have attained the paleosurface as volcanic domes (e.g., Guinaoang, Philippines; Sillitoe and Angeles 1985; Fig. 1). Most diatremes breached the paleosurface to form maar volcanoes (Fig. 1) as confirmed by the presence within them of subsided blocks of base surge and lacustrine sedimentary deposits and chunks of carbonized wood. Accretionary lapilli are characteristic of these subaerial base surge deposits, but can also form within the diatreme vents themselves.

The breccias are predominantly heterolithic, matrix supported, and highly milled (Fig. 2b) and, by definition, contain juvenile igneous material: broken crystals (tuff) admixed with the rock-flour matrix and/or wispy, plastically deformed clasts of either dense or vesicular magma. Diatreme breccias generally display low-temperature clay alteration and disseminated grains of pyrite although, at the shallow lithocap level (Fig. 1), some diatremes were subjected to advanced argillic alteration and may host structurally controlled or disseminated, high-sulfidation epithermal precious-metal mineralization, particularly along their margins (e.g., Yanacocha, Peru; Longo et al. 2010).

2.3 Phreatic breccias

Phreatic breccias form in the shallower parts of porphyry copper systems, typically within their lithocaps (Fig. 1) – permeable, lithologically determined rock volumes with fracture-controlled feeder zones – when fluid pressures in deeper reservoirs were transmitted to shallow accumulations of vapor, especially where these contained CO_2. Commonly, the vapor pockets seem to have been confined beneath self-sealed zones of silicification. Intrusions at depth may perturb the shallow hydrologic regime to greater degrees, inducing more energetic vapor separation (flashing) and potentially more deeply penetrating brecciation. Phreatic eruptions can be accompanied by rock fragmentation to depths of at least 1,000 m below the paleosurface (Ohba et al. 2007). The term phreatic in the context of porphyry copper systems is used to signify any aqueous liquid, irrespective of whether it is of meteoric, largely magmatic, or, as commonly the case, mixed origin.

The breccias occupy dike-like to irregular bodies that may either be restricted to the subsurface or attain the paleosurface to form hydrothermal eruption craters

rimmed by breccias and finer-grained ejecta (Hedenquist and Henley 1985; Fig. 1). The clast- to matrix-supported breccias are typically heterolithic, commonly rich in silicified clasts derived from the breached seals, and cemented by chalcedony (Fig. 2c), which can host gold and/or silver mineralization. End-stage cavities may be lined by quartz, barite, and/or other minerals.

3 Breccia timing

Magmatic-hydrothermal breccias are typically related to inter-mineral porphyry phases (Fig. 1) rather than to the first porphyry intrusions to be emplaced (e.g., Sillitoe and Gappe 1984; Bushnell 1988; Anderson et al. 2009; Vry et al. 2010; Perelló et al. 2012). Phreatic breccias are normally also inter-mineral in the context of the enclosing lithocap and normally later than potassic alteration in underlying porphyry copper deposits. Hence, these two breccia types commonly contain clasts of altered, veined, and/or mineralized rocks generated during earlier stages of porphyry copper system development. Clast-confined quartz veinlets in magmatic-hydrothermal breccias and vuggy residual quartz clasts in phreatic breccias are emblematic.

Diatremes, present in ~20–30% of deposits worldwide, are normally also late features, post-dating porphyry copper formation. Consequently, centrally located diatremes can be porphyry copper destructive and are everywhere sub-ore grade or barren; however, as noted above, their shallow, lithocap-hosted parts may be subject to at least the final stages of high-sulfidation epithermal precious-metal mineralization (e.g., Dizon, Philippines, Caspiche, Chile, Tujuh Bukit, Indonesia, and Wafi-Golpu, Papua New Guinea; Sillitoe and Gappe 1984; Sillitoe et al. 2013; Harrison et al. 2018; Rinne et al. 2018). Nonetheless, a minority of diatremes pre-date porphyry intrusion and mineralization (e.g., Tujuh Bukit and Grasberg, Indonesia, and Boyongan, Philippines; MacDonald and Arnold 1994; Braxton et al. 2018; Harrison et al. 2018), although they may not in every case be genetically related given that >3 Myr separate the diatreme and copper-gold mineralization at Tujuh Bukit (Harrison et al. 2018).

4 Implications for copper deposit formation

It is clear that the majority of hydrothermal breccias associated with porphyry copper deposits formed after at least the earliest porphyry intrusions had been emplaced and, in the case of most phreatomagmatic and phreatic breccias, after all but the latest intrusions were already in place, hydrothermally altered, and mineralized. Therefore, any juvenile igneous material in most porphyry copper-associated breccias was likewise later than the early porphyry intrusions. Thus, these inter- and late-mineral breccias could not have acted as conduits for ascent of the magmas that fed the porphyry intrusions most closely related to the early, highest-grade porphyry copper mineralization.

Many porphyry copper deposits were formed beneath or, less commonly, in the basal parts of volcanic edifices, including stratovolcanoes and dome complexes (Sillitoe 1973). However, magmatic-hydrothermal breccias, the most closely related type to porphyry copper deposit formation, cannot have been connected to overlying volcanic features because they terminate subsurface, mainly beneath or in the lower parts of lithocaps (Fig. 1). This conclusion is widely corroborated by the results of core drilling, which further show that the apices of porphyry intrusions, where preserved in shallowly eroded systems, commonly beneath lithocaps, display abrupt contacts with non-brecciated, older (typically much older) host rocks (e.g., Recsk, Hungary, Red Mountain, Arizona, Far Southeast, Philippines, Pampa Escondida and Valeriano, Chile, and Wafi-Golpu; Baksa et al. 1980; Quinlan 1981; Hedenquist et al. 1998; Sillitoe 1999; Hervé et al. 2012; Sillitoe et al. 2016; Rinne et al. 2018; Fig. 1).

Therefore, in the majority of porphyry copper deposits, emplacement of early, ore-related porphyry intrusions was likely facilitated not by breccia bodies but by structural and rheological anisotropies, particularly the dilatant portions of deeply penetrating faults and their associated damage zones (Tosdal and Richards 2001). The only exceptions could be the few deposits that were preceded by and emplaced into diatremes (Grasberg, Tujuh Bukit, and Boyongan; see above), which may have helped guide magma ascent. Nonetheless, even though these early diatremes may have attained the paleosurface in the form of maar volcanoes, an active, through-going connection to the paleosurface was not retained during subsequent porphyry copper formation. Furthermore, when the more numerous late-mineral diatremes formed and vented, porphyry copper deposit formation was declining or had already ended. The small-volume ignimbrite eruptions that concluded porphyry copper formation at Río Blanco-Los Bronces and Bajo de la Alumbrera, Argentina were similarly terminal events (Toro et al. 2012; Buret et al. 2017).

5 Conclusions

Porphyry copper deposits are commonly associated with one or more varieties of hydrothermal breccia, most of which were emplaced during the hydrothermal alteration and mineralization events, including their waning stages. Therefore, most breccias did not act as either conduits for pre-mineral magma ascent or provide pre- or syn-mineral connections to any suprajacent volcanic activity. Nearly all breccias that could potentially have attained the paleosurface are late and post-dated porphyry copper formation, although they may have overlapped with high-sulfidation epithermal precious-metal mineralization hosted by lithocaps. The field evidence further shows that porphyry stocks and dikes were overlain at the time of copper ± molybdenum ± gold mineralization by intact host rocks.

Therefore, intrusions that underwent main-stage porphyry copper development lacked significant through-going connections to the overlying volcanic environment, a situation that may well be a prerequisite for effective ore deposition. A direct volcanic connection, via diatremes,

developed during the waning stages of a minority of porphyry copper systems, and precursor diatremes are also recognized but of extremely minor occurrence.

These conclusions further suggest that porphyry copper deposits are generated during volcanic dormancy, beneath parasitic vents on volcano flanks (e.g., Bajo de la Alumbrera; Proffett 2003), or following final construction of the edifices, with the last two alternatives undoubtedly favoring their preservation.

Acknowledgments

Thanks are due to porphyry copper-related breccias worldwide for revealing some of their secrets and to Jeff Hedenquist and Pepe Perelló for helpful manuscript reviews.

References

Anderson ED, Atkinson WW Jr, Marsh T, Iriondo A (2009) Geology and geochemistry of the Mammoth breccia pipe, Copper Creek mining district, southeastern Arizona: evidence for a magmatic-hydrothermal origin. Miner Deposita 44:151-170

Baksa C, Cseh-Nemeth J, Csillag J, Földessy J, Zelenka T (1980) The Recsk porphyry and skarn deposit, Hungary. SGA Spec Publ 1:73-76

Buret Y, Wotzlaw JF, Roozen S, Guillong, M, von Quadt A, Heinrich CA (2017) Zircon petrochronological evidence for a plutonic-volcanic connection in porphyry copper deposits. Geology 45:623-626

Bushnell SE (1988) Mineralization at Cananea, Sonora, Mexico, and the paragenesis and zoning of breccia pipes in quartzofeldspathic rock. Econ Geol 83:1760-1781

Gustafson LB, Hunt JP (1975) The porphyry copper deposit at El Salvador, Chile. Econ Geol 70:857-912

Harrison RL, Maryono A, Norris, MS, Rohrlach BD, Cooke DR, Thompson, JM, Creaser RA, Thiede DS (2018) Geochronology of the Tumpangpitu porphyry Au-Cu-Mo and high-sulfidation epithermal Au-Ag-Cu deposit: Evidence for pre- and postmineralization diatremes in the Tujuh Bukit district, southeast Java, Indonesia. Econ Geol 113:163-192

Hedenquist JW, Henley RW (1985) Hydrothermal eruptions in the Waiotapu geothermal system, New Zealand: Their origin, associated breccias, and relation to precious metal mineralization. Econ Geol 80:1640-1668

Hedenquist JW, Arribas A, Reynolds TJ (1998) Evolution of an intrusion-centered hydrothermal system: Far Southeast-Lepanto porphyry and epithermal Cu-Au deposits, Philippines. Econ Geol 93:373-404

Hervé M, Sillitoe RH, Wong C, Fernández P, Crignola F, Ipinza M, Urzúa F (2012) Geologic overview of the Escondida porphyry copper district, northern Chile. Soc Econ Geol Spec Publ 16:55-78

Howell FH, Molloy JS (1960) Geology of the Braden orebody, Chile, South America. Econ Geol 55:863-905

Irarrazaval V, Sillitoe RH, Wilson AJ, Toro JC, Robles W, Lyell GD (2010) Discovery history of a giant, high-grade, hypogene porphyry copper-molybdenum deposit at Los Sulfatos, Los Bronces-Río Blanco district, central Chile. Soc Econ Geol Spec Publ 15:253-269

Longo AA, Dilles, JH, Grunder AL, Duncan R (2010) Evolution of calc-alkaline volcanism and hydrothermal gold deposits at Yanacocha, Peru. Econ Geol 105:1191-1241

MacDonald GD, Arnold, LC (1984) Geological and geochemical zoning of the Grasberg Igneous Complex, Irian Jaya, Indonesia. J Geochem Explor 50:143-178

Ohba T, Taniguchi H, Miyamoto T, Hayashi S, Hasenaka T (2007) Mud plumbing system of an isolated phreatic eruption at Akita Yakeyama volcano, northern Honshu, Japan. J Volcanol Geotherm Res 161:35-46

Perelló J, Sillitoe RH, Mpodozis C, Brockway H, Posso H (2012) Geologic setting and evolution of the porphyry copper-molybdenum and copper-gold deposits at Los Pelambres, central Chile. Soc Econ Geol Spec Publ 16:79-104

Proffett JM (2003) Geology of the Bajo de la Alumbrera porphyry copper-gold deposit, Argentina. Econ Geol 98:1535-1574

Quinlan J (1981) Geology and silicate-sulfide alteration zoning at the Red Mountain porphyry copper deposit, Santa Cruz County, Arizona: In: Symposium on relations of tectonics to ore deposits in the southern Cordillera, Tucson, 1981, Arizona Geol Soc–Univ Arizona mine tour and field trip 8, Guidebook, pp 4-25

Rinne ML, Cooke DR, Harris AC, Finn DJ, Allen CM, Heizler MT, Creaser RA (2018) Geology and geochronology of the Golpu porphyry and Wafi epithermal deposit, Morobe province, Papua New Guinea. Econ Geol 113:271-294

Rivera SL, Alcota H, Proffett J, Díaz J, Leiva G, Vergara M (2012) Update of the geologic setting and porphyry Cu-Mo deposits of the Chuquicamata district, northern Chile. Soc Econ Geol Spec Publ 16:19-54

Sillitoe RH (1973) The tops and bottoms of porphyry copper deposits. Econ Geol 68:799-815

Sillitoe RH (1985) Ore-related breccias in volcanoplutonic arcs. Econ Geol 80:1467-1514

Sillitoe RH (1999) Styles of high-sulphidation gold, silver and copper mineralisation in porphyry and epithermal environments. Australas Inst Min Metall Pacrim '99 Conf, Bali, Indonesia, Proc, pp 527-532

Sillitoe RH, Angeles CA Jr (1985) Geological characteristics and evolution of a gold-rich porphyry copper deposit at Guinaoang, Luzon, Philippines. In: Asian Mining '85, Inst Min Metall, London, pp 15-26

Sillitoe RH, Gappe IM Jr (1984) Philippine porphyry copper deposits: Geologic setting and characteristics. United Nations ESCAP, CCOP Tech Publ 14, 89 pp

Sillitoe RH, Tolman J, Van Kerkvoort G (2013) Geology of the Caspiche porphyry gold-copper deposit, Maricunga belt, northern Chile. Econ Geol 108:585-604

Sillitoe RH, Burgoa C, Hopper DR (2016) Porphyry copper discovery beneath the Valeriano lithocap, Chile. Soc Econ Geol Newsl 106:1, 15-20

Toro JC, Ortúzar J, Zamorano J, Cuadra P, Hermosilla J, Spröhnle C (2012) Protracted magmatic-hydrothermal history of the Río Blanco-Los Bronces district, central Chile: Development of the world's greatest known concentration of copper: Soc Econ Geol Spec Publ 16:105-126

Tosdal RM, Richards JP (2001) Magmatic and structural controls on the development of porphyry Cu ± Mo ± Au deposits. Rev Econ Geol 14:157-181

Vry VH, Wilkinson JJ, Seguel J, Millán J (2010) Multistage intrusion, brecciation, and veining at El Teniente, Chile: Evolution of a nested porphyry system. Econ Geol 105:119-153

The hypogene evolution of the Spence porphyry copper system, northern Chile

Edward G. Bunker
University of Bristol, UK

Simon R. Tapster
NERC Isotope Geosciences Laboratory, British Geological Survey, UK

Frances J. Cooper, Jon D. Blundy
University of Bristol, UK

Abstract. The timing and duration of magmatism and ore formation in Porphyry Copper Deposit (PCD) systems offer valuable insight in to the geological processes leading to ore formation which may aid in future exploration efforts and can provide constraints upon the potential metal endowment of a deposit. The Spence PCD in Northern Chile is centered upon granodioritic porphyry stocks of Palaeocene age. Whilst Spence formed at ~57 Ma, spatio-temporal constraints on the evolution of magmatism are poorly defined and the deposit's geological model lacks the detail required for to investigate the evolution of the deposit at high resolution. We redefine the sequence of igneous units at the deposit based on key textural characteristics, these lithologies are then mapped using a novel and non-intrusive mapping strategy which utilises drill-core. We apply high precision CA-ID-TIMS U-Pb geochronology to the deposit using the lithologies defined in this study to reveal a complex magmatic history with at least four independent pulses of mineralising hydrothermal fluid. Our data illustrate that magmatism and hydrothermal activity initiated in the SSW of the deposit and gradually migrated NNE following the trend of the pre-existing Antofagasta-Calama Lineament.

1 Introduction

Ore deposit models underpin our understanding of the geological processes leading to ore formation and provide a theoretical basis which may be used in minerals systems exploration strategies and to generate exploration criteria which may be applied in the field. More locally, ore deposit models are used in day-to-day decision making at mines which influence pit design, ore processing and efficiency gains.

Spence was discovered in Region II of northern Chile in 1995-96 during an exploration drilling campaign by Rio Algom Ltd. (Sillitoe 2000). The deposit was a blind discovery beneath Miocene age gravels of the Atacama Formation (Guzman-Cruces 2001) which limited the level of detail that could be incorporated in the deposit's geological model to what could be observed in drill-core and through remote sensing at that early stage.

We conduct a detailed study of the intrusive sequence at the Spence PCD through textural study, geological mapping and high precision CA-ID-TIMS U-Pb zircon geochronology leading us to propose a revised geological model for the hypogene evolution of the deposit based upon observable textural criteria and cross-cutting relationships.

We reveal the absolute time-frame of this complex geological system demonstrating that each zone of the deposit developed independently from one another and that magmatism was more protracted toward the south. Several mineralising hydrothermal events are identified that occurred diachronously across the deposit. Magmatic and hydrothermal activity are shown to migrate from the SSW to NNE across the deposit following pre-existing crustal structures.

2 Geological setting

The Spence PCD is located in the Paleocene-early Eocene metallogenic belt of northern Chile (Sillitoe and Perelló 2005). The deposit consists of three mineralised igneous centers and a zone of sub-economic dykes which are termed the South, Central South, Central North and North Zones and which are aligned along an NNE trending axis.

Rowland (2001) determined that Spence was comprised of three intrusive phases which are differentiated by cross-cutting relationships and timing relative to mineralisation. These are a syn-mineralisation granodiorite termed Quartz Feldspar Porphyry 1 (QFP1), a post mineralisation granodiorite termed Quartz Feldspar Porphyry 2 (QFP2) and a monzodiorite dyke termed Feldspar Porphyry (FP) which represented the latest igneous event. Preliminary studies constrained the emplacement age of Spence by ^{40}Ar-^{39}Ar biotite geochronology to 57.00 ± 0.69 Ma (Rowland & Clark, 2001).

3 Redefining the igneous sequence at Spence based upon igneous texture

The igneous stratigraphy of Spence was set out by Rowland (2001) who argued that the deposit was comprised of three igneous units QFP1, QFP2 and FP. Whilst subsequent work has acknowledged that the geology of Spence is more complex than this simplified geological model suggests (Sillitoe 2011) Rowland's

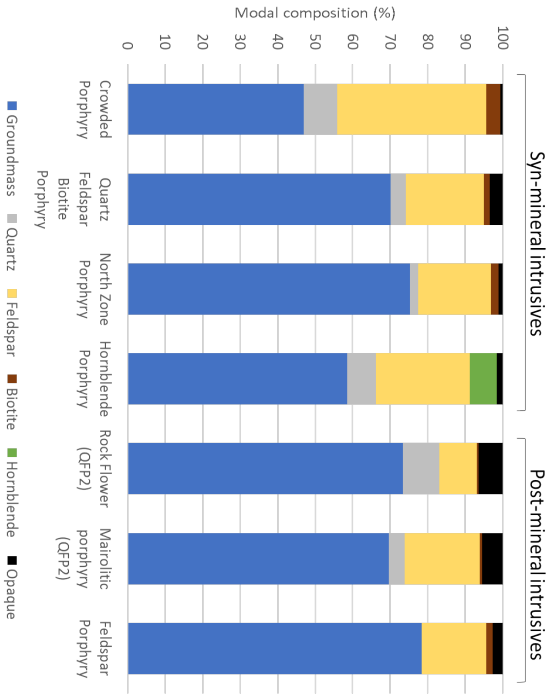

Figure 1. Representative modal compositions for the igneous lithologies recognized at Spence in this study, determined by point counting. The results indicate a gradual decrease in crystallinity of the syn-mineral intrusives with relative age, apart from the hornblende porphyry. Post mineral intrusives generally have elevated pyrite contents which is reflected in the modal opaque composition.

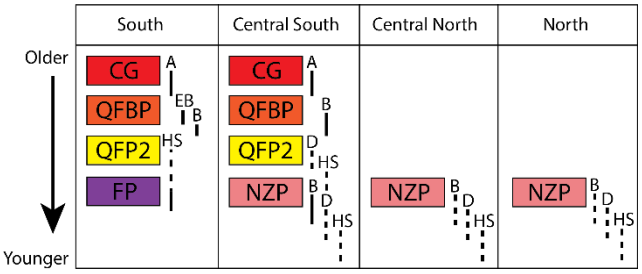

Figure 2. Relative chronology of igneous units and hydrothermal veins in the four zones of the Spence PCD. Veins are classified after the terminology of Gustavson and Hunt (1975): A – A-vein, EB – Early B vein, B – B-vein, D – D-vein, HS – High Sulphidation vein. Lithological abbreviations are as follows: CG – Crowded Granodiorite, QFBP – Quartz Feldspar Biotite Porphyry, QFP2 – Mairolitic porphyry and rock flour, FP – Feldspar Porphyry, HP – Hornblende Porphyry, NZP North Zone Porphyry.

model is still employed in geological studies to date (e.g. Cameron et al. 2004; Palacios et al. 2007).

In order to study the hypogene evolution of Spence using sensitive analytical methods, a detailed understanding of the igneous stratigraphy and relative chronology of the deposit is first required. We grouped samples by their igneous texture, using phenocryst size range, phenocryst to groundmass ratio and modal mineralogy in order to redefine the igneous stratigraphy of the deposit (Fig. 1).

We established a relative chronology of igneous and hydrothermal events through observation of geologic contacts in drill-core and hand-sample scale cross-cutting relationships (Fig. 2). There were no clear relative relationships between igneous units within different zones of the deposit, therefore the relative progression of events occurring in different zones of the deposit could not be determined in the field.

4 Developing a geological map through interpolated drill-core study

4.1 Mapping rationale and methods

Whilst the geological model proposed by Rowland (2001) facilitates the day-to-day operation of the mine, it does not reflect the spatial and textural complexity of the deposit's igneous lithologies as determined in this study. In order to better illustrate the geology of the deposit, and to investigate its geological and spatial complexity in greater detail, the deposit required re-mapping.

At the time of discovery, Spence was concealed beneath 15-120 m of Miocene gravels, subsequent access to surface exposure of the geology of Spence has been limited due to logistical and safety considerations relating to mining operations ongoing at the site. To overcome this, we utilized the extensive library of drill-core which covers the deposit at a high spatial resolution in order to interpolate the geology of the deposit at a depth of our choosing.

We studied 10 m intercepts from 252 drill-cores that were distributed across the deposit. The igneous lithologies were logged according to the textural criteria defined in section 3; geological contacts were recorded as well as the location of tectonic breccias which were interpreted as faults. An irregular drill-core spacing was used with high sample density in geologically complex areas, and less densely spaced in simpler regions.

4.2 Observations

The Jurassic age Cerritos Bayos Formation was differentiated into a calcareous and silicic member based principally upon its colour; the contact between these sub-units defined the axis of a north plunging anticline that had not been previously recognized. The fold axis parallels the axis of the deposit and constrains the intrusive zones of the deposit in the South and Central South Zones (Fig 3). The deposit is further bounded by faults trending SSW-NNE, NW-SE and N-S.

The crowded granodiorite (CG) occurs in the South and Central South zones where it is cut by the quartz feldspar biotite porphyry (QFBP), the contact between these two units is often faulted, but where it is observed the contact is diffuse over several meters. In the South and Central South zones, QFBP is cut by the the post-mineralisation mairolitic porphyry which grades from a competent porphyry unit to a breccia with igneous matrix or a rock flour with occasional igneous clasts. The magmatic breccia is most extensive in the South Zone and is overprinted by a later phase of hydrothermal breccia which is cemented by a fine-grained sericite, tourmaline and molybdenite matrix. Feldspar Porphyry

(FP) cuts the hydrothermal breccia in the South Zone as an NNE trending dyke that represents the youngest intrusive event in this zone of the deposit.

The North Zone Porphyry (NZP) is observed in the Central South, where it cuts the post-mineralisation mairolitic porphyry and rock flour, however despite cutting these units, the NZP exhibits B-vein and disseminated mineralisation. The NZP represents the only lithology identified in the Central North and North Zones.

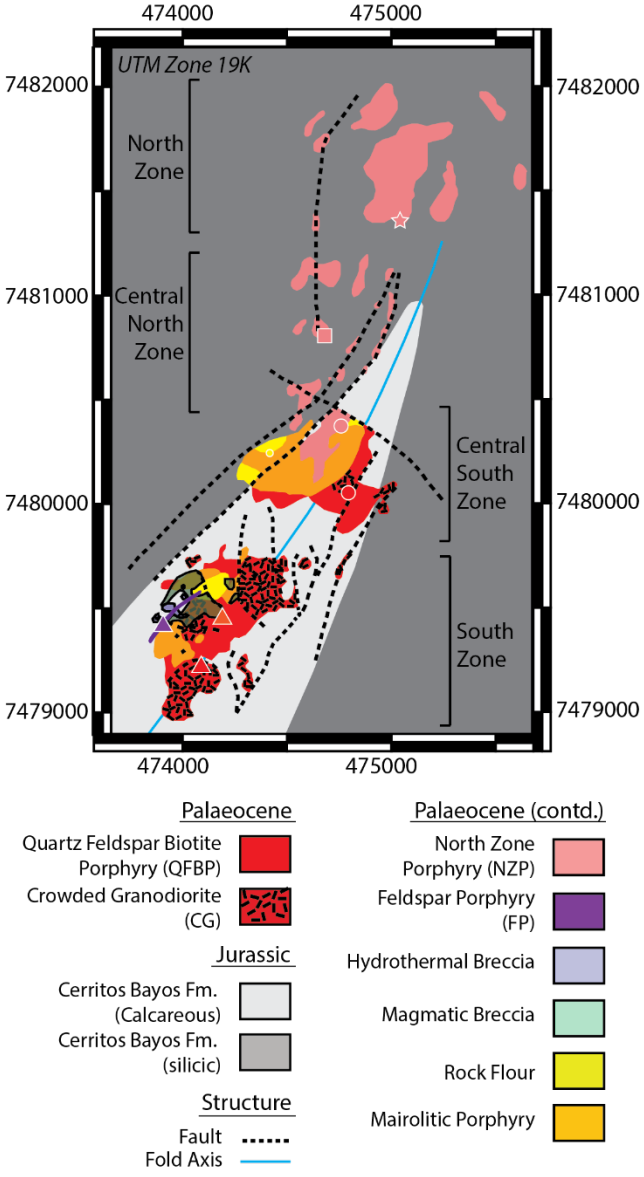

Figure 3. A sub-surface geological map of the Spence PCD at 1400m above sea level (~350 m below surface) which was obtained through the study of >250 10 m intervals of drill-core intersecting the same datum. Sample locations for U-Pb CA-ID-TIMS dating are indicated on the map as colour-coded shapes.

5 CA-ID-TIMS U-Pb zircon geochronology

In order to place absolute constraints upon the newly defined igneous stratigraphy and relative chronology, we applied high-precision Chemical Abrasion Isotopic Dilution Thermal Ionisation Mass Spectrometry (CA-ID-TIMS) U-Pb zircon geochronology to a representative suite of samples from Spence (Fig. 4). The samples were distributed across the deposit and were selected to cover the full igneous history of the deposit as determined through relative chronology; the sample locations are shown in Figure 3.

Deposit formation commenced in the South Zone when the crowded granodiorite intruded at 57.286 ± 0.025 Ma. Magmatism subsequently migrated gradually toward the north through time, with the final pulse occurring in the North Zone at 56.616 ± 0.032 Ma, indicating that magmatism was ongoing for at least 670 ± 41 kyr. The duration of magmatism varies between zones, with the South Zone displaying the longest interval of magmatism of 412 ± 78 kyr, the Central South Zone indicating a duration of 224 ± 39 kyr and single pulse durations constrained in the Central North and North Zones.

6 Discussion

6.1 The magmatic and hydrothermal evolution of the Spence PCD

We present a new igneous stratigraphy for Spence which is differentiated texturally, spatially and temporally. Our stratigraphy defines a complex progression of igneous events with each zone having a unique igneous history. The syn-mineralisation intrusive suite is separated in to at least four distinct pulses which have distinct vein associations, the relative progression of vein types determined from cross-cutting relationships in hand sample indicate that there were at least four distinct pulses of magmatic hydrothermal fluid. Within the main phase of mineralisation the age of syn-mineral intrusives is roughly proportional to the phenocryst/groundmass ratio of the sample.

Magmatism onset in each zone of the deposit defines a steady migration from SSW to NNE following the 4 km long axis of the deposit. The SSW-NNE structural fabric of the deposit is reflected in the orientation of early faults and the axis of the pre-emplacement fold along which the deposit is emplaced.

We identify texturally similar units that were emplaced diachronously across different zones of the deposit, illustrating a shortfall in the correlation of rocks by texture alone. The potential for texturally similar but temporally distinct intrusive events to occur within a short period of time in the same magma system is not well understood, but this may become an increasingly common phenomenon as the available precision of dating techniques improves.

6.2 Structural evolution of the Spence PCD

Prior to the emplacement of Spence, the Jurassic age Cerritos Bayos Fm. was folded in to a N-plunging anticline, that may have influenced the

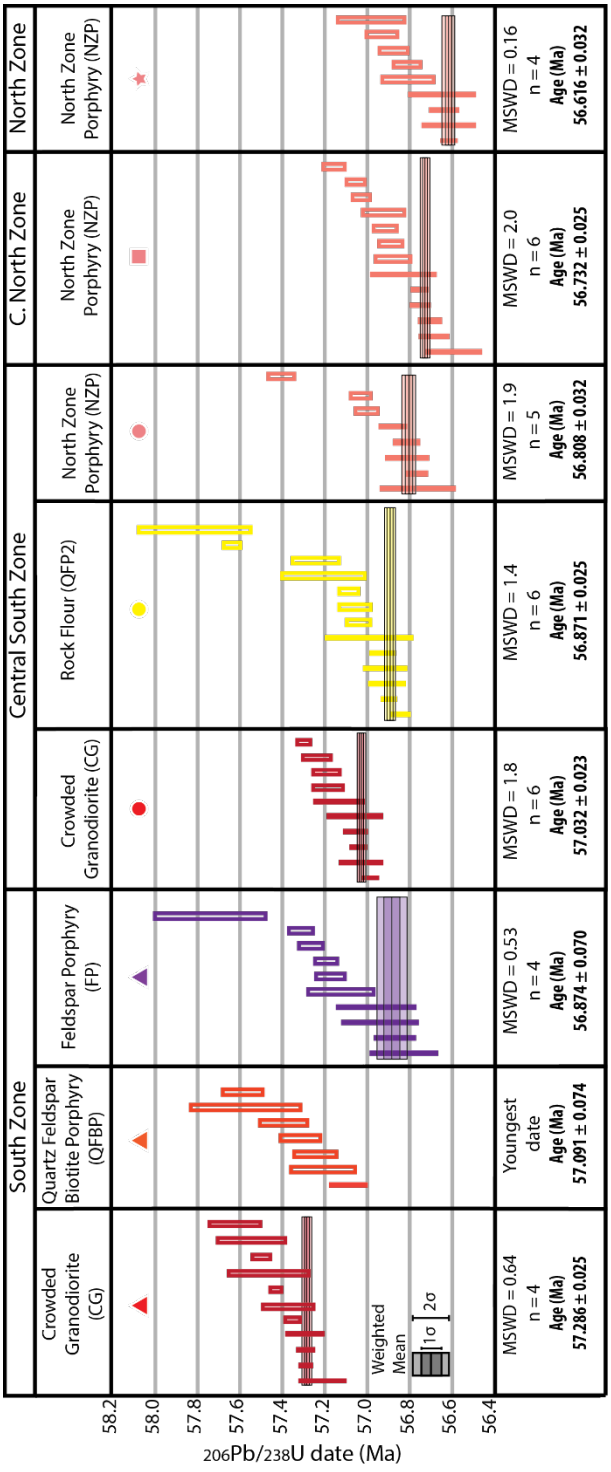

Figure 4. High precision Chemical Abrasion Isotopic Dilution Thermal Ionisation Mass Spectrometry (CA-ID-TIMS) U-Pb zircon dates obtained across the Spence deposit in northern Chile. Each coloured bar is a single zircon date, the filled bars indicate dates included in the weighted mean age, whereas un-filled bars are excluded from the weighted mean. The weighted mean was determined from the youngest acceptable population of zircon were determined using a Mean Squared Weighted Deviate (MSWD) or reduced chi-squared statistic. A weighted mean was not calculated for QFBP because the data are over-dispersed and do not fit an acceptable population. All data are presented at 2σ confidence. Sample locations are indicated by coloured shapes and correspond to those seen in Figure 3

location and orientation of the deposit. NNE-trending faults bound the South and Central South Zones of the deposit; elongate porphyry dykes coincide with these faults indicating that they were active at the time of deposit emplacement. These faults are aligned with a major trans-crustal fracture that runs through the region termed the Antofagasta-Calama Lineament which may have influenced the location of PCD formation during the Palaeocene (Arriagada et al. 2003; Cameron et al. 2004; Palacios et al. 2007).

7 Implications

A revised geological model for the hypogene evolution of the Spence PCD is presented that indicates that each zone of the deposit has a unique formational history which is independent from respective zones of the deposit. Magmatism began at Spence 57.286 ± 0.025 Ma and lasted for at least 670 ± 41 kyr however over this time the magmatic activity migrated gradually NNE, influenced by the regional structural fabric of the Antofagasta-Calama Lineament.

Acknowledgements

This work was funded by BHP. We are grateful to Jean des Rivières for permitting this work and for offering guidance alongside Cam McCuaig, Aldo Vasquez, Jaime Cortes and Jill Terry. We thank Reinaldo Guzmán and his team at Spence who gave us great geological insight and access to the drill-core used in this study. We are grateful to Lia Ituarte for providing logistical and communicative support throughout the project.

References

Arriagada, C. et al. 2003. Paleogene clockwise tectonic rotations in the forearc of central Andes, Antofagasta region, northern Chile. Journal of Geophysical Research

Cameron, E.M. et al. 2004. Finding deeply buried deposits using geochemistry. Geochemistry: Exploration, Environment, Analysis 4:7–32.

Gustavson, L.B. and Hunt, J.P. 1975. The porphyry copper deposit at El Salvador, Chile. Economic Geology 70(5):857–912.

Guzman-Cruces, R.A. 2001. Geologia del proyecto Spence y caracterizacion de la capa lixiviada. Universidad De Chile.

Palacios, C. et al. 2007. The role of the Antofagasta-Calama Lineament in ore deposit deformation in the Andes of northern Chile. Mineralium Deposita 42(3):301–308

Rowland, M.G. 2001. Geology of the Spence porphyry copper deposit, Northern Chile.

Sillitoe, R.H. 2000. Exploration and discovery of base and precious metal deposits in the circum-Pacific region - A late 1990s update. Tokyo.

Sillitoe, R.H. 2011. Comments on the Cerro Colorado and Spence hypogene models, northern Chile.

Sillitoe, R.H. and Perelló, J. 2005. Andean Copper Province: Tectonomagmatic Settings, Deposit Types, Metallogeny, Exploration, and Discovery. In: Society of Economic Geologists 100th Anniversary Volume:845–890.

Ore genesis of the Devonian superimposed Yulekenhalasu porphyry Cu-Mo deposit in CAOB: Insights from paragenesis and fluid inclusions

Chao Wu, Huayong Chen
Key Laboratory of Mineralogy and Metallogeny, Guangzhou Institute of Geochemistry, Chinese Academy of Sciences, China

Abstract. The Yulekenhalasu porphyry Cu–Mo deposit is located in the Devonian Halasu copper belt, part of the East Junggar block in northwest China. At Yulekenhalasu, Cu and Mo mineralization commonly occurs as disseminations or veinlets in both porphyry-type alteration zones and late high-grade Cu sulfide-bearing veins. Seven hydrothermal alteration stages were identified at the deposit, including sodic-calcic alteration (Stage I), potassic alteration (Stage II), propylitic alteration (Stage III), phyllic alteration (Stage IV), late Cu sulfide-bearing veins (Stage V), argillic alteration (Stage VI), and supergene alteration (Stage VII). Fluid inclusion assemblage (FIA) microthermometry coupled with cathodoluminescence (CL) imaging reveals that mineralizing fluid for Stage II–IV had intermediate to high temperatures and variable salinities. The Stage V late Cu sulfide-bearing veins were associated with intermediate temperatures and dilute hydrothermal fluid, in contrast to low-temperature and dilute fluid in Stage VI. Stage II and III veins were overprinted by hydrothermal fluid associated with Stage V and VI via reopening of early hydrothermal veins. Discrete multi-stage alteration features in Yulekenhalasu can represent a typical example of the Paleozoic porphyry copper deposit (PCD) systems formed in the Central Asian Orogenic Belt (CAOB).

1 Introduction

The CAOB, one of the world's largest subduction-accretionary orogens (Carroll et al. 1990; Sengör et al. 1993; Mossakovsky et al. 1994), hosts several giant PCDs including Oyu Tolgoi, Samarka and Aktogai-Aiderly, consequently it is considered one of most crucial porphyry Cu belts in the world (Perelló et al. 2001; Yakubchuk 2004; Mao et al. 2014; Seltmann et al. 2014). Corresponding to recognized magmatic-hydrothermal-tectonic overprinting events (Zhang et al. 2015; Xue et al. 2016), many PCDs in the CAOB initially formed in an island arc setting underwent the Late Paleozoic collision and subsequent post-collision and intra-plate extension, and raise critical challenges and opportunities for mineral exploration (Yakubchuk 2004). The Yulekenhalasu deposit, one of the earliest discovered PCDs in the Chinese Altay – East Junggar (CAEJ) orogenic belt, is characterized by typical porphyry-type mineralization overprinted by late-stage hydrothermal events. Previous studies suggest that Upper Devonian porphyry mineralization was probably formed by island arc-related flat subduction, followed by Late Carboniferous intra-plate tectonic overprinting (Wu et al. 2015; Xue et al. 2016). However, the detailed processes involved in the evolution of the hydrothermal fluid in various tectonic settings, including from the subduction to post-subduction stages, and their contributions to the metal endowment are still inadequately understood.

FIA represents the finest temporal resolution as to the timing of initial closure of the inclusion vacuoles (Goldstein and Reynolds 1994), while CL microscopy can distinguish compositional variations in quartz crystals resulted from the growth, fracturing-healing, and re-crystallization (Rusk and Reed 2002). Rather than lumping together of multiple events, methods such as FIA and CL allow us to consider each growth zone and each event of fracture healing as separate events in geological history at Yulekenhalasu deposit.

Aiming to address the current lack of understanding the detailed paragenetic history of this vital deposit in NW China, this study presents microthermometric data, including new FIA coupled with CL imaging on hydrothermal quartz sampled from different alteration zones at the Yulekenhalasu deposit, the combination of which contributes not only to a better understanding of the complex hydrothermal evolution of the Yulekenhalasu deposit, but also to the more generalized metallogenic model for similar multi-stage mineralization in the CAOB porphyry Cu deposits.

2 Deposit geology

The area surrounding the Yulekenhalasu deposit is host to remnants of a succession of marine volcanic or volcaniclastic rocks, dominated by the Middle Devonian Beitashan Formation that contains mafic to intermediate lavas and corresponding tuffs, breccias and sandstones, and the Early Carboniferous Jiangbasitao Formation that consists primarily of carbonaceous black shale, slate, conglomerate, tuffaceous sandstone and intermediate tuff intercalated with minor andesite (Zhang et al. 2009). Of the three principal fault orientations recognized in the district (Fig. 1), including NNW-, NE- and WE-trending fault systems, the NNW-trending fault system has a similar strike direction to the principal ore bodies at Yulekenhalasu, and appear closely associated with the regional Fuyun fault which dips sharply to the northeast.

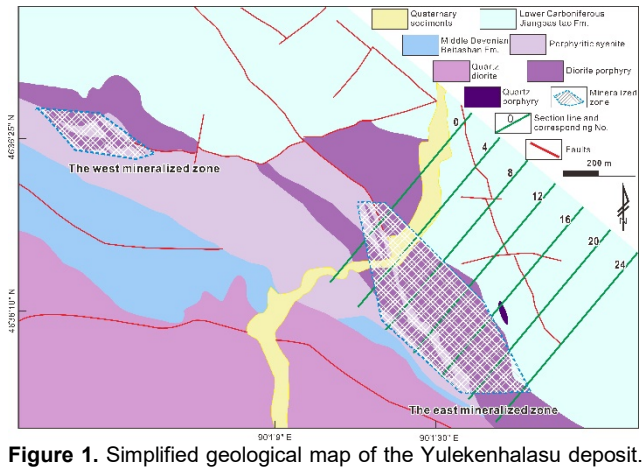

Figure 1. Simplified geological map of the Yulekenhalasu deposit. Modified from the No. 4 Geological Party of the Xinjiang Bureau of Geology and Mineral Exploration and Development, 2009.

Intrusive rocks of Middle Devonian to Carboniferous age comprise the pre-mineralization (porphyritic syenite, ca. 390 Ma), syn-mineralization (quartz diorite and diorite porphyry, ca. 382–372 Ma) and post-mineralization (quartz porphyry and alkali granite porphyry, ca. 350–320 Ma) episodes of intrusive activity in the district. The emplacement of these porphyries are generally controlled by the NW-trending fault system, and are cross-cut by WE-trending faults (Fig. 1). The porphyritic syenite (ca. 391 Ma) occurs as NW-trending stocks and contains coarse-grained K-feldspar phenocrysts within a groundmass of fine-grained quartz and K-feldspar. The quartz diorite (ca. 379 Ma), which crops out as a large stock along the south margin of the district, locally intruded the Beitashan Formation (Fig. 1) and comprises plagioclase, quartz, and biotite, with minor alkali feldspar, titanite, apatite, magnetite, and zircon. The diorite porphyry (ca. 377 Ma) is separated from the overlying Jiangbasitao Formation by an NW-trending fault (Fig. 1) and generally contains a weak to moderately porphyritic texture, consisting of plagioclase, quartz, K-feldspar, minor biotite and hornblende. Post-mineralization quartz porphyry is exposed as dykes in the Jiangbasitao Formation and is characterized by a porphyritic texture with quartz and minor plagioclase as phenocrysts, and a groundmass of quartz, plagioclase, and biotite (Yang et al. 2014). The alkali granite porphyry (ca. 327 Ma) is dominated by coarse-grained K-feldspar and minor biotite phenocrysts within a groundmass of fine-grained K-feldspar, quartz, and biotite (Wu et al. 2015).

Two mineralized zones (west and east) have been recognized in the Yulekenhalasu ore district (Fig. 1). The eastern zone occurs within the diorite porphyry and is host to the main copper reserve; it extends for approximately 800 m in length and 20 m to 120 m in width (Fig. 1). The western zone occurring in basalt and porphyritic syenite is distributed in the NW part of the ore district, and extends for about 300 m in length, with a width of 10–80 m, consisting of three smaller scale copper mineralized bodies. Sulfide minerals at the Yulekenhalasu deposit consist primarily of chalcopyrite, pyrite, and molybdenite, with lesser amounts of bornite, galena, sphalerite, and pyrrhotite. Gangue minerals are dominated by quartz, feldspar, magnetite, biotite, gypsum, sericite, chlorite, epidote and calcite. Ores occur in various textural forms including disseminated grains, veinlets, stockwork veins, metasomatic relict grains, and cataclastic textures, as described in more detail below.

3 Superimposition and evolution of hydrothermal fluids at the Yulekenhalasu deposit

Seven hydrothermal alteration stages were identified at the Yulekenhalasu deposit, including Stage I sodic-calcic alteration, Stage II potassic alteration, Stage III propylitic alteration, Stage IV phyllic alteration, Stage V late Cu sulfide-bearing veins, Stage VI argillic alteration, and Stage VII supergene alteration. Of the above alteration stages, the potassic and late Cu sulfide-bearing veins were the principle ore-forming stages. The paragenetic study of the Yulekenhalasu deposit indicates that potassic alteration was superimposed by later phyllic alteration and further overprinted by Stage V late Cu sulfide-bearing veins and Stage VI argillic assemblages. Similar overprinting textures of magmatic-hydrothermal features have been widely recognized in deposits containing multiple mineralizing events, including the Bingham Canyon porphyry Cu–Mo–Au, Questa porphyry Mo, Acupan porphyry-epithermal Au–Ag, and Dabaoshan porphyry Mo deposits. Cooke and Bloom (1990) suggested that intermittent rupture events could produce late hydrothermal veins encrusting or crosscutting early veins before sealing, eventually leading to repeated seal/rupture cycles, wherein late fractures and reopened veins also act as pathways for late-stage fluid circulation, resulting in complex overlapping of fluids from different stages (Cooke and Bloom 1990).

The combination of microthermometric data and CL imaging in this study supports the premise of there being multi-stage hydrothermal superimposition events onto pre-existing mineral assemblages at the Yulekenhalasu deposit. For example, firstly, the presence of CL-bright quartz cores with CL-dark overgrowths in Stage II quartz veins implies the superimposition of Stage IV phyllic alteration onto early-formed Stage II potassic alteration. Subsequently, in Stage II veins, the presence of cobweb-like networks of CL-dark quartz (Stage V) cutting CL-bright quartz grains of Stage II, indicates overprint of Stage V hydrothermal fluid on the precursor Stage II quartz. Finally, continuous stringers of CL-dark quartz that hosts low-temperature FIs are observed to cut across cobweb-like CL-dark quartz containing Generation II FIs, combined with above observations, thus suggesting that the early homogeneous quartz veins forming in Stage II were initially overprinted by phyllic alteration (Stage IV), subsequently reopened in response to Stage V CO_2-bearing fluid represented by cobweb-like CL-dark quartz, and eventually modified by injection of a Stage VI fluid, producing new CL-dark quartz of continuous stringers in Stage II veins.

Based on textural studies of multi-generation quartz veins in porphyry Cu systems (e.g., Grasberg, Butte,

Bingham Canyon, and Oyu Tolgoi), later quartz veins are generally CL-dark and characterized by low Ti concentrations, most likely due to their formation at lower temperatures and high Al due to more acidic fluids(Rusk et al. 2008). These features are consistent with studies at Yulekenhalasu, as Stage IV, V and VI quartz vein-related FIAs are characterized by relatively lower temperatures (appropriately 230 °C for Stage IV, 300 °C for Stage V and 160 °C for Stage VI) compared with CL-bright quartz vein-related FIAs with temperatures at ~ 400 °C for stage II. Also, the lower temperature and more acidic nature of the overprinting Stage VI hydrothermal fluid are further supported by its association with muscovite-bearing and argillic alteration-dominated mineral assemblages at the Yulekenhalasu deposit.

In the porphyry-type alteration stage, the fluid associated with Stage II potassic alteration is characterized by higher temperatures and salinities than for Stage III propylitic alteration, which is most likely due to the distance from the heat source. The occurrence of Type C fluid inclusions suggests that the salinity for potassic alteration could reach up to 30 wt.% NaCl equiv., although the measured data mostly have lower salinities. Also, the recognition of boiling at about 400 °C in the potassic stage implies the lowest trapping depth of ~0.55 km under lithostatic pressure and ~2.3 km under hydrostatic pressure. Therefore, it is inferred that hydrothermal fluid originated from magma may ascend along preexisting fractures, syn-mineralization faults or permeable contacts provided by pre-existing intrusions, and then reach the boundary between lithostatic and hydrostatic pressure at ca. 400 °C, wherein pressure fluctuation was likely to produce fluid boiling and homogeneous quartz. The hydrothermal fluid may have mixed with meteoric water to yield lower salinity Stage IV phyllic alteration. The hydrothermal fluid for Stage V is markedly CO_2-rich and characterized by low salinity, and temperatures of around 300 °C, while Stage VI argillic-related fluid is characterized by temperatures of approximately 160 °C with a wide range of salinity. Although late Cu sulfide-bearing veins of Stage V overprinted on potassic assemblages thus are termed to postdate Stage II, the relative timing between Stage IV and Stage V remained undecided, with no unambiguous evidence uncovered.

Acknowledgements

We sincerely thank Zhenjiang Liu form No. 4 Brigade of the Xinjiang Geology, Mineral Exploration and Development Bureau for the field support in the Halasu PCD belt. This research is financially supported by Type-B Chinese academy of sciences strategic pilot science and technology special (XDB18030206)

References

Carroll A R, Liang Y H, Graham S A, et al. (1990) Junggar basin, northwest China: trapped Late Paleozoic ocean. Tectonophysics 181:1–14.

Cooke D R, Bloom M S (1990) Epithermal and subjacent porphyry mineralization, Acupan, Baguio district, Philippines: a fluid-inclusion and paragenetic study. Journal of Geochemical Exploration 35:297–340.

Goldstein R H, Reynolds T J (1994) Systematics of fluid inclusions in diagenetic minerals: SEPM Short Course 31. Society for Sedimentary Geology 199.

Mao J W, Pirajno F, Lehmann B, et al. (2014) Distribution of porphyry deposits in the Eurasian continent and their corresponding tectonic settings. Journal of Asian Earth Sciences 79:576–584.

Mossakovsky A A, Ruzhentsev S V, Samygin S G, et al. (1994) Central Asian fold belt: geodynamic evolution and formation history. Geotectonics 27:445–474.

Perelló J, Cox D, Garamjav D, et al. (2001) Oyu Tolgoi, Mongolia: Siluro-Devonian porphyry Cu-Au-(Mo) and high-sulfidation Cu mineralization with a Cretaceous chalcocite blanket. Economic Geology 96:1407–1428.

Rusk B, Reed M (2002) Scanning electron microscope-cathodoluminescence analysis of quartz reveals complex growth histories in veins from the Butte porphyry copper deposit, Montana. Geology 30:727–730. doi: Doi 10.1130/0091-7613(2002)030<0727:Semcao>2.0.Co;2.

Rusk B G, Lowers H A, Reed M H (2008) Trace elements in hydrothermal quartz: Relationships to cathodoluminescent textures and insights into vein formation. Geology 36: 547–550.

Seltmann R, Porter T M, Pirajno F (2014) Geodynamics and metallogeny of the central Eurasian porphyry and related epithermal mineral systems: a review. Journal of Asian Earth Sciences 79:810–841.

Sengör A M C, Natal'In B A, Burtman V S (1993) Evolution of the Altaid tectonic collage and Palaeozoic crustal growth in Eurasia. Nature 364:299–307.

Wu C, Chen H Y, Hollings P, et al. (2015) Magmatic sequences in the Halasu Cu Belt, NW China: Trigger for the Paleozoic porphyry Cu mineralization in the Chinese Altay-East Junggar. Ore Geology Reviews 71:373–404. doi: 10.1016/j.oregeorev.2015.06.017.

Xue C J, Chi G X, Zhao X B, et al. (2016) Multiple and prolonged porphyry Cu-Au mineralization and alteration events in the Halasu deposit, Chinese Altai, Xinjiang, northwestern China. Geoscience Frontiers 7: 799–809.

Yakubchuk A (2004) Architecture and mineral deposit settings of the Altaid orogenic collage: a revised model. Journal of Asian Earth Sciences 23:761–779.

Yang F Q, Chai F M, Zhang Z X, et al. (2014) Zircon U–Pb geochronology, geochemistry, and Sr–Nd–Hf isotopes of granitoids in the Yulekenhalasu copper ore district, northern Junggar, China: petrogenesis and tectonic implications. Lithos 190:85–103.

Zhang L C, Xiang P, Xu X W, et al. (2015) Study on superimposed and tectonically reworked porphyry copper deposits in Kalaxianger metallogenic belt, eastern Junggar. Acta Petrologica Sinica 31:333–350.

Zhang Z C, Zhou G, Kusky T M, et al. (2009) Late Paleozoic volcanic record of the Eastern Junggar terrane, Xinjiang, Northwestern China: major and trace element characteristics, Sr–Nd isotopic systematics and implications for tectonic evolution. Gondwana Research 16:201–215.

Relative timing of sulfide precipitation at the Batu Hijau porphyry Cu-Au deposit, Sumbawa, Indonesia

Michael Schirra, Thomas Driesner, and Christoph A. Heinrich
Institute of Geochemistry and Petrology, ETH Zürich, Switzerland

Abstract. Timing of sulfide precipitation in porphyry Cu deposits has been assumed to correlate with quartz vein formation and K-silicate alteration at high temperatures. Cathodoluminescene imaging challenged this traditional model by revealing the textural link between sulfides and a dull-luminescent quartz generation post-dating the main stockwork vein quartz. At Batu Hijau, inconspicuous sulfide veinlets ("paint-veins") associated with pervasive chlorite-sericite alteration are genetically related with dull-luminescent quartz and introduce all Cu-Fe sulfides into the system after a period of quartz dissolution. Fluid inclusions characterize the mineralizing fluid as a magmatic low-salinity liquid-like phase at temperatures of 350° to 300°C. Consequently, quartz vein formation is decoupled from the precipitation of bornite and chalcopyrite, which occurs in an overprinting event at lower temperatures at Batu Hijau, a prototypic porphyry Cu deposit. This finding adds to the growing evidence that sulfide precipitation occurring at low- to moderate temperatures is a common process in porphyry copper formation.

1 Geological framework of the Batu Hijau porphyry Cu-Au deposit

The world-class porphyry Cu-Au deposit Batu Hijau is located in the SW corner of Sumbawa, an island in the tectonically active Sunda-Banda intra-oceanic arc system, Indonesia. Mineralization is centered on a porphyryitic tonalite complex that intruded into a thick sequence of volcanoclastic sediments (Garwin 2000).

Alteration pattern and vein-types follow the common model for porphyry copper deposits (Sillitoe 2010), with a central zone of biotite alteration associated to quartz stockwork veins hosting most of the copper-iron sulfides (Mitchell et al. 1998; Clode et al. 1999; Arif and Baker 2004). Quartz veins are classified into A-, AB-, and B-veins, becoming thicker, straight-walled and more continuous in this chronological order (Fig. 1A and B). Thin sulfide-veinlets with green chlorite-sericite alteration selvages ("paint-veins"; Fournier 1967) crosscut earlier quartz vein generations. During this stage, primary and secondary biotite is replaced by chlorite and sericite, producing the characteristic pale-green color of the mineralized rocks (Fig. 1B). Pyrite veinlets (D-veins) accompanied by feldspar-destructive sericite-clay alteration are the last veining-stage, crosscutting all other vein-types.

The general positive correlation of ore grade with quartz vein density as well as the spatial overlap of the highly mineralized zone and biotite alteration close to the porphyry center (Mitchell et al. 1998), sulfides are thought

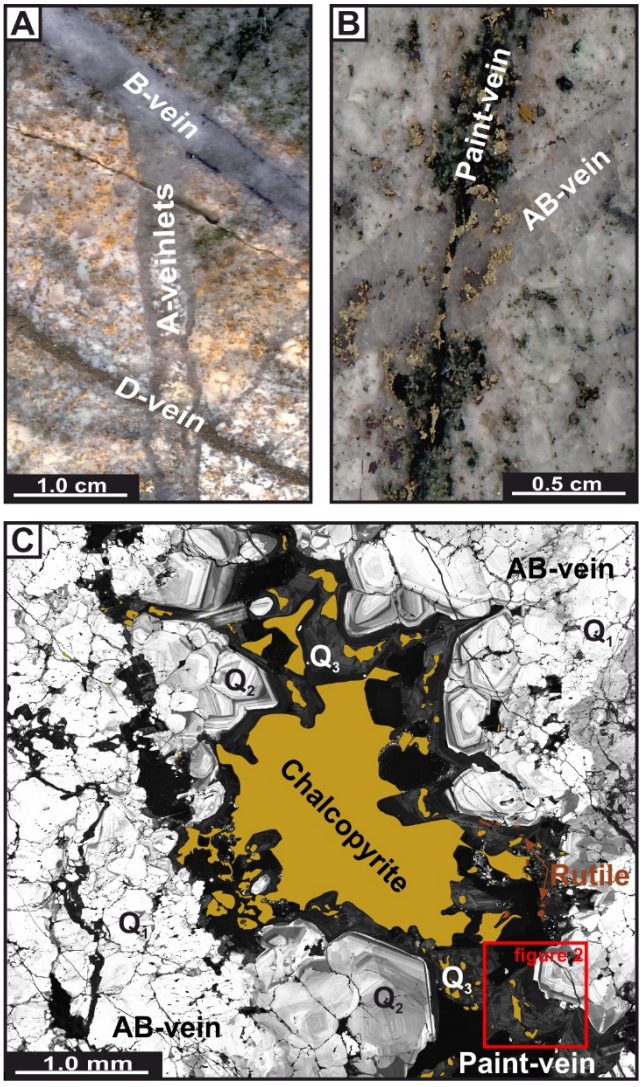

Figure 1. Crosscutting relationships of various vein-types at Batu Hijau (A and B) and textural position of sulfides relative to different quartz generations present within individual quartz veins (C).

to have precipitated during quartz stockwork formation at high temperatures (Garwin 2000; Arif and Baker 2004; Proffett 2009).

Cathodoluminescence (CL) imaging reveals the complex internal structure of quartz veins marked by several superimposed quartz generations and dissolution events (Fig. 1C). Chalcopyrite and bornite hosted by quartz veins are always related to a network of cracks filled with dull-luminescent quartz or to minor euhedral dull-luminescent quartz grains within paint-veins, illustrating a genetic link of sulfide precipitation and paint-vein formation. Consequently, physical and chemical

conditions of ore formation at Batu Hijau might differ significantly from the common model.

2 Insights from fluid inclusions

2.1 Fluid inclusion types and distribution

Four main types of fluid inclusions (FIs) can be distinguished at Batu Hijau based on phase proportions at room temperature: intermediate density (ID) FIs, low-density low-salinity vapor (V) FIs, high-density high salinity brine (B) FIs, and high-density low- to medium-salinity aqueous (A) FIs. Due to the large number of FIs, the unambiguous identification of primary or pseudosecondary FIs is difficult and therefore most inclusions are considered to be of secondary origin.

In quartz veins from the deepest, non-mineralized parts of the deposit the predominant type of FIs are of intermediate density, < 5 to 40 µm big and consisting of liquid and gas in equal proportions. With decreasing depth, the abundance of ID FIs decreases rapidly while B and V FIs become the dominant FI-type within mineralized quartz veins. Polyphase B inclusions contain a small gas bubble (10 – 30 vol.%) and a halite daughter crystal. Many more solids can be present in individual inclusions, including sylvite, hematite, chalcopyrite, anhydrite, and calcite. In V FIs the gas bubble occupies the majority of the inclusion volume (70 – 95 vol.%) and a small triangular chalcopyrite is commonly present. Coexisting B and V FIs on healed fracture planes demonstrate immiscibility of hydrothermal fluids during and after quartz vein formation. All three FI-types (V, ID, and B FIs) are hosted by and are genetically related to bright-luminescent quartz generations in the stockwork veins within the biotite-altered center of Batu Hijau. The dull-luminescent quartz generation enclosing all sulfides post-dates those quartz generations and exclusively hosts A FIs. This inclusion-type consists of a small gas bubble (around 20 vol.%) and liquid. Most A FIs follow the microfracture network healed by dull-luminescent quartz along which the sulfides occur. Rarely, unambiguously primary FIs can be found within euhedral quartz of paint-veins growing into open spaces. On the other hand, pseudosecondary A FI-trails truncated by sulfides along a specific growth zone are commonly present and suggest entrapment immediately before or during sulfide precipitation (Fig. 2).

2.2 Microthermometric characterization

Heating and freezing experiments were conducted on selected fluid inclusion assemblages (FIAs), defined as trails or groups of FIs with similar phase proportions at room temperature (Goldstein and Reynolds 1994).

ID FIs show very homogenous salinities of 3.5 to 4 wt.% $NaCl_{eq}$. with decreasing homogenization temperatures (T_H) from 430° in A- to 350°C in B-veins. The deep barren core of Batu Hijau is assumed to have been formed at paleodepths of around 3 km (Garwin 2000) and the respective pressure corrections indicate entrapment temperatures between 500° and 400°C for A- and B-veins, respectively (Fig. 3).

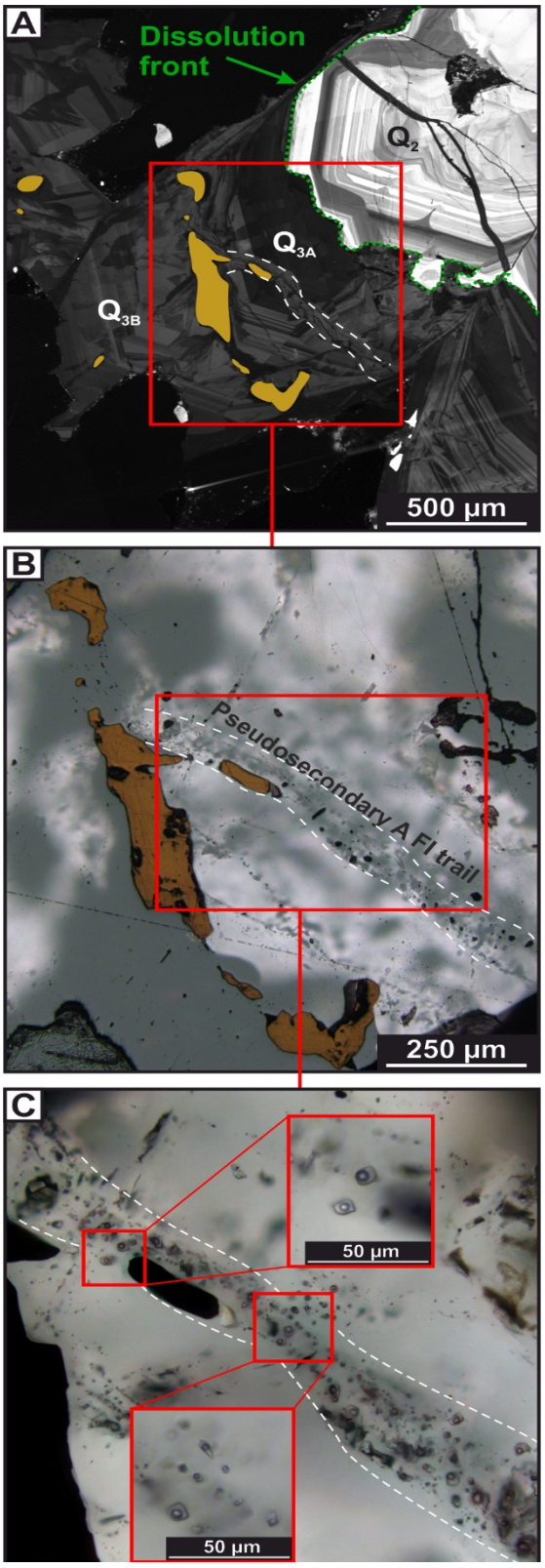

Figure 2. Pseudosecondary trail of A FI with chalcopyrite. A. CL image showing textural position of chalcopyrite, B. Combined reflected and transmitted light image, C. Transmitted light image of A FI trail and individual A FIs.

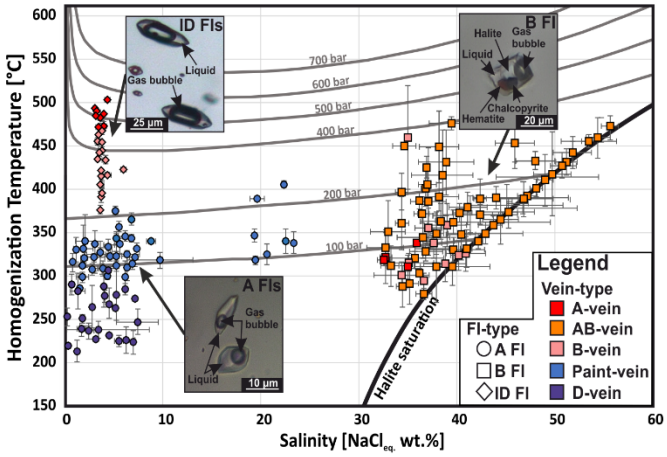

Figure 3. Microthermometry results for different FI types. Note that T_H of ID FIs is pressure corrected.

Poly-phase B FIs homogenized by either bubble disappearance or halite dissolution (FIAs on the halite saturation curve in Fig. 3) at temperatures between 280° and 480°C. The T_H and salinities of B FIs within AB-veins are higher than in B-veins. Most B FIs from boiling trails homogenize within a narrow range from 370 to 390°C and have salinities between 35 and 40 wt.% NaCleq.. Microthermometry results of V FIs are difficult to obtain due to the small amount of liquid present and hence phase-transitions are easy to miss. However, the TH of V FIs should be similar to those of B FIs along boiling trails, and their salinities were calculated using the SoWat software (Driesner 2007, Driesner and Heinrich 2007) to be around 0.1 wt.% NaCleq..

The A FIAs coeval with formation of paint-veins show homogenization temperatures mainly in the range of 310 to 350°C with a few exceptions at lower and higher temperatures. In few cases high salinities of up to 25 wt.% NaCleq. were observed from A FIAs within cores of dull-luminescent euhedral quartz crystals. The majority of pseudosecondary and secondary FIAs, however, have lower salinities between 0.5 to 10 wt.% NaCleq..

Most A FIs from D-veins homogenize at temperatures below 300°C, and their salinities overlap with the lower range of A FIs from paint-veins.

2.3 Chemical composition of fluids

LA-ICP-MS analysis of individual FIs were conducted at ETH Zürich and the results for selected elements are shown in figure 4. In general, analyzed elements can be divided into three different groups based on their behavior during phase separation. For elements like K, Cs, and Rb, ratios relative to Na stay constant within all FI types and hence throughout the lifespan of the hydrothermal system at Batu Hijau. In contrast all detected base metals partitioned into the brine phase, while Li, B, Ag, and As preferred the vapor phase relative to Na during phase separation. Most strikingly however, is the fact that element/Na ratios in ID and A FIs perfectly overlap for most of the elements analyzed.

Copper concentrations within B FIs are very high (up to 10 wt.%) and decrease with decreasing T_H to values as low as 1000 µg/g, whereas Fe concentrations are rather constant at around 10 wt.% over the whole temperature range. The A FIs related to the paint-vein stage and the mineralization have much lower Cu and Fe concentrations, typically between 100 and 1000 µg/g.

3 Porphyry mineralization from a low-salinity fluid at moderate temperatures

Due to the textural position of sulfide grains within or attached to the dull-luminescent quartz generation, mineralization at Batu Hijau postdates locally the formation of quartz stockwork veins, which are characterized by much brighter luminescent quartz (Q_1 and Q_2). In addition, the general absence of B FIs within the dull-luminescent quartz argues against sulfide precipitation from a highly saline fluid, although B FIs contain the highest Cu concentrations of up to several wt.%. Decreasing Cu concentrations of B FIs with lower T_H was interpreted to document sulfide precipitation at Bingham Canyon (Landtwing et al. 2010) and is also observed at Batu Hijau (Fig. 4). However, unchanging Fe concentrations demonstrate that the Cu depletion cannot be the result of chalcopyrite ± bornite precipitation but might be attributed to other effects, such as decreasing partitioning coefficients between liquid and vapor with decreasing temperatures (Zajacz et al. 2017). Occasionally detectable sulfur concentrations in B FIs (not shown here) also stay constant and do not decrease with temperature.

The occurrence of A FIs within dull-luminescent quartz as pseudo- and secondary trails imply that they represent the fluid present either during or immediately before sulfide precipitation. Consequently, Cu and Fe concentrations of A FIs represent either the remaining amount of these metals after or the initial amount before

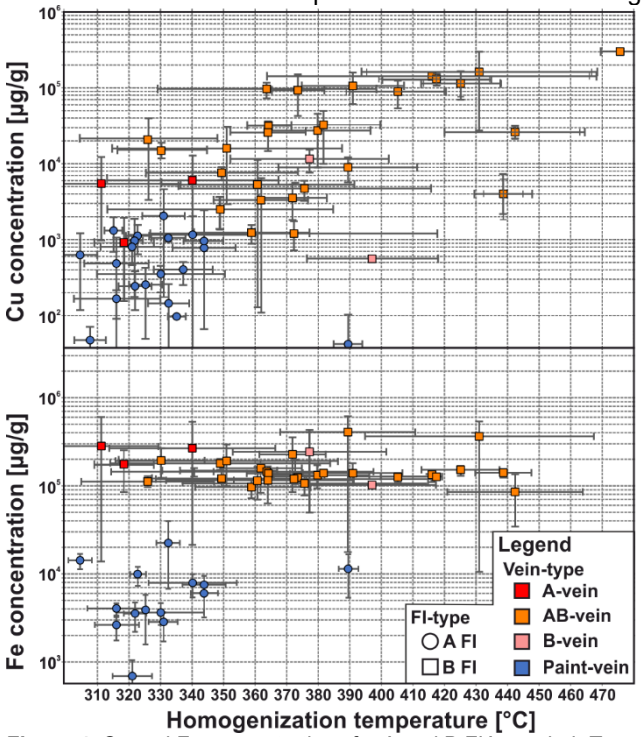

Figure 4. Cu and Fe concentrations for A and B FIAs vs their T_H.

sulfide precipitation. Even if the analyzed average Cu concentration of around 730 μg/g is regarded as the maximum of Cu dissolved in the low-salinity fluid, a medium-sized magma chamber of 47.5 km^3 would be able to produce the required amount of fluid for transporting the copper at Batu Hijau (assuming 100% precipitation efficiency and initial magmatic water contents of 5 wt.%). Main trigger for sulfide precipitation was cooling over a temperature interval from 350° to 310°C as indicated by T_H of A FIs. The Ti-in-quartz (Huang and Audétat 2012) and the chlorite thermometer (Jowett 1991), indicate a comparable range of temperatures (370° to 330°C and 350° to 290°C, respectively) for the formation of paint-veins and their characteristic alteration.

Based on the chemical similarities between ID and A FIs, the mineralizing fluid represents an ascending and cooling magmatic fluid, which becomes denser (from 0.55 to 0.75 g/cm^3). Without any drastic depressurization event, like the change from lithostatic to hydrostatic regime (Fournier 1999) that caused phase separation of previous fluid pulses, the ascending fluid stays within the single-phase field following a path of decreasing pressure and temperature parallel to the two-phase boundary. Mixing with variable amounts of vapor and brine explains the range of salinities in A FIs (Fig. 3). However, the bulk composition of the mineralizing fluid changed only slightly. Constant fluid chemistry from initial magmatic fluids, entrapped as ID FIs in A-veins of the deep barren core, to the mineralizing fluid represented by A FIs demonstrate that no significant processes within the magma chamber or the hydrothermal system, like phase separation or intensive mixing with meteoric fluids, were important for the porphyry Cu-Au mineralization at Batu Hijau.

4 Conclusion and outlook

Detailed petrographic observations, microthermometry, and LA-ICP-MS analyses of FIs entrapped during or slightly before sulfide precipitation support ore formation at moderate temperatures (350° to 310°C) from a low-salinity high-density fluid during the paint-vein stage characterized by chlorite-sericite alteration. Similar conditions for sulfide precipitation have been reported from several other porphyry copper deposits, such as Santa Rita (Reynolds and Beane 1985), Far Southeast (Hedenquist et al. 1998), El Teniente (Klemm et al. 2007), and Nuevo Chaquiro (Bartos et al. 2017). This study emphasizes that paint-veins and apparently disseminated Cu-Fe-sulfides texturally postdating quartz vein formation carry the greatest part of Cu and probably Au, even in a deposit that was traditionally considered a typical example of high-temperature bornite-rich Cu-Au mineralization.

Acknowledgements

We would like to thank the geology staff at Batu Hijau, who hosted and guided us during our visits. Special thanks go to Oscar Laurent for helping with the LA-ICP-MS analyses and Tobias Zwyer for collecting some of the samples used in this project. This research was funded by the Swiss National Science Foundation (project 200020_166151).

References

Arif J, and Baker T (2004) Gold paragenesis and chemistry at Batu Hijau, Indonesia: implications for gold-rich porphyry copper deposits. Miner Deposita 39:523-535

Bartos PJ, Garcia C, Gil J (2017) The Nuevo Chaquiro Cu-Au-(Mo) porphyry deposit, Middle Cuaca Belt, Colombia: Geology, alteration, mineralization. Econ Geol 112:275-294

Clode CH, Proffett JM, Munajat I (1999) Timing relationship of intrusion, wall-rock alteration, and mineralization in the Batu Hijau copper-gold deposit. Proceedings Pac-Rim Congress, 10-13 October 1997, Bali, pp 485-498

Driesner T (2007) The system H_2O-NaCl. II. Correlation for molar volume, enthalpy, and isobaric heat capacity from 0 to 1000 degrees C, 1 to 5000 bar, and 0 to 1 X_{NaCl}. Geochim Cosmochim Acta 71:4902-4919

Driesner T, and Heinrich CA (2007) The system H_2O-NaCl. I. Correlation formulae for phase relations in temperature-pressure-composition from 0 to 1000°C, 0 to 5000 bar, and 0 to 1 X_{NaCl}. Geochim Cosmochim Acta 71:4880-4901

Fournier RO (1967) The porphyry copper deposit exposed in the Liberty open-pit mine near Ely, Nevada. Part I. Syngenetic formation. Econ Geol 62:57-81

Fournier RO (1999) Hydrothermal processes related to the movement of fluid from plastic to brittle rock in the magmatic-epithermal environment. Econ Geol 94:1193-1211

Garwin SL (2000) The setting, geometry and timing of intrusion-related hydrothermal systems in the vicinity of Batu Hijau porphyry copper-gold deposit, Sumbawa, Indonesia. PhD Thesis, University of Western Australia, Nedlands, 320 pp

Goldstein RH, and Reynolds TJ (1994) Systematics of fluid inclusions in diagenetic minerals. Society for sedimentary Geology, 199pp

Jowett EC (1991) Fitting iron and magnesium into the hydrothermal chlorite geothermometer. GAC/MAC/SEG Joint annual meeting, 16, Toronote, Canada

Hedenquist JW, Arribas A, Reynolds TJ (1998) Evolution of an intrusion-centered hydrothermal system: Far Southeast-Lepanto porphyry and epithermal Cu-Au deposits, Philippines. Econ Geol 93:373-404

Huang R and Audétat A (2012) The titanium-in-quartz (TitaniQ) thermobarometer: A critical examination and re-calibration. Geochim Cosmochim Acta 84:75-89

Klemm LM, Pettke T, Heinrich CA, Campos E (2007) Hydrothermal evolution of the El Teniente deposit, Chile: Poprhyry Cu-Mo ore deposition from low-salinity magmatic fluids. Econ Geol 102:1021-1045

Landtwing MR, et al. (2010) The Bingham Canyon porphyry Cu-Au-Mo deposit. III. Zoned copper-gold ore deposition by magmatic vapor expansion. Econ Geol 105:91-118

Mitchell PA, Proffett JM, Dilles JH (1998) Geological review of the Batu Hijau porphyry copper-gold deposit, Sumbawa, Indonesia. Internal report to PT Newmont Nusa Tenggara, Nusa Tenggara Barat, Indonesia, 164 pp

Proffett JM (2009) High Cu grades in porphyry Cu deposits and their spatial relationship to emplacement depth of magmatic resources. Geol 37:675-678

Reynolds TJ, and Beane RE (1985) Evolution of hydrothermal fluid characteristics at the Santa Rita, New Mexico, porphyry copper deposit. Econ Geol 80:1328-1347

Sillitoe RH (2010) Porphyry copper systems. Econ Geol 105:3-41.

Zajacz Z, Candela PA, Piccoli PM (2017) The partitioning of Cu, Au and Mo between liquid and vapor at magmatic temperatures and its implications for the genesis of magmatic-hydrothermal ore deposits. Geochim Cosmochim Acta 207:81-101

Magnetite alteration and formation of porphyry Cu (Au) deposits

Huaying Liang, Wenting Huang, Weidong Sun, Long Ren
Key Laboratory of Mineralogy and Metallogeny, Guangzhou Institute of Geochemistry, Chinese Academy of Sciences, China

Abstract. Porphyry Cu-Au(±Mo) deposits are usually associated with highly oxidized felsic magmas and the sulfur in the magmas is present as sulfate. The high oxidation state not only triggers the destruction of sulfide from the source of magma and formation of magmas with high concentrations of chalcophile element and sulfur, but also leads to enrichment of chalcophile element and sulfur in evolved magmas, given that the sulfur remains as sulfate in the magmas. The sulfur presents mainly as sulfide in porphyry Cu-Au(±Mo) deposits. Magnetite is found in almost all porphyry Cu(±Au±Mo) deposits. It is suggested that a redox reaction of Fe^{2+} to Fe^{3+} and S^{6+} to S^{2-}, leading the formation of magnetite provides enough S^{2-} for sulfide precipitation and plays a key role in the formation of porphyry Cu-Au deposits. It is concluded that porphyry ore prospect targeting should be focused on areas with low magnetic susceptibility in regions with high magnetic susceptibility.

1 Sulfur species in porphyry Cu-Au(±Mo) magmas

Giant porphyry Cu-Au(±Mo) deposits contain not only high concentrations of metals such as Cu and Au, but also a very large sulfur budget, usually over 1 billion tons (Chambefort et al. 2008). The high oxidation triggers the destruction of sulfide from the sources of magma and the formation of magmas with high concentrations of chalcophile element and sulfur. Almost all giant porphyry Cu-Au(±Mo) deposits have genetic link to oxidized magmas (Sillitoe 1997; Mungall et al. 2002; Liang et al. 2009; Sun et al. 2013), usually with oxygen fugacity ($\log fO_2$) >FMQ+2 (Sun et al. 2013). Sulfur remains as sulfate in magmas with FMQ>2 (Fig. 1) (Jugo et al. 2005) Anhydrite inclusions in quartz phenocrysts found in the Yulong giant porphyry Cu-Au deposit indicate also that sulfate is the dominant species in oxidized magmas. This keeps magmas sulfide undersaturated during ascending and evolution, which favors enrichment of chalcophile elements and sulfur and provides enough metal and sulfur for the formation of giant porphyry Cu-Au(±Mo) deposits.

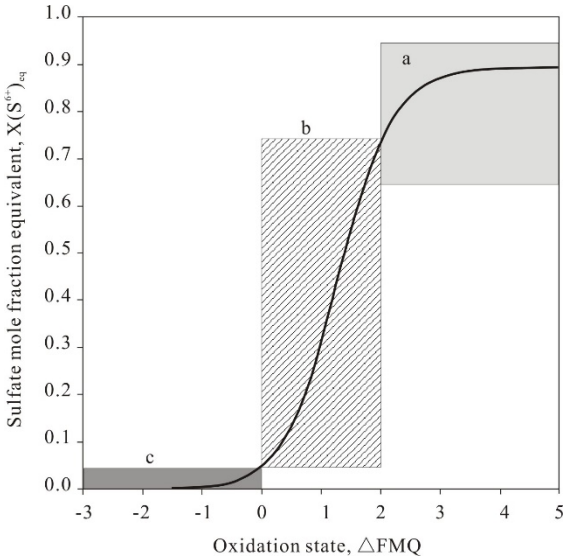

Figure 1. Sulfur speciation vs. oxygen fugacity, modified after Jugo et al. (2005). (a) magmatic stage; (b) pre-ore magnetite alteration stage; and (c) main mineralization stage

2 Sulfur species in porphyry Cu-Au(±Mo) deposits

Ore minerals of porphyry deposits are composed primary of sulfides, such as chalcopyrite, bornite, pyrite, molybdenite, galena, sphalerite, etc. and therefore, the S^{2-} is the dominant species in the porphyry main mineralization stage (Fig. 1c). Daughter mineral assemblages of chalcopyrite and ± anhydrite were found in fluid inclusions from the early stage and main stage mineralization in the Yulong porphyry Cu-Au deposit (Fig. 2a, 2b) (Liang et. 2009), respectively, suggesting that the S^{6+} and S^{2-} coexist in the early stages of mineralization (Fig. 1b) and S^{2-} is the dominant species in the main stage mineralization (Fig. 1c). It is therefore, that the sulfur remains dominantly as S^{6+} in magma stage, S^{6+} and S^{2-}

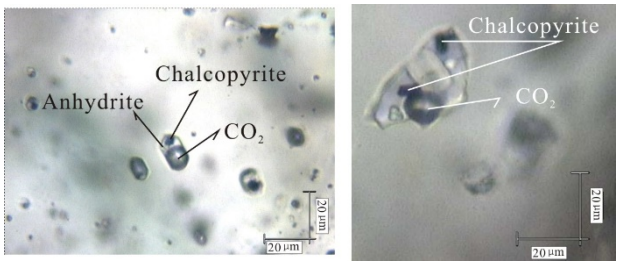

Figure 2. Daughter mineral assemblage in fluid inclusion from the early (a) and main (b) stage mineralization in the Yulong giant porphyry Cu-Au deposit

in the early mineralization state, and dominantly as S^{2-} in the main mineralization stage (Fig. 1). The presence of S^{6+} and S^{2-} could be due to sulfate reduction or the disproportionation of SO_2 during fluid cooling. The S^{2-} dominated in main mineralization stage should triggered mainly by sulfate reduction rather than disproportionation of sulfate. The final large scale precipitation of sulfide is controlled by sulfate reduction. What kinds of processes trigger the redox reaction?

3 Magnetite alteration and redox reaction of sulfate to sulfide in porphyry Cu-Au ore forming systems

Sulfur species in magmatic-hydrothermal system are controlled by redox potential (Fig. 1). The redox potential is usually buffered by redox-sensitive elements such as C, H, S and Fe (Evans 2006), through reaction involving mafic minerals (Carmichael 1991) and oxides (Sun et al. 2004). Fe is the most effective and abundant redox agent in magmas. The most abundant mafic silicate minerals in porphyries are amphibole and biotite. Biotite usually contains minor amount of Fe^{3+}, while amphibole has $Fe^{3+}/(Fe^{3+}+Fe^{2+})$ ratios less than 30%. Fe^{3+} in magnetite accounts for more than 66% percent of the total Fe. Once mafic silicate minerals are replaced by magnetite, a large amount of Fe^{2+} must be oxidized to Fe^{3+}. The Fe^{2+} could act as important reducing agent that reduces the S^{6+} to S^{2-} in the porphyry ore forming system during magnetite alteration (Sun et al. 2004) as shown by the following equation:

$$12[FeO] + H_2SO_4 = 4Fe_3O_4 + H_2S \quad (1)$$

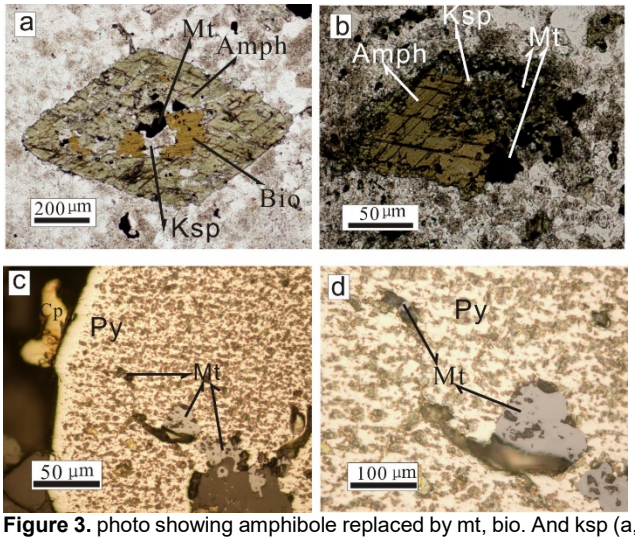

Figure 3. photo showing amphibole replaced by mt, bio. And ksp (a, b) and Mt by Py (c, d). Amph: amphibole, Mt.: magnetite, Ksp: K-feldspar, Bio: biotite, Py: pyrite

Magnetite usually occurs in the potassic alteration zone and shows a close association with K-feldspar (Fig. 3a, b). This association could be illustrated by the following reaction:

$$8KFe_3AlSi_3O10(OH)_2 + 2H_2SO_4 = 8KAlSi_3O_8 + 8Fe_3O_4 + 8H_2O + 2H_2S \quad (2).$$

Fe^{2+} could be transported by low-density aqueous vapor at high pressures in magmatic-hydrothermal ore forming system (Simon et al. 2004). The oxidation of Fe^{2+} transported by magmatic fluid could form magnetite as shown by the following equation (Field et al 2005):

$$12FeCl_2 + 12H_2O + H_2SO_4 = 4Fe_3O_4 + 24HCl + H_2S \quad (3)$$

The above three reactions indicate that the formation of magnetite could transfer S^{6+} to S^{2-}, which supplies enough reduced sulfur to the porphyry ore forming system, favoring the precipitation of sulfide minerals in porphyry ore forming system.

Magnetite alteration is commonly found in the early alteration stages of porphyry ore deposits (Sillitoe, 1997; Liang et al. 2009). Magnetite in porphyry Cu-Au deposits was inferred to form either prior to potassic alteration, or during the main stage potassic alteration (Arancibia and Clark 1996). Given sulfate is the dominant species in oxidized porphyry magmas, magnetite alteration prior to main stage mineralization, which could transform sulfate in magmas to reduced sulfur in mineralization stage, plays a key role in the formation of porphyry Cu-Au deposits.

4 Implication for porphyry ore exploration

Magnetite is abundant in porphyry Cu-Au deposits and it is therefore that ore bearing porphyries are characterized by high magnetic susceptibility. Intense sodic-calcic or potassic alteration would increase the abundance of magnetite. Hydrolytic alteration would destroy magnetite. This is due to the reaction of magnetite with H_2S to form pyrite in the acidic condition (Fig. 3 c, d). The relatively strong mineralization zone should have low magnetite susceptibility. Porphyry ore prospecting target should focus on areas with low magnetic susceptibility in a region with high magnetic susceptibility.

Acknowledgements

This work was financially supported by the Natural Science Foundation of China (Grants 41772065) and the National Key R&D Program of China (Grant 2016YFC0600407).

References

Arancibia ON, Clark AH (1996) Early magnetite-amphibole-plagioclase alteration-mineralization in the Island Copper porphyry copper-gold-molybdenum deposit British Columbia. Economic Geology 91(2): 402-438

Carmichael ISE (1991) The redox stage of basic and silicis magmas: a reflection of their source regions?. Contributions to Mineralogy and Petrology 103:129-141

Chambefort I, Dilles JH, Kent AJR (2008) Anhydrite-bearing andesite and dacite as a source for sulfur in magmatic-hydrothermal mineral deposits. Geology 36 (9): 719-722Evans KA (2006) Redox decoupling and redox budgets; conceptual tools for the study of Earth systems. Geology 34(6): 489-492

Field CW, Zhang L, Dilles JH, Rye RO, Reed MH (2005) Sulfur and oxygen isotopic record in sulfate and sulfide minerals of early, deep, pre-Main Stage porphyry Cu-Mo and late Main Stage base-metal mineral deposits, Butte district, Montana. Chemical Geology 215 (1-4):61-93

Liang HY, Sun WD, Su WC, Zartman RE (2009) Porphyry copper-

gold mineralization at Yulong, China, promoted by dercrasing redox potential during magnetite alteration. Economic Geology 104 (9):587-596

Jugo PJ, Luth RW, Richard JP (2005) Experimental data on the speciation of sulfur as a function of oxygen fugacity in basaltic melts. Geochimica Et Cosmochimica Acta 69 (2):497-503

Mungall JE (2002) Roasting the mantle: Slab melting and the genesis of major Au and Au-rich Cu deposits. Geology 30(10): 915-918

Sillitoe RH (1997) Characteristics and controls of the largest porphyry copper-gold and epithermal gold deposits in the circum-Pacific region. Australian Journal of Earth Sciences 44(3):373-388

Simon AC, Pettke T, Candela PA, Piccoli PM, Heinrich CA (2004) Magnetite solubility and iron transport in magmatic-hydrothermal environments. Geochimica Et Cosmochimica Acta 68(23):4905-4914

Sun WD, Arculus RJ, Kamenetsky VS, Binns RA (2004) Release of gold-bearing fluids in convergent margin magmas prompted by magnetite crystallization. Nature 431:975-978

Sun WD, Liang HY, Ling MX, Zhan MZ, Ding X, Zhang H, Yang XY, Li YL, Ireland TR, Wei QR, Fan WM (2013) The link between reduced porphyry copper deposits and oxidized magmas. Geochimica Et Cosmochimica Acta 68(23):4905-4914

Chlorite alteration in porphyry Cu systems: New insights from mineralogy and mineral chemistry

Bing Xiao, Huayong Chen, Yuzhou Feng,
Key Laboratory of Mineralogy and Metallogeny, Guangzhou Institute of Geochemistry, Chinese Academy of Sciences, China

Pete Hollings
Geology Department, Lakehead University, Canada

Yu Zhang
School of Geosciences and Info-Physics, Central South University, China

Abstract. Chlorite is one of the most widely developed hydrothermal alteration minerals in porphyry deposits, and provides an important tool to investigate the nature of fluid-rock reactions and mass transfer during hydrothermal fluid advection. Samples of chlorite from alteration systems around three large porphyry Cu deposits, i.e., Tuwu (NW China), Atlas (Philippines) and Xiaokelehe (NE China), were used to investigate element transfer between chlorite and pyroxene, amphibole and biotite during alteration.

Hydrothermal titanite occurred together with chlorite in all samples. Titanite formed during chlorite alteration of biotite has higher Al_2O_3 and F contents compared with that formed during hornblende and pyroxene chloritization. There is a clear elemental transition zone which occurs between biotite and chlorite, whereas there are no transitions between hornblende or pyroxene with chlorite. FeO_T and MgO contents of chlorite are more likely controlled by the crystal structure of the precursor minerals (not only the compositions), whereas TiO_2 and Al_2O_3 are probably controlled by the similar formation temperature of chlorite without obvious influence of precursor minerals. Thus, TiO_2 and Al_2O_3 contents of chlorite could be more suitable to be used as mineral geochemical vectoring tool in exploration of porphyry deposits.

1 Introduction

Chlorite mainly forms through replacement of ferromagnesian minerals (such as biotite, hornblende and pyroxene) as a result of hydrothermal fluids (Walker 1993). The detailed process and mechanism of element transport and enrichment during chlorite alteration is relatively poorly understood (Hart et al. 2016), and the impacts of chemical concentrations of precursor minerals on chlorite have received attention (Wilkinson et al. 2015; Xiao et al. 2018). We focus on chlorite alteration of biotite, hornblende and pyroxene in porphyry deposits, and investigate how the chemistry and texture of precursor minerals affect chlorite compositions based on detailed mineralogical observation and geochemical analysis.

2 Sampling

Granodiorite porphyry samples from Xiaokelehe, quartz diorite porphyry samples from Atlas, and basalt samples from the Tuwu Cu deposit, were collected. Representative samples were examined with EMPA to aid mineral identification and determine compositions. Samples containing chlorite were all selected from major alteration zones of porphyry deposits. They include chlorite alteration of 1) biotite in the Xiaokelehe granodiorite; 2) biotite in the Atlas quartz diorite; 3) hornblende in the Atlas quartz diorite and 4) pyroxene in the Tuwu basalt.

3 Chlorite alteration processes in porphyry deposits

Two approaches have been proposed for using the chemical composition of chlorite to determine the formation temperature: (1) the use of empirical calibrations based on the tetrahedral aluminium (Al^{IV}) occupancy as a function of measured temperature in geothermal systems (Cathelineau 1988), and (2) thermodynamic calculation of equilibrium conditions for chlorites (Walshe 1986). For the thermodynamic method the chlorites must coexist with quartz, which is not consistent within this study. We calculated the chlorite formation temperatures using the chlorite thermometer of Cathelineau (1988) which yielded temperatures of 249 - 278 °C (average of 264 °C) for Xiaokelehe chlorite; 212 - 282 °C (average of 264 °C) for Atlas Type A chlorite; 265 - 304 °C (average of 282 °C) for Atlas Type B chlorite; 254 - 295 °C (average of 273 °C) for Tuwu chlorite. The temperature ranges for all the chlorite studied are broadly the same.

In Xiaokelehe and Atlas samples, chlorite replaced biotite along the cleavage and is associated with the formation of abundant titanite grains. In all samples the K_2O, Na_2O, TiO_2, SiO_2, F and Cl concentrations decrease, while MgO, FeO_T, Al_2O_3 and MnO concentrations increase from biotite to chlorite, over a gradual transition zone. Both titanite and chlorite contain no or limited Na, K and Cl, suggesting that the process of biotite chloritization results in Na, K, and Cl entering the hydrothermal fluid rather than chlorite or titanite. In the

compositional profiles through hornblende and pyroxene to chlorite, there are sharp contacts between hornblende/pyroxene and chlorite. Atlas hornblende contains Na_2O = 1.18 – 1.64 wt.% and K_2O = 0.21 – 0.47 wt.%, and Tuwu pyroxene contain Na_2O = 0.33 – 0.42 wt.%, whereas Na_2O and K_2O contents of chlorite formed from Atlas hornblende and Tuwu pyroxene are either close to or below the detection limits of EPMA. This suggests that chloritization releases Na and K of Atlas hornblende, and Na of Tuwu pyroxene to enter into the hydrothermal fluid. Biotite and chlorite are both phyllosilicate minerals, whereas pyroxene is a single-chain silicate and hornblende is a double chain silicate. The similarity between the structure of chlorite and biotite means that chlorite is more likely to inherit part of biotite structure during alteration which would explain the gradual transition between biotite and chlorite, compared to the abrupt transition between hornblende/pyroxene and chlorite.

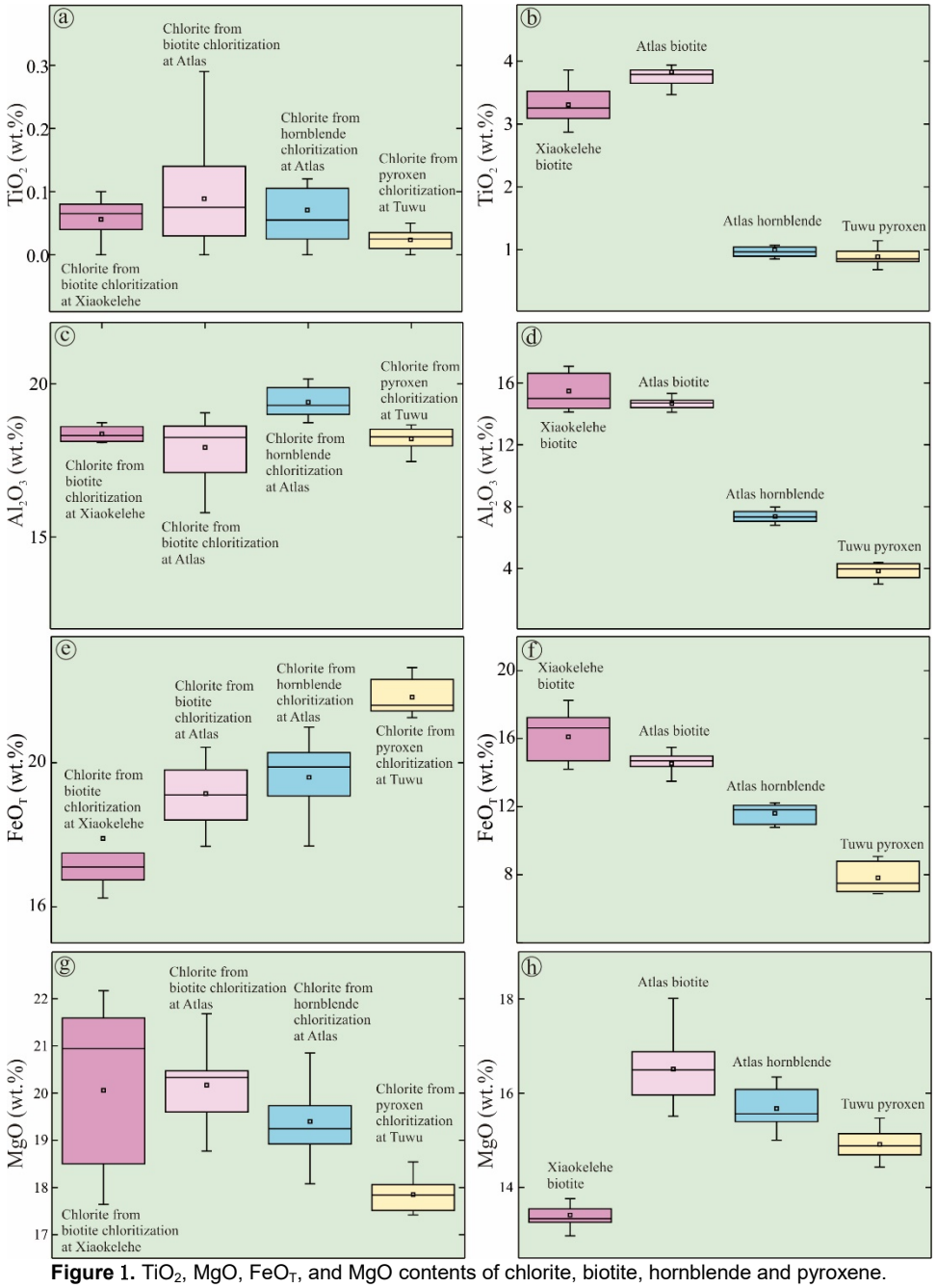

Figure 1. TiO_2, MgO, FeO_T, and MgO contents of chlorite, biotite, hornblende and pyroxene.

4 Genesis of hydrothermal titanite in chlorite alteration

Titanite is a dominant Ti-bearing phase and widespread accessory mineral in igneous rocks, metamorphic rocks, and hydrothermal mineral deposits, such as porphyry and skarn deposits (Xie et al. 2018). In this study, titanite coexists with chlorite formed by the alteration of biotite,

hornblende and pyroxene in all samples from the three porphyry systems. In Xiaokelehe and Atlas samples with biotite chloritization, needle-like titanite grains occur along cleavage of biotite, whereas it occurs as irregular crystals associated with Atlas hornblende and Tuwu pyroxene chloritization, which may be possibly related to different crystal structure of precursor minerals. Titanite grains in this study all exhibit good negative linear relationships between Al_2O_3 + FeO_T and TiO_2, and positive relationships between Al_2O_3 + FeO_T and F, indicating that Al and Fe substitute into the Ti octahedral site with an additional Al-involving reaction ($(Al, Fe)^{3+}$ + $(F, OH)^- \leftrightarrow Ti^{4+} + O^{2-}$; Xie et al. 2018). In addition, nearly all titanite grains plot within the hydrothermal titanite field consistent with their occurrence with hydrothermal chlorite.

The occurrence of titanite associated with chlorite alteration suggests the transfer of abundant Ca and Ti from the hydrothermal fluid or precursor minerals. The Xiaokelehe biotite, Atlas biotite and hornblende, and Tuwu pyroxene have high TiO_2 contents (2.95 – 3.86 wt.%, 3.32 – 4.81 wt.%, 0.85 – 1.43 wt.% and 0.68 – 1.14 wt.%, respectively), whereas Xiaokelehe and Atlas biotite only has minor Ca. This suggests that the Ti was likely derived from the precursor minerals, whereas Ca was derived from hydrothermal fluids and/or precursor minerals (such as hornblende and pyroxene). Our results also suggest that Ti could be transported into hydrothermal solutions of porphyry Cu deposits, although it is typically considered to be an immobile element in hydrothermal environments (Jiang et al. 2005). Titanite formed during chloritization at Xiaokelehe and Atlas contains higher Al_2O_3 and F contents than titanite formed in Atlas hornblende and Tuwu pyroxene, whereas, Xiaokelehe and Atlas biotite has higher Al_2O_3 and F contents than Atlas hornblende and Tuwu pyroxene. These results suggest that Al_2O_3 and F contents of titanite may be controlled by the chemistry of the precursor minerals.

5 Impacts of precursor mineral on chlorite compositions

The hydrothermal fluids that generated chlorite alteration at Xiaokelehe, Atlas, and Tuwu are all related to porphyry systems and were likely broadly similar, consistent with the similar formation temperatures. TiO_2 and Al_2O_3 contents of all the chlorites studies are generally similar (Figs. 1a, c), regardless of the variable TiO_2 and Al_2O_3 contents of precursor minerals (Figs. 1b, d). Xiao et al. (2018) found that TiO_2 and Al_2O_3 contents of chlorite correlate positively with formation temperature of chlorite. This would suggest that TiO_2 and Al_2O_3 contents of chlorite may be mainly controlled by formation temperatures rather than the concentration of the precursor minerals. However, FeO_T and MgO contents of chlorite are influenced by precursor minerals (Figs. 1e-h). For example, FeO_T contents of chlorite increase with its decreasing trend in precursor minerals (Figs. 1e, f); MgO contents are variable in precursor minerals but uniformly high in chlorite altered from biotite (Figs. 1g, h). Obviously, these concentrations are not controlled simply by their abundances in precursor minerals. Instead, these unexpected variations could be caused by different crystal structure of precursor minerals. Compared to pyroxene and hornblende, during chlorite alteration process of biotite, the octahedral-site Al^{3+} and Fe^{3+} will be moved out from biotite and more Mg^{2+}-Fe^{2+} occupied the octahedral sites in chlorite structure, which can further decrease the FeO_T content of chlorite but the MgO can always be increased due to substitution of Mg and Fe in chlorite (Foster 1962). In summary, FeO and MgO contents of chlorite are clearly affected by precursor minerals (including both composition and texture) compared to Ti_2O and Al_2O_3 which are possibly mainly controlled by temperature or other factors.

Acknowledgements

This study was funded by the Chinese National Science Fund for Chinese National Science Foundation (41702068), Distinguished Young Scholars (41725009) and Chinese academy of sciences strategic pilot science and technology special (XDB18030206).

References

Cathelineau M (1988) Cation Site Occupancy in Chlorites and Illites as a Function of Temperature. Clay Minerals 23:471–485

Foster MD (1962) Interpretation of the composition and a classification of the chlorites. Geological Survey Professional Paper

Hart L, Wilkinson J, Armstrong R, Araujo D (2016) Element mobility during propylitic alteration in porphyry ore systems: a case study of the Oyu Tolgoi deposits, Mongolia. Applied Earth Science 125:84

Jiang SY, Wang RC, Xu XS, Zhao KD (2005) Mobility of high field strength elements (HFSE) in magmatic-, metamorphic-, and submarine-hydrothermal systems. Physics and Chemistry of the Earth, Parts A/B/C 30:1020–1029

Walker JR (1993) Chlorite polytype geothermometry. Clays and Clay Minerals 41:260

Walshe JL (1986) A six-component chlorite solid solution model and the conditions of chlorite formation in hydrothermal and geothermal systems. Economic Geology 81:681–703

Wilkinson JJ, Chang ZS, Cooke DR, Baker MJ, Wilkinson CC, Inglis S, Chen HY, Bruce Gemmell J (2015) The chlorite proximitor: A new tool for detecting porphyry ore deposits. Journal of Geochemical Exploration 152:10–26

Xiao B, Chen HY, Hollings P, Wang YF, Yang JT, Wang FY (2018) Element transport and enrichment during propylitic alteration in Paleozoic porphyry Cu mineralization systems: Insights from chlorite chemistry. Ore Geology Reviews 102:437–448

Xie GQ, Mao JW, Bagas L, Fu B, Zhang ZY (2018) Mineralogy and titanite geochronology of the Caojiaba W deposit, Xiangzhong metallogenic province, southern China: implications for a distal reduced skarn W formation. Mineralium Deposita Doi: 10.1007/s00126-018-0816-2

Porphyry Cu(Mo) deposits of the Urals: insights from molybdenite trace element geochemistry

Olga Y. Plotinskaya, Vera D. Abramova
Institute of Geology of Ore Deposits, Petrography, Mineralogy, and Geochemistry, Russian Academy of Sciences, Moscow, Russia

Dmitry Bondar
University of Bayreuth, Germany

Reimar Seltmann, John Spratt
Natural History Museum, Department of Earth Sciences, CERCAMS, London, UK

Abstract. The first data on EMPA and LA-ICPMS study of molybdenite from four porphyry deposits of the South and Middle Urals (Tomino, Mikheevskoe and Benkala porphyry Cu and Talitsa porphyry Mo deposits) are presented. It is shown that most trace elements form mineral inclusions within molybdenite in all the deposits studied; only Re and W are most likely to be incorporated into the molybdenite lattice. Porphyry Cu deposits (Tomino and Mikheevskoe) formed within oceanic arc settings are featured by high contents of Re (mostly over 400 ppm) and low contents of W (<10 ppm) in molybdenite; porphyry Cu deposits from Andean-type geotectonic environment (Benkala) are featured by lower Re content (hundreds ppm) and high contents of W (tens ppm) in molybdenite. Molybdenite from porphyry deposits from collisional setting (Talitsa) has low content of Re and elevated W contents (tens ppm). It is demonstrated that trace element geochemistry of molybdenite is a useful tool to define the source of metal components and the geotectonic environment for porphyry Cu(Mo) deposits.

1 Introduction

Porphyry Cu (±Mo,Au) deposits of the Urals (Fig. 1) can be subdivided into the following groups according to their link to subduction zones of different ages (Plotinskaya et al. 2017):

(1) Deposits of the East-Uralian volcanic terrane related to Silurian intra-oceanic arc: porphyry Cu deposits of the Birgilda-Tomino ore cluster and several subeconomic occurrences.

(2) Deposits within the Magnitogorsk volcanic megaterrane linked to the Magnitogorsk intra-oceanic arc which was active from Early Devonian (Emsian) and collided with the East European plate in the Late Devonian (Famennian). These are Middle Devonian Salavat and Voznesenskoe porphyry Cu deposits, and Late Devonian Yubileinoe porphyry Au deposit and Verkhneuralskoe porphyry Mo occurrence

(3) Deposits located in the Trans-Uralian megaterrane and linked to the Late-Devonian to Carboniferous subduction events. This is the Late Devonian to Early Carboniferous Mikheevskoe porphyry Cu deposit linked to an intra-oceanic arc. Tevelev et al. (2006) however supposed a subduction under the accretion prism on the eastern margin of the East-Uralian microcontinent. This group includes also Early Carboniferous deposits formed due to eastward Andean-type subduction under the Kazakh continent (Benkala porphyry Cu deposit and several occurrences).

(4) Continent-continent collision of the East European plate and the Kazakh continent in the Late Carboniferous produced the Talitsa porphyry Mo deposit located in the East Uralian megaterrane.

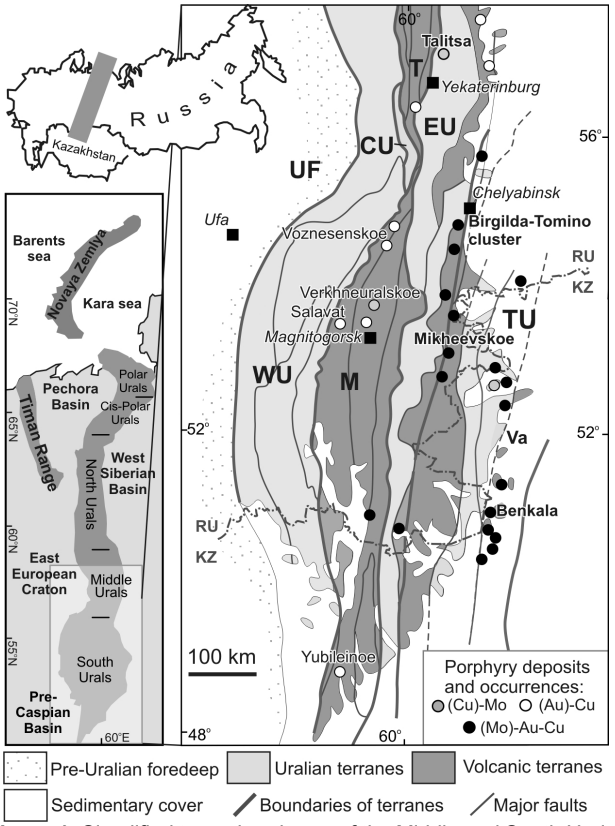

Figure 1. Simplified tectonic scheme of the Middle and South Urals, and locations of porphyry deposits and occurrences, modified after (Petrov et al. 2007; Plotinskaya et al. 2017). Terranes: WU – West Uralian; CU – Central Uralian; T – Tagyl; M – Magnitogorsk; EU – East Uralian, TU – Trans Uralian (Va – Valerianovka volcanic terrane).

This paper presents first data on EMPA and LA-ICPMS study of molybdenite from selected Cu(Mo) deposits and attempts to discuss the obtained regularities in terms of trace element geochemistry of molybdenite and geotectonic settings of the deposits.

2 Analytical methods

The chemical compositions of ore and gangue minerals were determined using a Zeiss EVO 15LS scanning electron microscope with an Oxford Instruments X-Max EDX detector (Natural History Museum, London). X-ray mapping and point analyses of molybdenite were performed using a Cameca SX-100 electron microprobe with five WDX spectrometers (Natural History Museum, London, UK). Farther details are described in Plotinskaya et al. (2018). The trace element data of molybdenite were acquired using the New Wave 213UP laser coupled with the Thermo X Series2 quadrupole ICP-MS (IGEM RAS, Moscow). The following isotopes were measured S^{33}, V^{51}, Fe^{57}, Co^{59}, Ni^{60}, Cu^{65}, Zn^{66}, As^{75}, Se^{77}, Mo^{95}, Ag^{107}, Sn^{118}, Cd^{111}, Sb^{121},Te^{125}, W^{182}, Re^{185}, Re^{187}, Au^{197}, Hg^{202}, Tl^{205}, Pb^{208}, Bi^{209}. In addition Si^{29}, Ti^{47}, and Ca^{43} were measured in order to reveal mineral inclusions but were not calculated. External standards were in-house pyrrhotite for Re and MASS-1 for the remaining elements; S was used as internal standard based on molybdenite stoichiometry. The analyses were obtained from line profiles with laser diameter 30 and 40 µm, laser frequency of 15 Hz, 5-7mJ input power and 5 µm/s ablation speed.

3 Results

3.1 The Tomino ore field

The Tomino porphyry Cu deposit with 660 Mt @ 0.4% Cu (Russian Copper Company, 2019) consists of two diorite stocks, each ca. 2 km in diameter, dated as 427±6 Ma (U-Pb in zircons) (Grabezhev and Ronkin 2011), intruded into Ordovician basalts. The northern stock hosts the Tomino site, while the southern one – Kalinovskoe site. Molybdenite from the Kalinovskoe deposit was dated by Re-Os as 430.4 ± 2.0 Ma (Tessalina and Plotinskaya 2017; Plotinskaya et al. 2018).

EMPA study of molybdenite from the Kalinovskoe site revealed uneven distribution of Re within single grains of molybdenite with micron-scale zones where Re contents reach 0.95 wt.%. LA-ICPMS data show contents of Re as much as 8.7 to 4540 ppm, geom. mean 621 ppm), W (to 4.3 ppm, geom. mean 0.46 ppm), Se (32 to 350 ppm, geom. mean 146 ppm), Cu, Fe (tens to thousands ppm), Zn, Pb, Bi (several ppm to hundreds ppm), Co, Ni, As, Ag, Te, Au (up to tens ppm), Sb (up to several ppm) (Plotinskaya et al. 2018).

EMPA study of molybdenite from the Tomino site (1 sample) revealed Re-enriched growth zones (up to 0.68 wt.% of Re) within molybdenite flakes (Fig. 2). LA-ICP-MS data also show high contents of Re (2670 to 5800 ppm, geom. mean 3645 ppm), Se (194 to 410 ppm, geom. mean 271 ppm), low contents of W (1.5 to 5.8 ppm), as well as remarkable admixtures of Cu, Fe, Zn (tens to hundreds ppm), Ni, Te (tens ppm), As, Cd, Hg, Pb, (several ppm to tens ppm), Co, Ag, Sb, Au, Bi (up to several ppm).

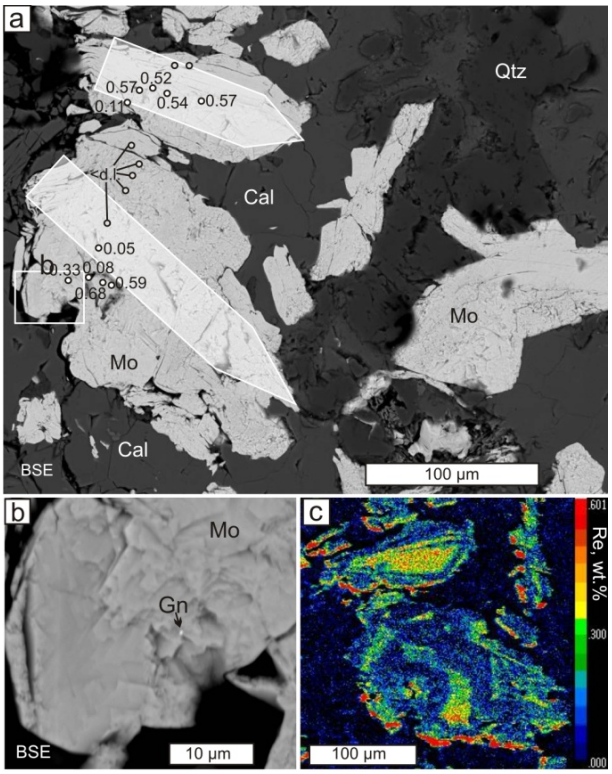

Figure 2. (a) BSE image of molybdenite (Mo) from the Tomino porphyry Cu deposit associating with quartz (Qtz) and calcite (Cal); numbers indicate Re contents in wt. %, d.l. – detection limit (0.04 wt.%); (b) detail of (a), inclusion of galena (Gn) in molybdenite; (c) calibrated X-ray map of the Re content in wt. %.

3.2 The Mikheevskoe deposit

The Mikheevskoe porphyry Cu deposit, with 629 Mt @ 0.41% Cu (Russian Copper Company, 2019), is the economically most significant porphyry Cu deposit in the Urals. Mineralization is hosted by Late Devonian sandstones, tuffstones, basaltic andesites, overlain by Late Devonian to Early Carboniferous basaltic lavas, tuffs, sandstones. Intrusions are represented by quartz diorite stocks and numerous diorite and granodiorite porphyry dykes (Shargorodsky et al. 2005) dated as 356±6 Ma (U-Pb in zircons) (Grabezhev and Ronkin 2011). Molybdenite from the Mikheevskoe deposit was dated by Re-Os as 357.8±1.8 Ma and 356.1±1.4 (Tessalina and Plotinskaya 2017).

Previous EMPA study (Plotinskaya et al. 2015) revealed micron-scale zones with up 1.34 wt.% of Re. LA-ICPMS study revealed contents of Re (83 to 3440 ppm, geom. mean 967 ppm), W (1.0 to 4.9 ppm), Se (124 to 848 ppm, geom. mean 307 ppm), Cu, Fe (tens to thousands ppm), Zn, Se (tens to hundreds ppm), as well as V, Co, Ni, As, Ag, Cd, Sb, Au, Hg, Pb, and Bi (several ppm to tens ppm).

3.3 The Benkala deposit

The Benkala porphyry Cu deposit (1.56 Mt Cu @ 0.42% Cu according to Frontier Mining (2012)) is associated with Early to Middle Carboniferous intrusions and dykes of the Sokolov-Sarbai diorite–granite complex (porphyritic quartz diorite and granodiorite, and plagiogranite porphyries) hosted by Lower Carboniferous volcano-sedimentary sequence (Gachkevich et al. 1986). Intrusions were dated as 334.7±2.9 Ma (U-Pb in zircons) (Grabezhev et al. 2017).

Molybdenite of the Benkala deposit (1 sample) contains Re (364 to 744 ppm, geom. mean 574 ppm), W (29.2 to 76.8 ppm, geom. mean 46.9 ppm), Se (72 to 120 ppm, geom. mean 96 ppm), Fe (thousands ppm), Cu (hundreds ppm), V, Zn, Pb (tens to hundreds ppm), As, (tens ppm), Co, Ag, Cd, (several ppm to tens ppm), Ni, Sb, Te, Au, Hg, Bi (up to several ppm).

3.4 The Talitsa deposit

The Talitsa Mo porphyry deposit is located in the western margin of the East Uralian megaterrane in the Middle Urals within a sub-alkaline intrusion of about 4 km^2 hosted by Devonian ultrabasic rocks and rhyolite-basalt volcanics. The Talitsa intrusion consists of granodiorite to quartz monzonites and minor monzodiorites cross-cut by granodiorite to quartz monzonite and granite porphyry stocks and dykes (Azovskova and Grabezhev 2008). The deposit was dated as 297.4±2.3 Ma (U-Pb in zircon) (Smirnov et al. 2017) and 298.3±1.3 Ma (Re-Os in molybdenite) (Tessalina and Plotinskaya 2017).

Molybdenite of the Talitsa deposit (5 samples, fig. 3) contains Re (40.8 to 388 ppm, geom. mean 109 ppm), W (6.0 to 232 ppm, geom. mean 17.4), Se (10 to 520 ppm, geom. mean 166 ppm), Fe, Cu, Zn, Sb, Pb, Bi (tens to thousands ppm), V, (tens to hundreds ppm), Ni, As, Cd, Ag,Te, Hg (up to hundreds ppm), Co (up to tens ppm), (several ppm to tens ppm), Au (up to several ppm).

4 Discussion

4.1 Trace elements incorporation in molybdenite

Most trace elements have positive correlations with each other (Fe, Co, Cu, Zn, Ni, As, Se, Ag, Cd, Sb, Te, Tl, Pb, and Bi) because they occur mainly as micro- to nano-scale mineral inclusions within molybdenite (Figs. 2, 3). Re and W usually have neither positive nor negative correlation with all other trace elements but show a weak negative correlation with each other (–0.26 for the whole dataset, –0.43 for the Mikheevskoe deposit). This means both Re and W substitute for Mo in the molybdenite structure. However in some LA-ICPMS profiles in molybdenite from the Talitsa deposit synchronous peaks of W^{182} and Ti^{47} indicate inclusions of rutile with W impurities (Fig. 3). Thus, the highest W contents observed in this study (over 60 ppm), are likely linked to mineral inclusions.

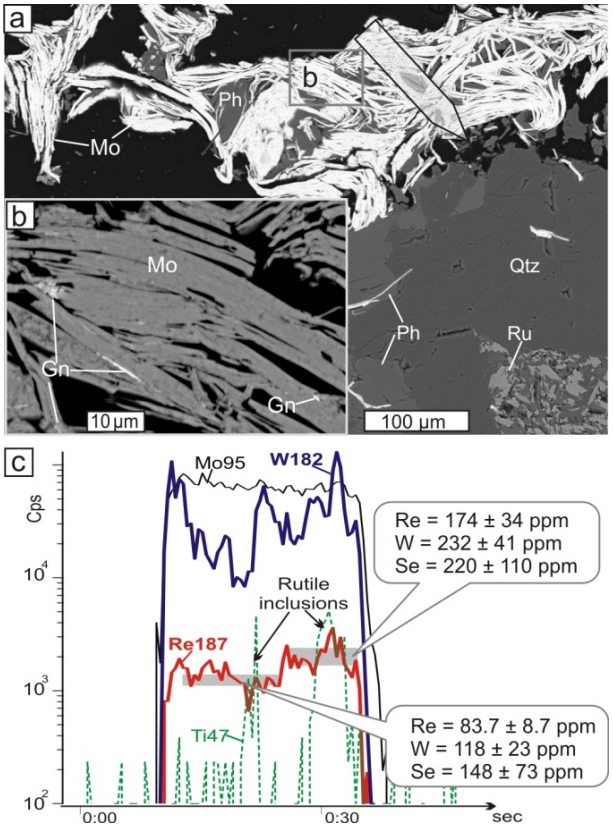

Figure 3. (a) BSE image of molybdenite (Mo) from the Talitsa porphyry Mo deposit associating with quartz (Qtz), phengite (Ph) and rutile (Ru); (b) detail of (a), inclusions of galena (Gn) in molybdenite; (c) time resolved LA-ICPMS line spectrum showing variations of selected isotopes; note synchronous peaks of W^{182} and Ti^{47} indicating inclusions of rutile.

4.2 Sources of rhenium and other metals

It is noteworthy that both Re and W are inhomogeneously distributed even within single grains of molybdenite (Figs. 2, 3) and vary in an order of magnitude within a deposit. Despite this, molybdenite from the deposits studied shows a significant difference in both Re and W contents. Molybdenite from Tomino and Mikheevskoe is featured by the highest contents of Re (mostly over 400 ppm) and lowest contents of W (<10 ppm), while molybdenite from the Talitsa deposit has lowest contents of Re (mainly below 200 ppm) and significant admixtures of W (6 to 50 ppm).

Mao et al. (2013) proposed that <10 ppm Re in molybdenite indicates crustal sources, 10 to 100 ppm indicates a mixed mantle/crustal source and >100 ppm Re in molybdenite indicates molybdenite derived from mantle sources. Therefore, the high Re contents of most molybdenites from Tomino, Mikheevskoe and Benkala deposits may indicate a predominantly mantle source for the metals, while molybdenite from the Talitsa deposit indicates a mixed mantle/crustal source (Fig. 4). Remarkable input of mantle material is in good agreement with a subduction setting of porphyry Cu deposits. Controls of W contents in molybdenite are not well understood. However continental crust is known to be enriched in W relative to mantle (Holland and Turekian

2003) and it can be supposed that significant input of crustal material may reflect elevated contents of W in molybdenite. It explains low contents of W in molybdenite from porphyry copper deposits from oceanic arc settings (e.g. in Tomino) and higher W admixtures in molybdenite from deposits formed on continental crust, i.e. Benkala deposit formed within a continental margin and Talitsa deposit formed due to continent-continent collision.

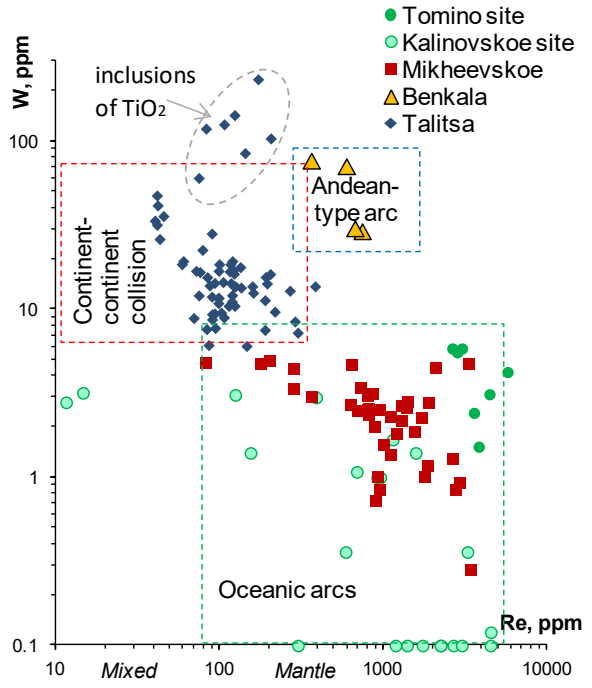

Figure 4. Re vs. W contents in molybdenite from the porphyry Cu(Mo) deposits studied. Fields for mixed mantle/crustal and mantle Re sources are from Mao et al. (2013) and references therein.

5 Conclusions

(1) Most trace elements form mineral inclusions within molybdenite in all deposits studied here; only Re and W are most likely to be incorporated into the molybdenite lattice.

(2) Porphyry Cu deposits formed within oceanic arc settings are featured by high contents of Re (mostly over 400 ppm) and low contents of W (<10 ppm) in molybdenite.

(3) Porphyry Cu deposits from Andean-type geotectonic environment (Benkala) are featured by lower Re content (hundreds ppm) and high contents of W (tens ppm) in molybdenite.

(4) Molybdenite from porphyry deposits from collisional setting (Talitsa) has low content of Re and elevated W contents (tens ppm).

(5) These results demonstrate that the study of trace element geochemistry molybdenite is a useful tool to define source of metal components in porphyry Cu(Mo) deposits.

Acknowledgements

This study was supported by RFBR ## 19-05-00254, 19-05-00476 and by NHM (CERCAMS program). RS acknowledges funding under NERC Grant NE/P017452/1 “From arc magmas to ores (FAMOS): A mineral systems approach”.

References

Azovskova OB, Grabezhev AI (2008) The Talitsa porphyry copper–molybdenum deposit, the first object of a subalkaline porphyry system in the Central Urals. Dokl Earth Sci 418(1):99–102.

Frontier Mining, 2012. http://www.frontiermining.com/operations/benkala.html (accessed 2012).

Grabezhev AI, Shardakova GY, Ronkin YL, Azovskova OB (2017) Systematization of U-Pb zircon ages of granitoids from the copper porphyry deposits on the Urals. Litosfera (Russia) 17(5):113–126.

Gachkevich IV, Kosterov EI, Zhukov NM, Filimonova LE (1986) The Benkala deposit. In: Abdulin AA, Chakabaev SE (Eds) Porphyry Copper Deposits of the Balkhash Region. Nauka, Alma Ata, pp. 73–79 (in Russian).

Grabezhev AI., Ronkin YL (2011) U-Pb age of zircons from ore-bearing granitoids of the South Urals porphyry-copper deposits. Lithosphere (Russia) 11(3):104–116 (in Russian with English abstract).

Holland HD, Turekian KK. Treatise on Geochemistry. Elsevier, 2003.

Mao Z, Cheng Y, Liu J, et al. (2013) Geology and molybdenite Re-Os age of the Dahutang granite-related veinlets-disseminated tungsten ore field in the Jiangxin province, China. Ore Geol Rev 53:422–433.

Petrov O, Shatov V, Kondian O, et al. (2007) Mineral Deposits of the Urals, 1M Scale Map and Database, Short Description (Explanatory Notes) CERCAMS, NHM, London.

Plotinskaya OY, Grabezhev AI, Seltmann R (2015) Rhenium in ores of the Mikheevskoe porphyry Cu-Mo deposit, South Urals. Geol Ore Depos 57(2):118–132.

Plotinskaya OY, Abramova VD, Groznova EO, et al. (2018) Trace element geochemistry of molybdenite from porphyry Cu deposits of the Birgilda-Tomino ore cluster (South Urals, Russia). Mineral Mag. 82(S1):S281–S306.

Plotinskaya OY, Grabezhev AI, Tessalina S, et al. (2017) Porphyry deposits of the Urals: geological framework and metallogeny. Ore Geol Rev 85:153–173.

Russian Copper Company. http://rmk-group.ru/en/activities/enterprises/ (accessed 11/03/2019).

Shargorodskii BM, Novikov IM, Aksenov SA (2005) The Mikheevskoe copper porphyry deposit in the South Urals. Otechestvennaya Geologia (2):57–61 (in Russian).

Smirnov VN, Ivanov KS, Shokalsky SP, Ronkin YL (2017) The results of U-Pb SHRIMP-II dating of zircon from granitoids of Talitsky molybdenum-bearing massif (eastern slope of the Middle Urals). Lithosphere (Russia) 17(3):145–150. (in Russian with English abstract).

Tessalina SG, Plotinskaya OY (2017) Silurian to Carboniferous Re-Os molybdenite ages of the Kalinovskoe, Mikheevskoe And Talitsa Cu- and Mo porphyry deposits in the Urals: implications for geodynamic setting. Ore Geol Rev 85:174–80.

Tevelev AV, Kosheleva IA, Popov VS, et al. (2006) Paleozoides of the Juncture Zone between the Eastern Urals and Transural Region. MSU Publisher, Moscow (in Russian).